

Investigating Mineral Weathering and Metal Transport through Century-Old Ore Chimney Waste Rock

Author: Andrew Hicks

A thesis addressed to the Department of Earth Sciences
and submitted to the Faculty of Graduate and Postdoctoral Affairs
in partial fulfilment of the requirements for the degree of

Master of Science

In

Earth Sciences

Carleton University, Ottawa, ON, Canada

(Ottawa-Carleton Geoscience Centre)

Copyright © Andrew Hicks, 2021. All Rights Reserved.

Author's Declaration and Dedication

I hereby declare that I am the sole author of this thesis. To the best of my knowledge, this thesis contains no materials previously published or written by another person and any contribution made by others is explicitly acknowledged. This is a true copy of the thesis, including any required final revisions, as accepted by my examiners.

I understand that this thesis may be made electronically available to the public.

As a testimony of gratitude, this thesis is dedicated to the companionship and memory of Clark Bolliger. Clark always pointed his compass in the right direction and establishing a friendship over the years was a privilege. Even when times were tough, Clark's optimism and wonderful sense of humour always shined through. Thank you for the positive influence you had on my life and may you forever live on through my acquired character and cherished memories.

Abstract

Sulfide minerals have an affinity to react with oxygen in the atmosphere when exposed above ground surface with the potential to release metals and acidity into the surrounding environment. The extent of contaminant release can be a function of time, and the myriad of historically abandoned mines across Canada create concern for how mine-waste systems, especially waste-rock piles, are affected by long-term exposure at Earth's surface. This thesis investigates the long-term weathering of a historical waste-rock pile at the Ore Chimney mine, which was developed ~100 years ago. Three trenches that transect the entire depth were excavated and 5 to 6 kg of waste-rock material were sampled at 0.5 m depth intervals. Waste-rock material was sieved into fine (< 0.5 mm) and coarse (0.5 to 2.0 mm) grain size fractions and in situ solid-phase geochemical signatures were investigated with optical microscopy, scanning electron microscopy with energy dispersive spectrometry, powdered X-ray diffraction, total carbon and sulfur analysis, and solid-phase digestions followed by inductively coupled plasma atomic emission and mass spectrometry (ICP-AES/MS). Samples were centrifuged to extract porewaters and analyzed by spectrophotometry, anion chromatography, and ICP-AES/MS. The geochemical modelling software PHREEQC was used to explore possible secondary controls on porewater chemistry.

Solid-phase geochemical investigations revealed average total carbon and sulfur concentrations of 1.38 wt.% [C] (comprised of calcite and dolomite) and 2.02 wt.% [S], respectively, and Zn and Pb concentrations of 1.56 and 1.38 wt.%, respectively. Sulfur content was associated with a sulfide mineral assemblage primarily composed of sphalerite and galena, with less frequent occurrence of pyrite and chalcopyrite sourced from carbonate-bearing quartz veins. Porewater pH was near-neutral suggesting ongoing acid neutralization and elevated Eh ($\mu = +421$ mV) indicate that oxygen was the main oxidizing agent independent of depth. Porewater ICP-AES measured Zn as high as 87.5 ppm accounting for 92% [M] of average heavy metal concentrations and is attributed to the oxidative

dissolution of sphalerite. High alkalinity levels ($\mu = 60.2 \text{ mg/L CaCO}_3$) suggest that calcite and dolomite are likely controlling pH, [Pb], [Zn], [Cd], and [Cu] in the porewaters. Results from this study indicate that the source lithology of sulfides plays a strong role in weathering. After ~100 years, sphalerite and galena grains are strongly altered but pyrite and chalcopyrite remain relatively unweathered suggesting that chemical weathering processes may continue for some time, but abundant Ca-carbonates will provide long-term buffering. This study shows that a detailed understanding of in situ solid- and aqueous-phase geochemistry is required to delineate waste-rock weathering as a function of long-term exposure.

Acknowledgements

This project was made possible by the Ontario Research Fund – Research Excellence Grant “Integrated tools and technologies for environmentally-responsible management of metal-bearing wastes” awarded to Dr. David Blowes and Dr. Carol Ptacek (Principal Investigators from the University of Waterloo) by the Ontario Ministry of Research, Innovation, and Science. First and foremost, I wish to extend my sincerest gratitude to my supervisor, Dr. Richard Amos, for recognizing my potential and continually showing support since my freshman year as an undergraduate student. Thank you for providing me with unparalleled opportunities throughout my experience at Carleton University including this project. The results from this study were arguably ~100 years in the making and completing this project may have taken just as long if not for your advisement, enthusiasm, and encouragement. I would also like to thank Timothy Mount for the tireless effort in completing the polished grain mounts and to Dr. Maryam Shahabi Far for your incredible work on the scanning electron microscope and for prioritizing my research to ensure I graduated on time. All your insights and recommendations were invaluable and provided me with the open mind necessary to develop a proper understanding in this field. A great deal of credit is owed to advisory board members Dr. Tom Al from the University of Ottawa and Dr. James Mungall from Carleton University for their expertise, knowledgeable recommendations, and for working within the parameters of a stressed timeline.

I wish to acknowledge Jeff Bain and Danielle Marie Simons from the University of Waterloo for undertaking the responsibility to analyze and post-process the total carbon and sulfur data. Field and laboratory work was mostly conducted independently; thus, I am very grateful for your contributions, which facilitated the research progress significantly. Furthermore, I would like to thank Dr. Jeffery Ovens and Dr. Lilianne Pagé from the University of Ottawa for treating me with overwhelming respect and for their exceptional work with powdered X-ray diffraction (PXRD) ensuring that proper analytical techniques were employed, and appropriate adjustments were made to collect data at the highest resolution. The

freeze-drying was permitted thanks to accommodations by Dr. Myron Smith and the post-processing of PXRD data was made possible by Dr. George Dix at Carleton University. Special thanks are owed to Dr. Nimal De Silva from the University of Ottawa for your incredible work on solid- and aqueous-phase atomic emission and mass spectrometry in addition to anion chromatography. I commend your knowledge, patience, and attention to detail, which are paramount qualities for gathering such a valuable dataset and I am incredibly fortunate to have been able to confine most of my analyses within the Ottawa-Carleton Geoscience Centre, which otherwise would not have been possible without your extraordinary help.

I am deeply indebted to Ken Cuddy for navigating through rough terrain with his excavator and for single-handedly deconstructing the waste-rock pile in sub-zero temperatures. There would be no project without a successful field season, which could only be attempted once, and your work ethic, skill, and composure deserves the utmost respect. Likewise, the field work would have not been possible without the help of Thomas Hicks who is a phenomenal field assistant and an even better brother. From clearing toppled spruce trees, to hauling hundreds of kilograms of waste-rock material off site by hand using a toboggan, and for always having my back; I owe you some serious favours and cannot thank you enough. I also wish to recognize Gary Smith and John Archibald for granting permission to conduct research at the privatized Ore Chimney property. I would like to thank Carleton University and the Department of Earth Sciences for their acceptance and accommodation throughout my graduate studies. Above all, I wish to formally congratulate my parents, Pauline and Steve, for recently celebrating their 30th anniversary and forever exemplifying the importance of family. Your unrivaled love and support have always provided me with the incentive to embrace life's toughest challenges and this project was certainly no exception. For all the hardships endured and sacrifices made, I thank you from the bottom of my heart.

Table of Contents

Chapter 1: Introduction	1
1.1 Mining and the Environment.....	1
1.2 Ore Chimney	6
1.3 Thesis Structure and Objectives of Research	9
Chapter 2: Mineralogy and Solid-Phase Geochemistry	12
2.1 Introduction	12
2.2 Methods	14
2.2.1 Field Methods	14
2.2.2 Sample preparation.....	15
2.2.3 Analytical Methods	16
2.3 Results	20
2.3.1 X-ray Diffraction: Phase Identification and Quantitation.....	21
2.3.2 Ore Petrography	26
2.3.3 Total Inorganic Carbon and Sulfur (C/S) Analysis.....	34
2.3.4 Solid Phase Chemistry.....	38
2.4 Discussion.....	45
2.4.1 General Lithology and Mineralogy	45
2.4.2 Mineral-Derived Metals in the Waste Rock	50
2.4.3 Sulfide Mineral Weathering	55
2.4.4 Total Carbon and Sulfur.....	59
2.4.5 Implications	64
Chapter 3: Porewater Chemistry	66
3.1 Introduction	66
3.2 Methods	68
3.2.1 Sample Preparation	68
3.2.2 Analytical Methods	70
3.3 Results	70
3.3.1 Porewater Chemistry.....	71
3.3.2 Mineral Saturation Indices.....	84
3.4 Discussion.....	91
3.4.1 Porewater Chemistry and Secondary Controls	91

3.4.2 Implications	106
Chapter 4: Conclusions	110
4.1 General Summary of Implications	110
4.2 Recommendations for Areas of Future Research	111
5.0 References	113

List of Tables

Table 2.1: Sulfide mineral oxidation ranking	17
Table 2.2: Sulfide alteration index (SAI) of the Ore Chimney waste-rock pile	17

List of Figures

Figure 1.1: Historical imagery (1934) of Ore Chimney (Natural Resources Canada, 2016).....	10
Figure 2.1: a) Aerial schematic of the waste-rock pile with location of vertical transects (stars; T = trench), b) Cross-sectional view of sampling locations (8× vertically exaggerated).	15
Figure 2.2: Major mineral phase depth plots for trench 1 (left), trench 2 (middle), and trench 3 (right).	24
Figure 2.3: Minor mineral phase depth plots for trench 1 (left), trench 2 (middle), and trench 3 (right).	25
Figure 2.4: Average pyrite, chalcopyrite, sphalerite, and galena oxidation ranking for each waste-rock sample location for trench 1 (left), trench 2 (middle), and trench 3 (right).	27
Figure 2.5: Common ore minerals under reflected light (0.5 to 2.0 mm grain size) (i.e. C1 refers to coarse grain fraction at trench 1).	30
Figure 2.6: Common ore minerals under reflected light (< 0.5 mm grain size) (i.e. F3 refers to fine grain fraction at trench 3).....	31
Figure 2.7: Trace ore minerals under reflected light (F: < 0.5 mm, C: 0.5 to 2.0 mm grain size).	32
Figure 2.8: BSE images of pyrite (a and b) and chalcopyrite (c and d) weathering phases under SEM (< 0.5 mm grain size).	32
Figure 2.9: BSE images of sphalerite (a and b) and galena (c and d) weathering phases under SEM (< 0.5 mm grain size).	33
Figure 2.10: BSE images of pyrite and Ca-carbonate phases under SEM (< 0.5 mm grain size).	34
Figure 2.11: Total C and S content (wt.%) for coarse (left) and fine (right) grain fractions for a) trench 1, b) trench 2, c) trench 3. Error bars show the standard deviation from three consecutive measurements	35
Figure 2.12: Acid generation potential for a) trench 1, b) trench 2, c) trench 3. .	37

Figure 2.13: Solid-phase iron (Fe), copper (Cu), zinc (Zn), and lead (Pb) depth plots for trench 1 (left), trench 2 (middle), and trench 3 (right).....	42
Figure 2.14: Solid-phase manganese (Mn), cadmium (Cd), arsenic (As), and antimony (Sb) depth plots for trench 1 (left), trench 2 (middle), and trench 3 (right).....	43
Figure 2.15: Solid-phase titanium (Ti), chromium (Cr), cobalt (Co), and nickel (Ni) depth plots for trench 1 (left), trench 2 (middle), and trench 3 (right).	44
Figure 2.16: Historical sketch of the Ore Chimney waste-rock pile updated with study sampling locations (modified from Kingston, 1980).....	46
Figure 2.17: BSE images of Fe- and Ti-oxide phases in the Ore Chimney waste rock.....	54
Figure 2.18: BSE images (a and b) and reflected light images (c - f) of sulfide minerals bound with quartz (Q).....	61
Figure 3.1: a) Falcon™ tubes shortened to 45 mL and filled with loose waste-rock material (2 mm hole drilled at the base and lined with glass wool), b) Falcon™ tubes shortened to 10 mL and placed underneath for porewater collection.	69
Figure 3.2: Aqueous-phase pH, Eh, alkalinity, and sulfate (SO ₄ ²⁻) depth plots for trench 1 (left), trench 2 (middle), and trench 3 (right).	73
Figure 3.3: Aqueous-phase sodium (Na), potassium (K), calcium (Ca), and magnesium (Mg) depth plots for trench 1 (left), trench 2 (middle), and trench 3 (right).	75
Figure 3.4: Aqueous-phase iron (Fe), copper (Cu), zinc (Zn), and lead (Pb) depth plots for trench 1 (left), trench 2 (middle), and trench 3 (right).....	77
Figure 3.5: Aqueous-phase manganese (Mn), cadmium (Cd), arsenic (As), and antimony (Sb) depth plots for trench 1 (left), trench 2 (middle), and trench 3 (right).....	79
Figure 3.6: Aqueous-phase titanium (Ti), chromium (Cr), cobalt (Co), and nickel (Ni) depth plots for trench 1 (left), trench 2 (middle), and trench 3 (right).	81
Figure 3.7: Aqueous-phase aluminum (Al), chloride (Cl ⁻), and phosphate (PO ₄ ³⁻) depth plots for trench 1 (left), trench 2 (middle), and trench 3 (right).....	83

Figure 3.8: Calcite, dolomite, gypsum, and jarosite depth plot saturation indices for trench 1 (left), trench 2 (middle), and trench 3 (right). Dashed lines indicate SI boundary between -0.5 and +0.5.....	85
Figure 3.9: Gibbsite, boehmite, ferrihydrite, and Cr(OH)_3 (am) depth plot saturation indices for trench 1 (left), trench 2 (middle), and trench 3 (right).	88
Figure 3.10: Manganite, $\text{Mn(HPO}_4\text{)}$, malachite, and otavite depth plot saturation indices for trench 1 (left), trench 2 (middle), and trench 3 (right).	89
Figure 3.11: Cerussite, Pb(OH)_2 , smithsonite monohydrate, and Zn(OH)_2 depth plot saturation indices for trench 1 (left), trench 2 (middle), and trench 3 (right).	90
Figure 3.12: Ca correlation plot with Mg for trench 1 (left), trench 2 (middle), and trench 3 (right).	94
Figure 3.13: Zn correlation plots with SO_4^{2-} , Ca (mmol/L), pH, and Cd ($\mu\text{mol/L}$) for trench 1 (left), trench 2 (middle), and trench 3 (right).	100
Figure 3.14: Zn (mmol/L) correlation plots with Pb, Cu, Co, and Ni ($\mu\text{mol/L}$) for trench 1 (left), trench 2 (middle), trench 3 (right).	102
Figure 3.15: Ca (mmol/L) correlation plot with Mn ($\mu\text{mol/L}$) for trench 1 (left), trench 2 (middle), and trench 3 (right).	104

Chapter 1: Introduction

1.1 Mining and the Environment

Canada's mining sector is an important part of the Canadian economy. As of the 2017 fiscal year, approximately 634,000 employment positions were created directly in or partially involved with mining (16,500 of which for indigenous people). Likewise, mining in Canada contributed \$97 billion CAD, which accounts for approximately 5% of Canada's total GDP (Marshall, 2017). Key resources that contribute to Canada's mining wealth include gold (\$8.8 billion), coal (\$6.3 billion), iron ore (\$4.7 billion), and diamond (\$2.7 billion CAD) (Natural Resources Canada, 2017), and the richness of natural resources in Canada appeals highly to prospecting and investing in the mining industry (Stedman and Green, 2019).

The treatment processes of ore material typically involve the use of different chemicals (Muhammed and Zhang, 1989). Gold, for example, is separated and purified with the help of harmful compounds such as cyanide and hydrogen peroxide (La Brooy et al., 1994). The waste material remaining from the purification process of ore bodies retains harmful chemicals and is typically unloaded nearby, as tailings. In addition, gold ore is often rich in other metals, in the form of silicate, sulfide, and oxide minerals, that are too expensive to purify and remain in the tailings after the gold is separated (Blowes et al., 2013). These minerals are more concentrated near ore bodies, but often persist throughout the subsurface within the surrounding area (Carranza and Sadeghi, 2012).

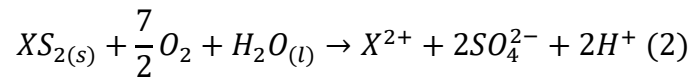
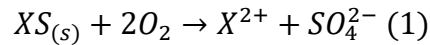
Waste rock is material that is removed to access the ore body and is different from tailings as it is left unprocessed. Although waste rock is not treated with harmful chemicals, the material itself contains metals in the form of sulfide minerals, which may reduce the quality of drainage waters under certain conditions. Waste rock tends to be lower in total sulfur (wt.% S) content than the tailings material that is processed from the ore body (Sracek et al., 2004). However, active mining operations often impose steady removal and stockpiling of large volumes of waste-

rock material that can be expensive to monitor (Amos et al., 2015). The rising demand for natural resources and the subsequent increasing scale in the Canadian mining industry comes with a growing importance of understanding the impact mining can have on the environment and how to properly manage mine-waste material (Hudson-Edwards et al., 2011).

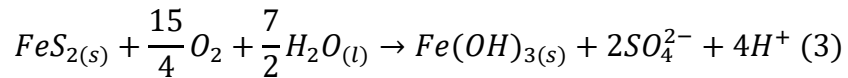
Mining regulations in Ontario were introduced in 1845 and mainly addressed exploration and land ownership rights and government tax requirements (MNDM, 2008). A discovery of a large silver deposit in Cobalt, Ontario, in 1903, prompted an extensive review of the Mining Act in 1906 designating a Mining and Lands Commissioner to regulate land claim practices, enforce labour health and safety measures, and mediate corporate legislative conflict (Kammerman, 2006). For example, prospectors in the early 1900's could not file for a mining patent until an ore discovery was made, which resulted in a plethora of exposed rocks at the surface from exploration. Likewise, labour disputes, engineering failures, and economic downfalls often created financial difficulties, which left a significant disregard for environmental considerations (Mackasey, 2000). It was not until the early 1990's that the Mining Act was updated to stipulate environmental reclamation upon site closure (Kammerman, 2006). As a result, the remains of historical mining activities are left scattered across Ontario among many other Canadian provinces leaving a legacy of contamination detrimental to surrounding ecosystems. Notorious examples include the Giant mine, NWT (O'Reilly, 2012), and Britannia mine, BC (Smitheringale, 2011); however, there are hundreds of smaller and lesser-known examples such as the Ore Chimney mine (the subject of this thesis) that may also pose environmental threats.

Waste-rock material piled at Earth's surface is exposed to significantly different conditions compared to its previous entrapment underground; namely, larger temperature variation and elevated oxygen concentrations. Seasonal fluctuations in temperature and precipitation accelerate chemical reactions between minerals in the waste-rock and oxidizing agents above ground surface (i.e. chemical weathering) (Akcil and Koldas, 2006). Moreover, weaker fragmented material from

blasting coupled with the freeze-thaw dynamics of water in high-latitude climates exacerbate the effects of chemical weathering by opening conduits in surfaced material and increasing mineral reactivity with the atmosphere (Sinclair, 2014). Sulfide minerals can be classified into monosulfides such as sphalerite (ZnS) and galena (PbS), and disulfides such as pyrite (FeS₂) and chalcopyrite (CuFeS₂). Monosulfide (1) and disulfide (2) weathering reactions under the presence of oxygen (Plumlee, 1999) can be generalized as:

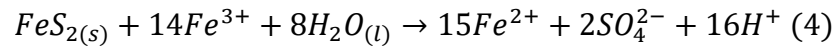


Where X^{2+} represents a divalent transition metal with common examples including ferrous iron (Fe^{2+}), copper (Cu^{2+}), zinc (Zn^{2+}), and lead (Pb^{2+}). The main difference between equations 1 and 2 is that monosulfide oxidation under the presence of oxygen is a non-acid generating process. In general, metal-sulfide mineral oxidation reactions are often the main chemical weathering processes in mine wastes with the potential to release metals and acidity into the environment (Amos et al., 2015). Ferrous iron is of particular interest because it can further oxidize into ferric iron under the thermodynamic conditions at Earth's surface and precipitate as ferric hydroxide minerals. Consequently, the overall net reaction for pyrite oxidation generates two moles of acidity for every mole of sulfur (Blowes et al., 2013) (3):

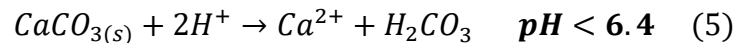


In the above reactions, elevated sulfate (SO_4^{2-}), dissolved metals (X^{2+}), and acidity may be expected; this poor-quality leachate water is referred to as acid mine drainage (AMD). When present, oxygen is the main agent for the oxidative dissolution of sulfide minerals. However, sulfide minerals, for example pyrite, can also oxidize under the presence of ferric iron (elevated in systems with $pH \leq 3$ due

to the increased solubility of ferric oxyhydroxides such as $Fe(OH)_3$, which can contribute to the overall generation of acidity (Amos et al., 2015) (4):



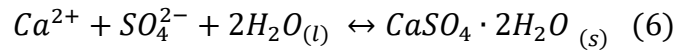
Depending on other minerals present in the waste-rock material, elevated acidity (i.e., equations 2, 3, and 4) can promote secondary mineral dissolution reactions that often control the geochemical weathering signatures observed in these aerobic systems. Calcium-bearing carbonate minerals most effectively buffer effluent to near-neutral levels if they are sufficiently present in the system. Calcite ($CaCO_{3(s)}$) and dolomite ($CaMg(CO_3)_2(s)$) buffer acid-generating waste to an observed pH range of 6.2 to 8.3 (Parbhakar-Fox and Lottermoser, 2017). Moreover, calcite reacts faster than dolomite by one order of magnitude (Lapakko, 2002) and one mole of Ca-carbonate (represented by calcite) can buffer up to two moles of acidity (5):



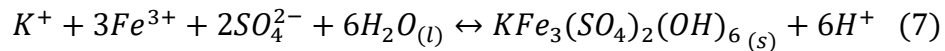
In the absence of Ca-carbonates, or when these minerals have depleted from the system, continuous oxidation of sulfide minerals may further elevate the acidity and a different buffering mineral will control the pH. One example of this is the Nickel Rim mine in Sudbury, Ontario, where the depletion of Ca-carbonate minerals in the upper portion of a tailings impoundment presented non-uniform pH measurements across depth (Johnson et al, 2000). If Ca-carbonates are depleted, the generalized mineral buffering sequence, in order of decreasing pH, includes siderite ($Fe^{2+}CO_{3(s)}$) (buffers at pH ~5), aluminum hydroxide ($Al(OH)_3(s)$) (pH ~4 to 4.5), iron(III) (oxy)hydroxide (pH ~2.5 to 3.5), and aluminosilicate minerals (i.e. $NaAlSi_3O_8$) (significant at pH < 2.5) (Bain et al., 2001; Blowes et al., 2013; Amos et al., 2015).

Elevated concentrations of sulfate (equations 1 to 4) and dissolved calcium (equation 5) in the waste-rock porewaters, when approaching saturation in solution, can facilitate the precipitation of certain salts, such as gypsum (Blowes et

al., 2013). This precipitation reaction proceeds independently of pH and limits the concentration of dissolved Ca^{2+} and SO_4^{2-} in solution (6).



Ferric iron (Fe^{3+}) is typically enriched over Fe^{2+} in aerobic systems as the final oxidation product of pyrite. Similarly, elevated ferric iron and sulfate (equation 3) and potassium (from the weathering of mica minerals) can precipitate jarosite and limit the dissolved concentration of ferric iron in porewaters (Leahy et al., 2009; Blowes et al., 2013) (7):



Consequent poor quality runoff waters released into the local watershed necessitates efforts to inhibit AMD processes and manage the waste material produced from mining. Traditionally, contaminated groundwater is pumped and treated at the surface (Rivett et al., 2006). However, actively treating contaminated mine waters, especially at decommissioned sites in secluded locations, is an expensive and painstaking process (Ford, 2003; Ziemkiewicz et al., 2003). Alternatively, passive treatment systems can be installed to react with drainage waters in-place and mitigate the financial burden from continuous pump-and-treat methods (Akcil and Koldas, 2006). Waste rock and tailings material deficient in Ca-carbonate minerals may require an artificial Ca-carbonate supply (Hedin et al., 1994). Moreover, elevated metals and sulfate can be remediated by sulfur reducing bacteria that proliferate in anoxic wetland environments (Jameson et al., 2010).

Passively treating contaminated throughflow waters is a low-maintenance cost-effective alternative for managing poor-quality mine drainage (Blowes et al., 2013). However, some chemically driven passive treatment systems still require maintenance and only remain functional along a 20- to 30-year timeline (Watzlaf et al., 2004). Alternatively, biologically driven wetland systems may have greater benefits as a long-term passive remediation option for treating mine drainage with

a circumneutral pH (Hsu and Maynard, 1999). Advantages to natural wetlands include the high attenuation capacity and storage of metals as well as ecological benefits, especially when preceded by Ca-carbonate pH buffering (Sheoran and Sheoran, 2006; Mayes et al., 2009; Blowes et al., 2013). Recognizing the long-term weathering processes of mine waste may help understand the utility of wetland systems to naturally attenuate low-quality drainage water in contaminated sites (Machemer and Wildeman, 1992; Skousen et al., 2000).

1.2 Ore Chimney

Ore Chimney is a historical gold prospecting site located near the town of Harlowe, Ontario, approximately 150 km west of Ottawa (44° 46'35" N, 77° 9'10" W). The 500-acre (2 km²) property lies within the southwest region of Frontenac County (Archibald, 2012). An abandoned ~10 kiloton (kt) waste-rock pile remains from nearby underground exploration adjacent to an organic-rich fen (Kingston and Papertzian, 1982). Previous site research assessing local groundwater and surface water flow indicates drainage from the pile, downgradient into the wetland area with localized flow to the southeast. Preliminary chemical analyses of throughflow waters near the waste-rock pile indicate near-neutral pH with some elevated metals, particularly zinc, calcium, and magnesium (Harper et al., 2021). Seasonal water table fluctuations typically present wetland surface waters during the spring months and on-site vegetation mainly consists of spruce, poplar, and birch trees.

Ore Chimney experiences a warm-summer humid continental climate with significant seasonal variation in daylight and temperature. Records since 1981 indicate that the coldest temperatures arrive during January with an average monthly temperature of -11.5°C and an elevated average temperature of 20.7°C during the month of July (Environment Canada, 2010). The hot summers frequently experienced around the Ottawa Valley raise humidity levels that increase the likelihood of severe storm events with strong winds and torrential downpours. The Ore Chimney property receives approximately 81 cm of

precipitation per year as a combination of rain and snow (Environment Canada, 2010).

Gold findings at Ore Chimney were first made in 1902, which prompted the excavation of a 123.4 m vertical mineshaft and branching underground corridors from 1909 to 1917 (Harnois and Moore, 1989). Mining rights were first held by the Ore Chimney Mining Company Ltd., which funded development on the property including the construction of an ore-processing stamp mill in 1915. Subsurface development continued intermittently from 1923 to 1932, which focused on extending and reinforcing the lateral underground network. Proprietorship at Ore Chimney changed when the site was purchased by Bey Mines Ltd. in 1928. The property continued to experience changes in ownership and was subjected to various drilling, mapping, and geophysical surveys before the mineshaft was officially capped and decommissioned in 1991 (Archibald, 2012). Despite significant efforts in prospecting and underground development, no ore material was ever processed from the Ore Chimney mine; thus, is considered and referred to as a mine only in name (Moore and Morton, 1986).

The Ore Chimney property is situated within the Mazinaw Domain, which is a stretch of land approximately 25 km wide that extends from Madoc, Ontario, 100 km northeastwards into Quebec (McCarron, 2013). The Mazinaw Domain is distinguished from other geological terranes due to its abundance and variation of metavolcanic rocks, and structural evidence within the metamorphic lithology suggesting two deformational events (MNDM, 1994). The Mazinaw Domain is one of few geological domains and terranes that comprise the Central Metasedimentary Belt (CMB). The CMB is part of the Grenville Province that covers a significant portion of southeastern Ontario and is located near the southern boundary of the Canadian Shield (Easton, 2006).

The oldest lithological unit at Ore Chimney is the Tudor Formation, which is crystalline volcanic basement rock that formed no earlier than 1.5 billion years ago (Ga) (Moore and Thompson, 1980). The metavolcanics comprising the Tudor Formation mainly consist of tholeiitic basalt with the intermittent presence of

amphibolite characterized by the foliation of hornblende with additional plagioclase feldspar and quartz. Minor and trace minerals attributed to the Tudor Formation include epidote, biotite, garnet, chlorite, pyrite, magnetite, tourmaline, and calcite (Harnois and Moore, 1988).

Overlying the Tudor Formation is the Ore Chimney Formation, which is a thin (< 10 m) biotite schist unit extending across the local area but is most easily distinguished at the Ore Chimney property. Mixed into the matrix of the Ore Chimney Formation is the presence of muscovite with porphyroblasts of garnet and hornblende. Other minerals identified in minor amounts include magnetite, hematite, pyrite, chalcopyrite, apatite, tourmaline, chlorite, and titanite (Harnois and Moore, 1988). Genesis of the Ore Chimney Formation is proposed as a result from hydrothermal alteration, reconsolidation, and metamorphism of material eroded from the Tudor Formation. This unconformity and subsequent metamorphic activity led to the creation of the Ore Chimney Formation approximately 1.2 Ga (Moore and Thompson, 1980).

The Flinton group overlies the Ore Chimney Formation and represents the youngest rocks in the area. The three main formations belonging to the Flinton group are the Myer Cave Formation, the Lessard Formation, and the Bishop Corners Formation. Surficial geology at the Ore Chimney property most commonly displays the Bishop Corners Formation, characterized by the presence of muscovite schist, quartzite, and oligomictic metaconglomerate. The minerals comprising the lithology of the Bishop Corners Formation include muscovite, quartz, plagioclase feldspar, orthoclase feldspar, and magnetite. The Flinton group was deposited in a fluvial environment resulting from continental uplift nearly 1.1 Ga. The continental uplift was part of the Grenvillian Orogeny, which regionally deformed all the rocks in the area approximately 1 Ga and is the most recent metamorphic activity on site (Moore and Thompson, 1980).

Major tectonic stresses exerted on the region over the course of the Grenvillian Orogeny opened fractures in the subsurface carrying fluids with solubilized mineral components from a nearby dyke intrusion that crystallized as a series of quartz

veins hosting calcite and dolomite at average volume proportions of 5% that occasionally measured as high as 20% (Harnois and Moore, 1989). Property surveys reveal a network of 14 quartz veins on the Ore Chimney property, five of which display significant sphalerite, galena, pyrite, and chalcopyrite mineralization (Archibald, 2012). Extensive drilling through one of the quartz veins yielded gold estimates of 7 g/tonne (Au), silver estimates as high as 193 g/tonne (Ag) and assays of lead and zinc at 3.2 and 1.9 wt.%, respectively (Carter 1984; Archibald, 2012). The quartz veins were the prospected ore deposit and formed 30 m below an unconformable contact between the Tudor Formation and the Bishop Corners Formation (Harnois and Moore, 1989).

1.3 Thesis Structure and Objectives of Research

Remaining at the Ore Chimney mine are the ruins of old structures, the abandoned mine shaft, and an estimated ~10 kt waste-rock pile that lies above the water table, approximately 30 m north of the mineshaft. Although prospecting activities continued at Ore Chimney until 1999, the ~10 kt waste-rock pile is documented to be formed from material removed to create the mineshaft and underground network from 1909 to 1932 (Archibald, 2012; Sangster et al., 2012). Aerial photography of the historical Ore Chimney mine in 1934 (Figure 1.1) combined with visual on-site inspections show little disturbance of the pile throughout time, corroborating estimations of ~100 years of subaerial exposure. Therefore, it is presumed that the waste-rock pile resembles material that was excavated as the underground network periodically expanded over an elapsed timeline of approximately 25 years. It is estimated that some of the earliest material was dumped ~110 years ago, and the most recent stockpiling of waste-rock material took place no later than ~85 years ago. The relationship between waste-rock pile strata and exposure time across the ~25-year underground tunneling phase is relatively uncertain aside from assuming that the development of the waste-rock pile follows Nicolaus Steno's principle of superposition (Winter, 1916). However, it is certain that the waste-rock pile at the Ore Chimney site, in its entirety, has been subjected to weathering above ground surface for a minimum of 85 years.

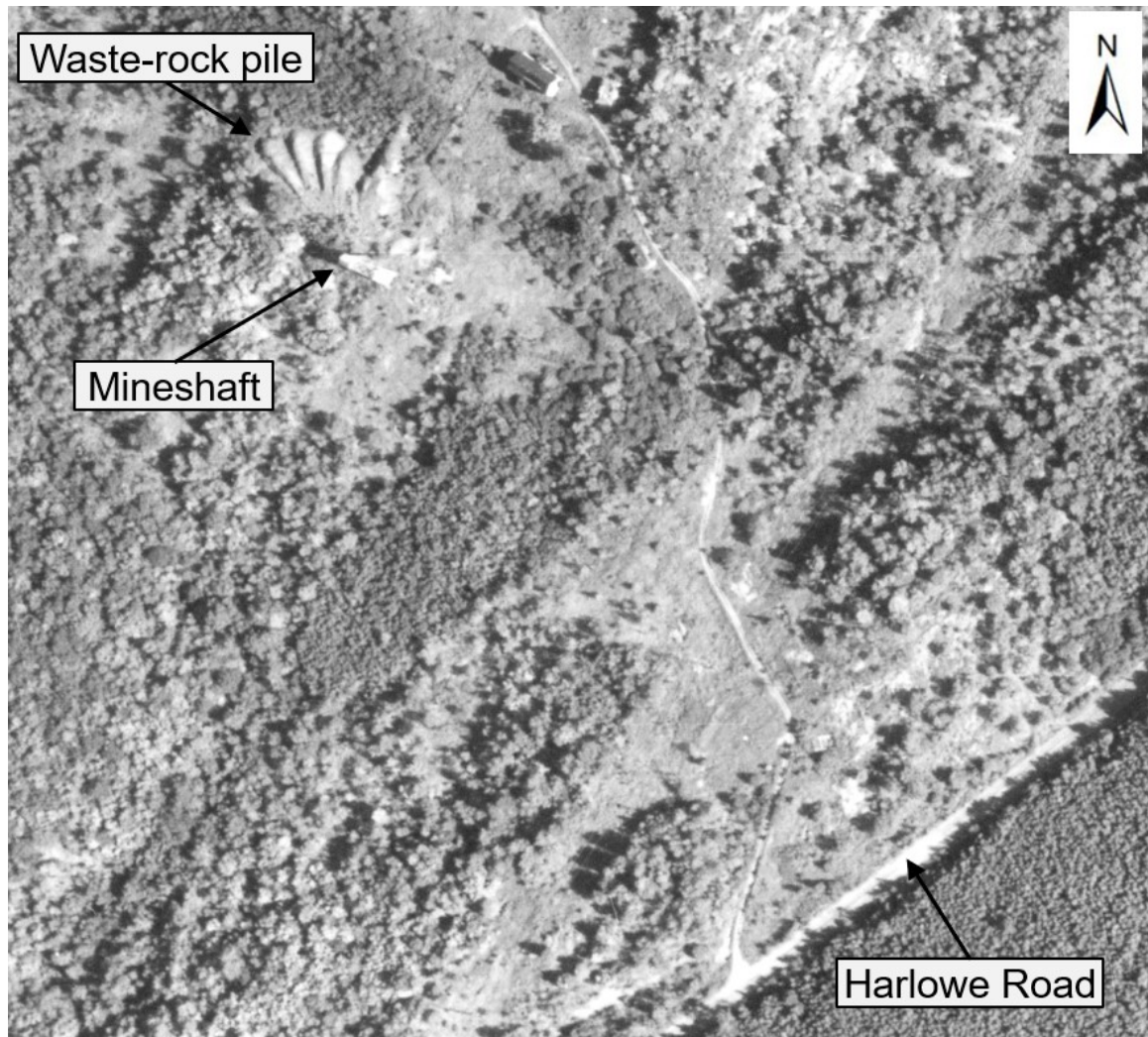


Figure 1.1: Historical imagery (1934) of Ore Chimney (Natural Resources Canada, 2016).

This study seeks to develop an improved understanding of the long-term mineral weathering in the waste-rock pile and the subsequent effects on metal transport. This has been accomplished by investigating the mineralogical and geochemical signatures that remain in this unsaturated aerobic system after 85+ years of weathering and how these signatures change spatially. Waste-rock mineral weathering in mining environments has been studied in the past (Langman et al., 2015); however, there are limited historical mine-waste dumps that allow the possibility of collecting empirical data to investigate long-term waste-rock weathering mechanisms. Likewise, few comprehensive studies have

complemented waste-rock mineralogical investigations with detailed porewater measurements to better describe chemical pathways observed in aerobic mine-waste systems (Atherton, 2017; Smith et al., 2021).

The research presented herein is divided into four chapters including the introduction, two research chapters, and the conclusion. Chapter two investigates mineral weathering processes using solid-phase mineralogical and geochemical data from optical microscopy, scanning electron microscopy with energy dispersive spectrometry (SEM-EDX), total carbon-sulfur (C/S) analysis, powdered X-ray diffraction (PXRD), and inductively coupled plasma atomic emission and mass spectrometry (ICP-AES/MS). Chapter three examines the porewater chemistry to complement metal-release mechanisms proposed in chapter two and investigate the overall mobility of metals throughout the pile. Results from spectrophotometry, probe measurements, anion chromatography (IC), and ICP-AES/MS were interpreted with PHREEQC geochemical modeling software to evaluate secondary mechanisms controlling the porewater chemistry and changes with depth. Chapter four summarizes conclusions and outlines future research.

Chapter 2: Mineralogy and Solid-Phase Geochemistry

2.1 Introduction

The increasing adaptability of modern civilization continues to accelerate the utility and extraction rate of Earth's resources, which has shaped the planet's surface dramatically since the industrial revolution (Hudson-Edwards et al., 2011). From the first recording of a streamlined iron ore smelting operation in 1737 near the St. Lawrence River, mining in Canada has remained a substantial component of the resource extraction industry (Cranstone, 2002). By volume, mining activities disturb and relocate more Earth materials than any other practice including the construction industry (ICOLD, 1996). In 2008, it was estimated that metal and non-metal mining in Canada (i.e. excluding oilsands mining) accumulated 217 million tonnes (Mt) of mine tailings and 256 Mt of waste rock that increased in production rate by 33% from 2001 (Statistics Canada, 2012). Large mining operations will often reuse waste rock to strengthen tailings impoundments (Wickland et al., 2006; Gorakhki and Bareither, 2017), to reinforce roads (Amrani et al., 2021), and even as a natural fertilizer (Ramos et al., 2017). However, the majority of waste rock is typically stockpiled as large volumes of unsaturated material and may produce low-quality drainage waters from chemical weathering at Earth's surface (Akcil and Koldas, 2006; Blowes et al., 2013).

Waste-rock piles are often formed by edge dumping that extends the footprint of the pile in different lateral directions over time (Pearce et al., 2016). Dumping material off the edges of the pile fractionates particles based on grain size with coarser material accumulating towards the base (Lahmira et al., 2016). Differences in particle settling rates typically reveal stratified layers of varying grain size, which has been characterized in greater detail in various settings (Azam et al., 2007; Cash, 2014). Geochemical signatures in waste-rock piles are often reflected by physical heterogeneities (Smith et al., 2013a), and recognizing these processes to evaluate risks associated with waste-rock weathering must consider both the chemical and physical aspects of mine-waste systems (Amos et al., 2015). Waste-

rock drainage waters affected by mineral weathering processes may percolate into neighbouring watersheds and necessitates a thorough understanding to inhibit the release of low-quality effluent and remediate contaminated waters at an industrial scale (Nordstrom and Alpers, 1999).

There have been many studies tailored to investigate mineral weathering and subsequent effects on water quality in mine tailings impoundments during the initial stages of development (Jamieson et al., 1995; Gleisner, 2005) and across multi-decadal timescales (Moncur et al., 2005; Gunsinger et al., 2006a; Hayes et al., 2014; Moncur et al., 2015; Elghali et al., 2021). However, there is less emphasis in the literature on evaluating these processes in aerobic waste-rock systems (Lefebvre et al., 2001; Sracek et al., 2004; Smith et al., 2013b; Langman et al., 2014). Delineating waste-rock weathering mechanisms, which change over time and govern in situ geochemical signatures is typically accomplished by applying an array of analytical techniques that may include optical microscopy, SEM-EDX, electron microprobe analysis (EMPA), total C/S, XRD, ICP-AES/MS, and X-ray absorption spectroscopy (XAS) (Smith et al., 2013a; Langman et al., 2014; Elghali et al., 2018; Langman and Moberly, 2018; Bao et al., 2020, Bao et al., 2021). However, the research typically incorporates a smaller portion of these analyses and is often focused solely on in situ metal release mechanisms into the porewaters. Furthermore, sampling approaches may not fully encapsulate the effects of waste-rock heterogeneity and many test piles have only weathered for one or two decades. Limited studies have applied a wide range of analytical techniques and combined solid-phase and aqueous-phase geochemical data to investigate metal mobility at different scales (Smith et al., 2021). Moreover, very few mine-waste investigations have examined mineral weathering processes beyond 50 years (Jeong and Lee, 2003; Moncur et al., 2009) and a comprehensive mineralogical and geochemical study on century-old Ore Chimney waste rock may help bridge the gap in the effects between short-term and long-term weathering.

Historical mining operations had higher cut-off grades for ore material, which typically led to increased concentrations of sulfide minerals in older waste dumps

compared to modern times (Kwong et al., 1997). Ontario's Ministry of Northern Development and Mines (2018) has documented over 5,000 abandoned mines across the province with potential environmental hazards that are not well understood. Therefore, it is important to recognize the long-term effects that waste-rock weathering can impose on metal transport and how the underlying processes may change over time to make properly informed decisions and develop impactful management strategies (Berghorn and Hunzeker, 2001). This chapter aims to investigate metal release mechanisms after ~100 years of weathering at Ore Chimney while capturing the effects of waste-rock heterogeneity.

2.2 Methods

2.2.1 Field Methods

During the first week of November 2019, samples of waste-rock material were collected from three vertical transects of the ~10 kt waste-rock pile at the Ore Chimney site. Vertical trenches were spaced out approximately 10 metres from each other and from the edges of the pile. In reference to the surface of the pile, three vertical transects were dug to a depth of five metres, approximately corresponding to the total height of the pile above the original ground surface. Samples of in situ waste-rock material were collected every 0.5 m along an undisturbed sidewall of each trench using a trowel and 5 to 6 kg of material was transferred into 2721 mL *Nasco Whirl-Pak* sample bags. Waste-rock pile deconstruction was facilitated using a 4.5 tonne Bobcat E42 mini-excavator. The material sampled at each depth was subdivided into two classes, designated for hard-rock geochemistry and porewater chemistry investigations, respectively. Furthermore, two depth locations in each trench were designated for collecting duplicate samples (Figure 2.1). Samples of waste-rock material were stored in a freezer at -22°C following each day of field work in preparation for subsequent laboratory analysis.

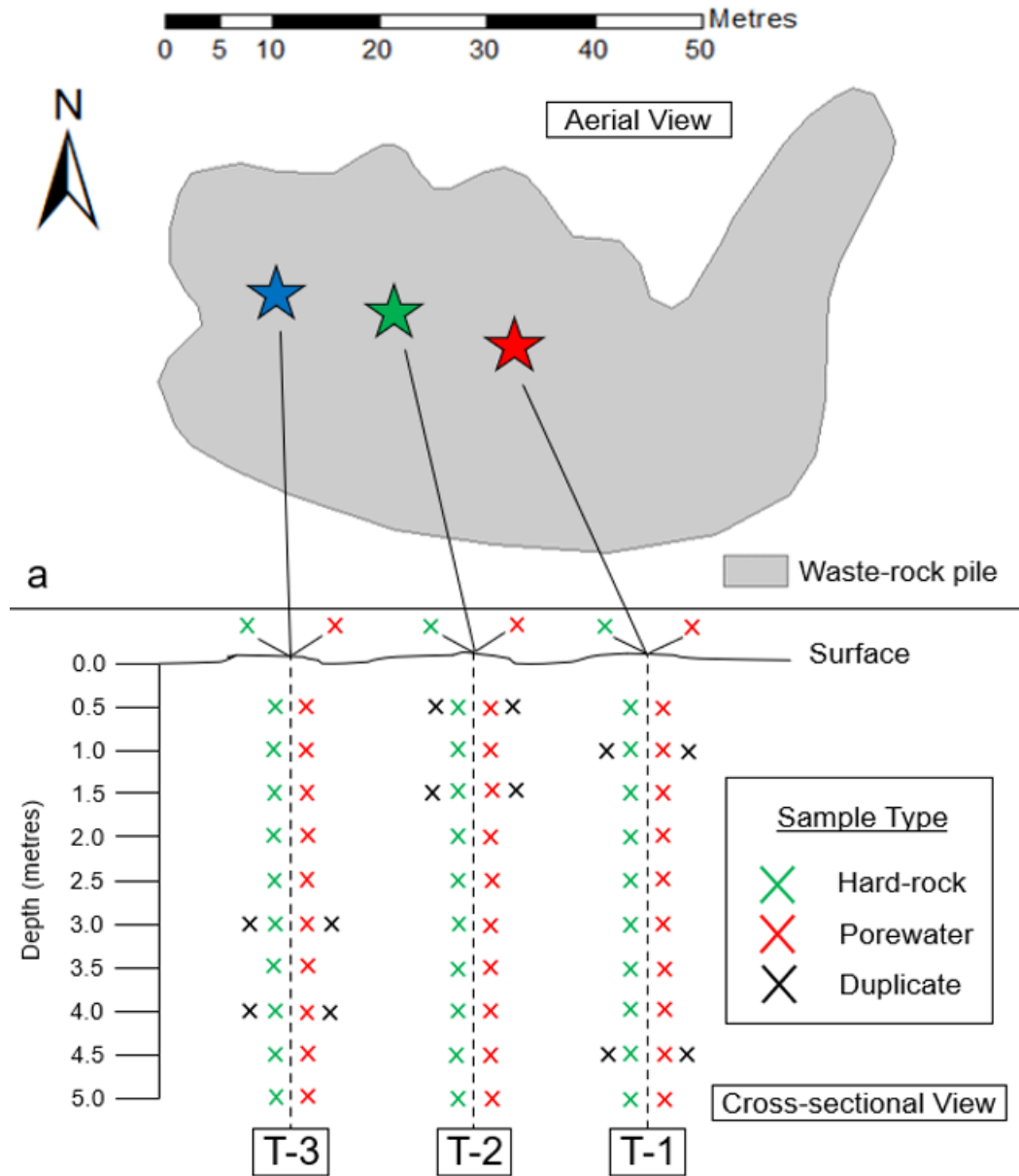


Figure 2.1: a) Aerial schematic of the waste-rock pile with location of vertical transects (stars; T = trench), b) Cross-sectional view of sampling locations (8× vertically exaggerated).

2.2.2 Sample preparation

Samples of waste-rock material were air-dried for 48 hours and passed through a two-millimetre sieve. The particles of waste-rock material that passed through the sieve were air dried for an additional 24 hours and the > 2.0 mm fraction was

immediately returned to the freezer for future considerations. To contrast weathering on different grain size, air-dried samples less than two millimeters in diameter were passed through a second sieve with a 0.5 mm mesh size. Waste-rock material 0.5 to 2.0 mm in diameter was designated as the coarse-grained fraction and material < 0.5 mm was designated as the fine-grained fraction. Sieved waste-rock material was passed through a *Gilson Model: SP-33* stainless steel universal riffle splitter and material was split to a desired sample volume of 110 mL for archiving and subsample freeze-drying (ASTM C702/C702M-11, 2011).

Samples of waste-rock material were transferred into 125 mL VWR® polypropylene wide mouth bottles and affixed with 20 µm filter paper for modified lids. To ensure that sample moisture was removed, samples were freeze dried at -87°C and 0.5 mbar for 24 hours using a *Labconco FreeZone 2.5 L* Benchtop Freeze Dry System with a 12-port drying manifold. A ~40 g subsample of freeze-dried material for polished grain mount preparation was obtained by applying the ASTM quartering method (ASTM C702/C702M-11, 2011). The remaining sample material was crushed and homogenized for quantitative geochemical analyses. Freeze-dried ~300 g subsamples were powdered to < 75 µm using a (*Rocklabs*) stainless steel standard ring mill. Pulverised samples were submitted for PXRD, total (C/S) analysis, and ICP-AES/MS. Non-pulverised freeze-dried samples were prepared for optical microscopy and SEM-EDX.

2.2.3 Analytical Methods

Grain mounts of freeze-dried waste-rock material were prepared on glass slides (45 mm × 25 mm), immersed in a non-aqueous epoxy, and polished to a thickness of 60 µm. Grain mounts were prepared to a thickness of 60 µm instead of 30 µm to reduce the likelihood of obscurities and better preserve entire grains of fine-grained ore minerals (Langman et al., 2015). The ore mineralogy of the polished grain mounts was characterized under reflected light using a *Nikon OPTIPHOT-POL* polarizing microscope connected to a *JENOPTIK ProgRes®* microscope camera. To assess the extent of waste-rock sulfide mineral alteration from prolonged exposure above ground surface, the average condition of sulfide grains

in coarse-grained samples was interpreted using an empirical ranking system (Table 2.1).

Table 2.1: Sulfide mineral oxidation ranking.

Rank	Description of average oxidation of sulfide grain
1	Pristine rim (0 to 10% of mineral area)
2	Thinly weathered rim (10 to 20% of mineral area)
3	Moderately weathered rim (20 to 30% of mineral area)
4	Extensively weathered rim (>30% mineral area)

With the average condition of each sulfide mineral in the coarse-grained fraction ranked, a sulfide alteration index (SAI) was developed to interpret the differences in weathering condition between the different sulfide minerals commonly found throughout the waste rock (Table 2.2). The SAI is based on similar scales in previous studies of mine-waste sulfide mineral weathering (Blowes and Jambor, 1990; Moncur et al., 2005, Moncur et al., 2009) but was tailored for the sulfide mineral assemblage ubiquitous to the Ore Chimney waste-rock pile and included pyrite (FeS_2), chalcopyrite (CuFeS_2), and sphalerite (ZnS).

Table 2.2: Sulfide alteration index (SAI) of the Ore Chimney waste-rock pile.

Index score	Description of alteration
4	Sulfide minerals near complete oxidation, traces of pyrite and chalcopyrite remain, no sphalerite present
3	Sphalerite is sparse and remaining grains are heavily oxidized, pyrite grains show alteration
2	Sphalerite grains show a thin oxidation rim with the mineral core relatively preserved, pyrite and chalcopyrite show minimal alteration
1	Sphalerite is common and relatively unweathered, pyrite and chalcopyrite grains are pristine

Various mineral phases and subsequent regions of suspected chemical alteration in polished grain mounts representing the fine-grained fraction of sampled waste-rock material were identified and prepared for SEM-EDX. Chemical analysis was performed using energy dispersive X-ray spectrometry with an *Oxford* silicon drift

detector energy dispersive spectrometer (SDD-EDS) ultra-thin window detector coupled with a *JSM-IT500 JEOL* scanning electron microscope. Furthermore, secondary mineral formation and subsequent mineral structures were interpreted with digital back-scattered electron (BSE) high-resolution imagery.

PXRD was performed for bulk mineralogical analyses at a (2θ) scan rate of $0.5^\circ/\text{minute}$ from 5 to 85° at the University of Ottawa using a *Rigaku Ultima IV* Diffractometer. Peak data generated from PXRD was post-processed at Carleton University using © PANalytical HighScorePlus software (version 4.7.0.24755). The primary mineral phases were identified in reference to the international centre for diffraction database (ICDD) and the amplitudes of peak data corresponded to mineral concentrations, quantified in relation to external standards developed in the ICDD. A conservative detection limit for PXRD mineral quantification and SEM-EDX elemental composition was estimated at 2 wt.% (Aguilar et al., 2019).

The total C/S analysis was conducted at the University of Waterloo using an *ELTRA CS-2000* Carbon/Sulfur analyzer with an induction furnace and infrared detector. The conservative detection limit for the *ELTRA CS-2000* system was estimated at 0.02 wt.% (Ripley et al., 2011). Inorganic carbon and sulfur content in a material sample are typically measured as a mass percentage value (wt.%). Post-processing data from total C/S analysis assumes that the S content is fixed as pyrite ($FeS_{2(s)}$) and the inorganic carbon content is fixed as calcite ($CaCO_{3(s)}$). The acidification potential (AP) and neutralization potential (NP) was interpreted under the assumption that one mole of calcite (equation 5) neutralizes one mole of sulfur (equation 3). Therefore, the AP (8) and NP (9) of a sample can be estimated (Sobek, 1978; Blowes et al., 2013).

$$AP = \text{sulfur content of sample (kg/tonne)} \times \frac{M_w \text{ of calcite (g/mol)}}{M_w \text{ of sulfur (g/mol)}} \quad (8)$$

$$NP = \text{carbon content of sample (kg/tonne)} \times \frac{M_w \text{ of calcite (g/mol)}}{M_w \text{ of carbon (g/mol)}} \quad (9)$$

Acidification and neutralization potential of waste-rock samples were classified according to INAC (1993). Waste-rock samples with NP:AP ratios less than 1:1 were described to have a “potential acid generating” (PAG) ability, NP:AP ratios between 1:1 and 3:1 were considered to have an “uncertain acid generating” (UAG) potential, and NP:AP ratios greater than 3:1 were termed “non-acid generating” (NAG) (Smith et al, 2013a).

ICP-AES/MS was performed at the Geochemistry Laboratory at the University of Ottawa. Freeze-dried and powdered waste-rock samples were subjected to a two-step acid digestion procedure. A 50 mg subsample of sediment was weighed in a 7 mL Teflon vial. Ultra-pure nitric acid (0.5 mL) and hydrochloric acid (1.5 mL) (aqua regia) were added to the vial and settled for one hour. The loosely capped Teflon vials were heated at 110°C for 12 hours. The solution evaporated to near dryness and the residue was re-dissolved in 0.5 mL of nitric acid and 2 mL of Fisher Optima Grade and MilliQ 18.2 Ω deionized water. Contents were transferred into pre-weighed 15 mL plastic vials and centrifuged. The clear portion of the solution containing major cations (i.e., Al, Ca, Mg) was quantitatively transferred to another 15 mL vial and diluted with deionized water to a mass of 10.0 g. Remaining residue mostly contained insoluble silicates and was transferred back into the 7 mL Teflon vial and digested with ultra-pure hydrofluoric acid (0.5 mL HF) and nitric acid (0.5 mL HNO₃). Contents were evaporated to near dryness and residual hydrofluoric acid was removed by adding a second 0.5 mL portion of nitric acid and repeating the drying procedure. The residue was re-dissolved in 0.5 mL of nitric acid and 2 mL of deionized water and diluted to a mass of 10.0 g. (N. De Silva, personal communications, 2021).

To compare metal concentrations between digestions representing more soluble solid phases (i.e. aqua regia) and less soluble silicate minerals (i.e. HF and HNO₃), solutions from both steps of the acid digestion procedure were analyzed. Major cations were measured by ICP-AES using an *Agilent 5110 SVDV CCD* atomic emission spectrometer and trace metal concentrations were determined by ICP-MS using an *Agilent 8800 QQQ triple quadrupole* mass spectrometer. Both ICP-

AES and ICP-MS measurements were calibrated using external standards and all calibration standards were prepared using an ultra-pure 1% nitric acid solution (N. De Silva, personal communications, 2021).

2.3 Results

Visual observations during excavation of the vertical transects at Ore Chimney revealed that the waste-rock pile (WRP) slightly exceeded five metres in depth at trench 1. The beginning of a transitional boundary between the waste-rock pile and natural overburden material was estimated between 4.5 to 5.0 metres deep in trench 2 and between 4.0 to 4.5 metres deep in trench 3. The subsequent geochemical depth plots indicate these non-discrete boundary estimations accordingly as “WRP boundary” and the samples located above these boundaries were referred to as the waste-rock material. Likewise, only the samples representing waste-rock material (i.e. excluding the samples below the WRP boundary) were included in statistical comparisons and the annotated results summary unless indicated otherwise.

The results presented herein compare fine-grained and coarse-grained materials, spatial differences within a given trench (i.e. vertical trends), and differences in measurements between trenches, but only trends and differences with a statistical significance are reported. Vertical trends were interpreted from a two-tailed Pearson correlation analysis with 95% confidence and compared to critical Pearson correlation (R^2_{critical}) values of 0.553, 0.576, and 0.602 for trenches 1, 2, and 3, respectively (Degrees of Freedom = $n - 2$) (Weatherington et al., 2012). Remaining statistical analyses were conducted as rank sum two-tailed t-tests calculating P-values (α) comparing fine- and coarse-grained samples of individual trenches (n = sample size = 13 in trench 1, n = 12 in trench 2, and n = 11 in trench 3). Additional t-tests that compared samples between trenches did not include data from duplicate samples and only considered samples between 0.0 to 4.0 m depth to account for the transition between waste rock and overburden material observed in trenches 2 and 3 (n = 9). Vertical trends with insignificant correlation coefficients ($R^2_{\text{calculated}} < R^2_{\text{critical}}$) and t-test comparisons of population means (μ) with standard

deviations (σ) yielding no statistical difference ($\alpha > 0.05$) were interpreted as such and not reported herein.

2.3.1 X-ray Diffraction: Phase Identification and Quantitation

Quartz concentrations in the waste-rock material ranged from 35 to 62 wt.% (coarse-grained $\mu = 48.1$, $\sigma = 9.9$; fine-grained $\mu = 42.9$, $\sigma = 7.2$) in trench 1, from 31 to 51 wt.% (coarse-grained $\mu = 42.2$, $\sigma = 5.5$; fine-grained $\mu = 37.3$, $\sigma = 3.8$) in trench 2, and from 33 to 52 wt.% (coarse-grained $\mu = 45.0$, $\sigma = 5.3$; fine-grained $\mu = 41.6$, $\sigma = 6.0$) in trench 3 (Fig. 2.2a - c). The lowest quartz concentrations of the fine-grained fraction were observed in trench 2 and were highest in trench 1 with a mean difference of 7.9 wt.% ($\alpha = 0.05$; 0.0 to 4.0 m depth). Quartz was the only mineral phase that consistently measured higher concentrations in the coarse-grained fraction of waste-rock samples throughout all three trenches. Quartz concentrations were statistically higher in the coarse-grained fraction than the fine-grained fraction by mean differences of 5.2, 4.9, and 3.4 wt.% in trenches 1, 2, and 3 ($\alpha = 0.002$, 0.006, and 0.03, respectively).

Oligoclase concentrations ranged from 10 to 25 wt.% (coarse-grained $\mu = 16.8$, $\sigma = 3.9$; fine-grained $\mu = 17.8$, $\sigma = 4.0$) in trench 1, from 17 to 25 wt.% (coarse-grained $\mu = 20.2$, $\sigma = 2.6$; fine-grained $\mu = 21.9$, $\sigma = 2.5$) in trench 2, and from 13 to 28 wt.% (coarse-grained $\mu = 17.9$, $\sigma = 3.2$; fine-grained $\mu = 21.1$, $\sigma = 5.7$) in trench 3 (Fig. 2.2d - f). The lowest oligoclase concentrations of the coarse-grained fraction were observed in trench 1 and were highest in trench 2 with a mean difference of 4.6 wt.% ($\alpha = 0.04$). Oligoclase concentrations in the fine-grained fraction were statistically higher than the coarse-grained fraction in trenches 2 and 3 with mean differences of 1.8 and 3.2 wt.% ($\alpha = 0.05$ and 0.02).

Hornblende concentrations ranged from 5 to 12 wt.% (coarse-grained $\mu = 8.6$, $\sigma = 2.1$; fine-grained $\mu = 8.3$, $\sigma = 2.3$) in trench 1, from 7 to 16 wt.% (coarse-grained $\mu = 10.7$, $\sigma = 2.4$; fine-grained $\mu = 9.3$, $\sigma = 1.6$) in trench 2, and from 5 to 15 wt.% (coarse-grained $\mu = 9.2$, $\sigma = 2.3$; fine-grained $\mu = 8.8$, $\sigma = 2.5$) in trench 3 (Fig. 2.2g - i). Hornblende concentrations within the waste-rock material were relatively consistent between trenches and did not vary statistically with depth.

Biotite concentrations ranged from 9 to 27 wt.% (coarse-grained $\mu = 14.6$, $\sigma = 4.2$; fine-grained $\mu = 16.7$, $\sigma = 6.4$) in trench 1, from 11 to 24 wt.% (coarse-grained $\mu = 14.8$, $\sigma = 2.5$; fine-grained $\mu = 18.2$, $\sigma = 3.6$) in trench 2, and from 10 to 20 wt.% (coarse-grained $\mu = 12.9$, $\sigma = 2.3$; fine-grained $\mu = 16.2$, $\sigma = 2.9$) in trench 3 (Fig. 2.2j - l). The biotite mineral phase was predicted to host Ti, Mn, and Zn at trace atomic proportions of 0.1, 0.01, and 0.01, respectively. Among the mineral phases identified by PXRD, biotite most consistently measured higher concentrations in the fine-grained fraction of waste-rock samples throughout all three trenches. Biotite concentrations in the fine-grained fraction were statistically higher than the coarse-grained fraction with mean differences of 2.1, 3.3, and 3.3 wt.% in trenches 1, 2, and 3 ($\alpha = 0.02$, 0.0003, and 0.0004, respectively).

Chlorite concentrations ranged from 3 to 7 wt.% (coarse-grained $\mu = 5.3$, $\sigma = 1.1$; fine-grained $\mu = 5.5$, $\sigma = 1.0$) in trench 1, from 3 to 6 wt.% (coarse-grained $\mu = 4.1$, $\sigma = 0.9$; fine-grained $\mu = 4.8$, $\sigma = 0.8$) in trench 2, and from 3 to 7 wt.% (coarse-grained $\mu = 4.9$, $\sigma = 1.0$; fine-grained $\mu = 4.9$, $\sigma = 1.2$) in trench 3 (Fig. 2.3a - c). Chlorite concentrations within the waste-rock material were relatively consistent between trenches and did not vary statistically with depth.

PXRD analyses had a conservative detection limit of 2 wt.%. As such, calcite often measured concentrations < 2 wt.% but were still incorporated in statistical calculations for simplicity, but with less emphasis in the discussion. Calcite concentrations ranged from below the detection limit to 6 wt.% (coarse-grained $\mu = 2.7$, $\sigma = 1.0$; fine-grained $\mu = 3.8$, $\sigma = 2.0$) in trench 1, from below detection to 3 wt.% (coarse-grained $\mu = 2.0$, $\sigma = 0.4$; fine-grained $\mu = 2.2$, $\sigma = 0.6$) in trench 2, and below detection of 2 wt.% (coarse-grained $\mu = 1.3$, $\sigma = 0.5$; fine-grained $\mu = 1.5$, $\sigma = 0.5$) in trench 3 (Fig. 2.3d - f). Although often measuring below detection, calcite concentrations in the coarse-grained fraction were highest in trench 1 and lower in trenches 2 and 3 by mean differences of 0.6 and 1.3 wt.% ($\alpha = 0.05$ and 0.04). The same trends were observed in the fine-grained fraction with mean differences of 1.5 and 2.2 wt.% ($\alpha = 0.02$ and 0.04). Calcite concentrations in the

fine-grained fraction were higher than the coarse-grained fraction in trench 1 with a mean difference of 1.1 wt.% ($\alpha = 0.003$).

Dolomite concentrations ranged from below detection to 6 wt.% (coarse-grained $\mu = 2.9$, $\sigma = 1.4$; fine-grained $\mu = 2.3$, $\sigma = 1.4$) in trench 1, from 2 to 8 wt.% (coarse-grained $\mu = 4.6$, $\sigma = 1.5$; fine-grained $\mu = 4.0$, $\sigma = 1.1$) in trench 2, and from 3 to 13 wt.% (coarse-grained $\mu = 7.0$, $\sigma = 3.2$; fine-grained $\mu = 4.6$, $\sigma = 1.2$) in trench 3 (Fig. 2.3g - i). Dolomite concentrations in the coarse-grained fraction were observed to be lowest in trench 1 and statistically higher in trenches 2 and 3 by mean differences of 2.1 and 4.4 wt.% ($\alpha = 0.004$ and 0.007). The same trend was observed for the fine-grained fraction with mean differences of 1.9 and 2.5 wt.% ($\alpha = 0.01$ and 0.002). Dolomite concentrations in the coarse-grained fraction were higher than the fine-grained fraction in trench 3 by a mean difference of 2.4 wt.% ($\alpha = 0.01$).

Pyrite, ferroan sphalerite, and galena were the only sulfide phases identified from PXRD measurements. Due to their trace abundance, individual sulfide phases were difficult to quantify. Therefore, the sulfide mineral phases were presented herein as the summation of pyrite, ferroan sphalerite, and galena measurements. The sulfide mineral content typically measured below detection of 2 wt.% and ranged from 0 to 3 wt.% in trench 1, from 1 to 4 wt.% in trench 2, and from 1 to 4 wt.% in trench 3 (Fig. 2.3j - l). There was no relationship between concentration and depth for any grain fraction of the cumulative sulfide mineral phases identified by PXRD.

The analytical sensitivity of PXRD analysis was estimated at ~2 wt.% (Aguilar et al., 2019), which creates difficulties in reporting the presence of trace mineral phases with sufficient confidence. However, estimations of carbonate (i.e. calcite and dolomite) and sulfide mineral wt.% from PXRD analysis was comparable to ranges observed from total C/S analysis (Fig. 10a - c). Any sulfide depth trends, differences in content between trenches, and differences between coarse and fine-grained samples in the same trench were better interpreted from total [C] and [S]

readings due to the higher sensitivity and no cumulative error associated with the reported measurements.

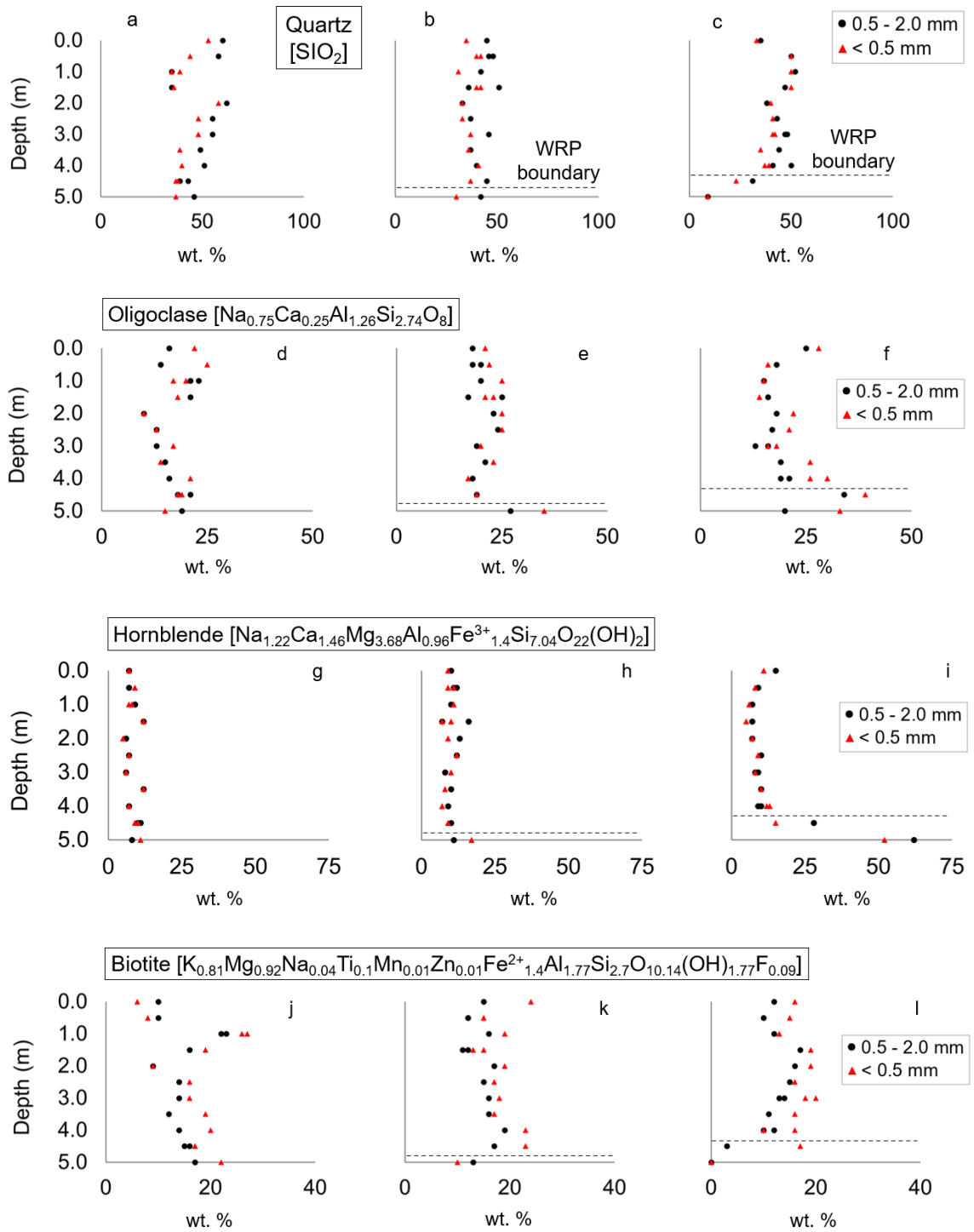


Figure 2.2: Major mineral phase depth plots for trench 1 (left), trench 2 (middle), and trench 3 (right).

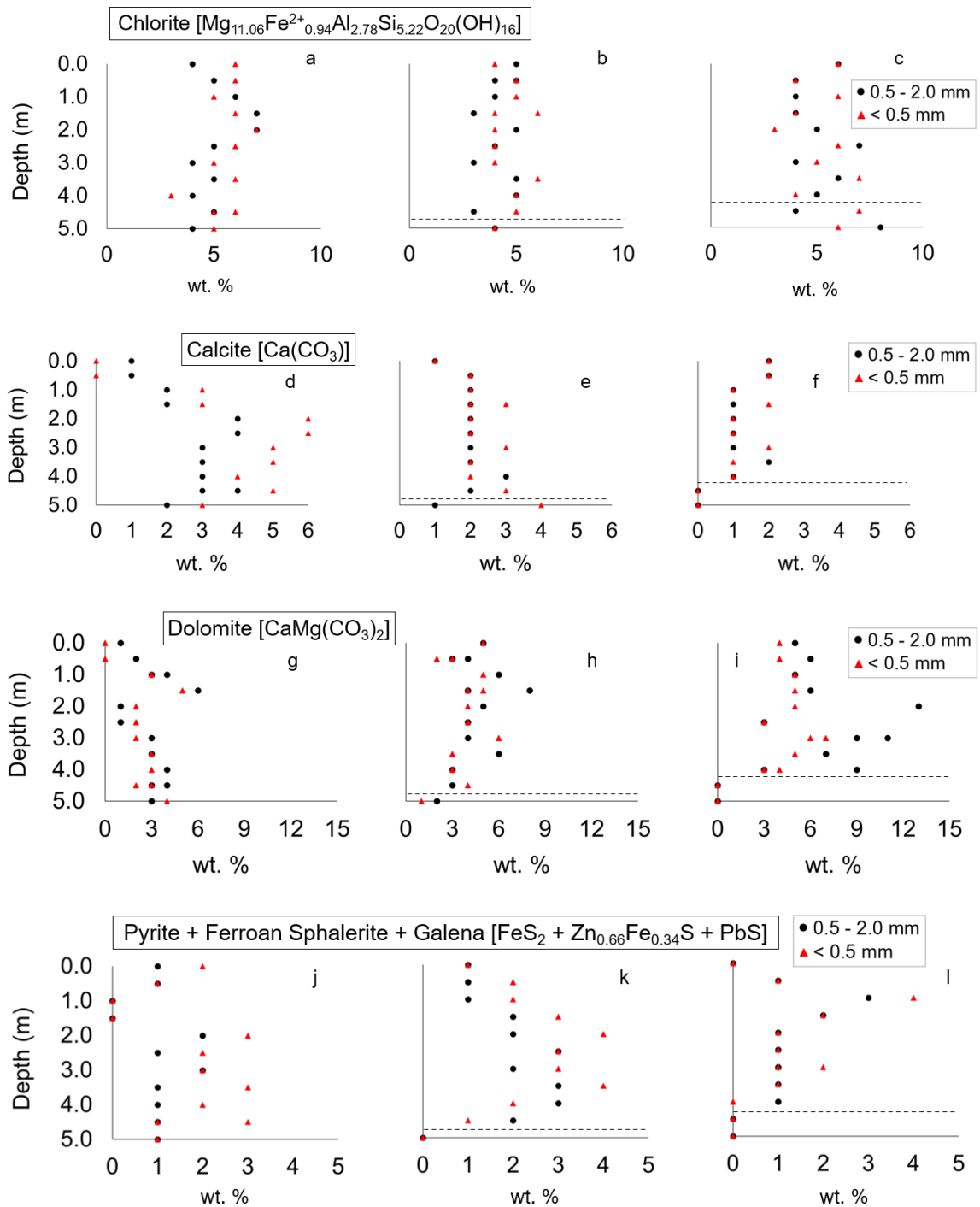


Figure 2.3: Minor mineral phase depth plots for trench 1 (left), trench 2 (middle), and trench 3 (right).

2.3.2 Ore Petrography

The four most common sulfide minerals from high to low relative abundance in the polished grain mounts were sphalerite (ZnS) > galena (PbS) > pyrite (FeS_2) > chalcopyrite (CuFeS_2) and were analyzed for the degree of oxidation based on the empirical ranking scheme presented in Table 2.1. Each polished grain mount (representing a sample of waste-rock material) contained approximately 3 to 8 pyrite and chalcopyrite grains (each) and 5 to 12 sphalerite and galena grains (each). Sulfide mineral grains within the same grain mount often showed a slight range in weathering and results are presented as an average rank for each sulfide mineral for each sample (one sample for each depth location in each trench; $n = 13$ for trench 1, $n = 12$ for trench 2, and $n = 11$ for trench 3). All four sulfide minerals showed some indication of weathering (Fig. 2.4a - l). The average degree of weathering for the four common sulfide minerals was relatively consistent between trenches and did not vary significantly with depth. Chalcopyrite displayed the lowest average degree of weathering with mineral grains typically assigned a rank of 1, indicating a very thin zone of alteration. In many instances, pyrite grains showed a similar alteration range to chalcopyrite; however, displayed a slightly higher average degree of weathering (i.e. a higher proportion of samples assigned an average rank of 2). In general, galena grains weathered to a similar extent as pyrite; however, exhibited a higher average range in weathering throughout each trench with more samples assigned a rank of 3. Sphalerite mineral grains were observed to be weathered to the highest extent with all samples given an average rank of 2 or 3.

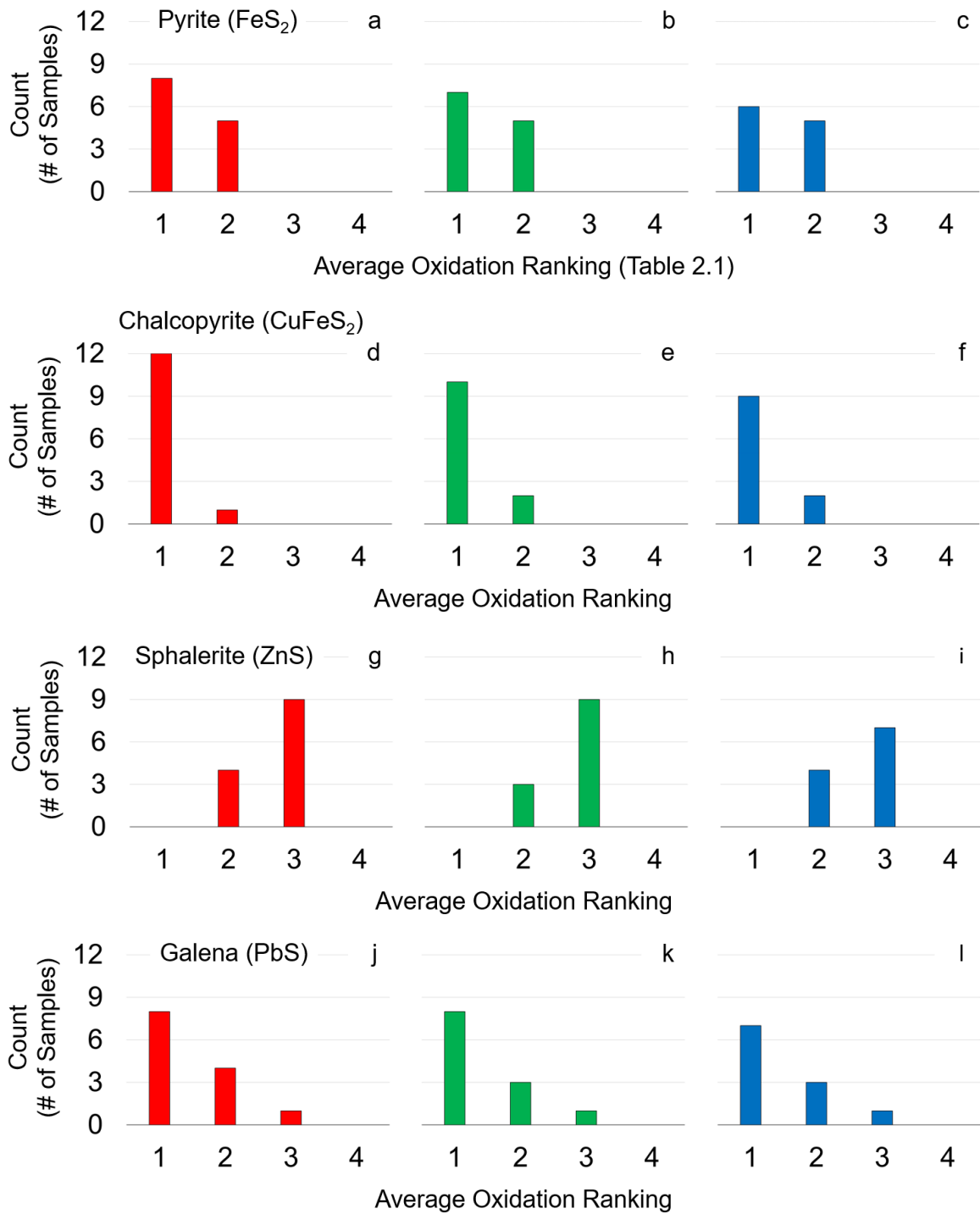


Figure 2.4: Average pyrite, chalcopyrite, sphalerite, and galena oxidation ranking for each waste-rock sample location for trench 1 (left), trench 2 (middle), and trench 3 (right).

The variation in the degree of sulfide mineral weathering of individual grains within the same sample reflected the overall variation in the average ranks distributed between sample locations. For example, the sample representing 4.5 m depth in trench 1 revealed pyrite grains that were oxidized < 10% of the mineral area (rank of 1; Fig. 2.5a) and 10 to 20% of the mineral area (rank of 2; Fig. 2.5b). Likewise, pyrite grains with an oxidation rank of 1 (Fig. 2.5e) and a rank of 2 (Fig. 2.5c, d, and f) were observed from samples representing different depths in different trenches. Chalcopyrite mineral grain oxidation ranks also ranged from 1 (Fig. 2.5h, i, k, and l) to 2 (Fig. 2.5g and j); however, most grains had an average condition of 1. Sphalerite mineral grain condition ranged from 2 (Fig. 2.5m, p, and r) to 3 (Fig. 2.5n, o, and q) and the average galena grain condition varied at 1 (Fig. 2.5s and u), 2 (Fig. 2.5t, v, and w), and 3 (Fig. 2.5x).

Sulfide Alteration Index (SAI) scores were assigned based on the overall degree of weathering, taking into account the suite of sulfide minerals, their abundance, and their average oxidation rank (Table 2.2). Galena was omitted from SAI interpretations due to a “persistence effect” described by Moncur et al (2009). The overall magnitude of weathering of the Ore Chimney waste-rock material was defined primarily by the prevalence and condition of sphalerite grains, which exhibited a combination of thinly weathered, moderately weathered, and extensively weathered rims. In addition, other sulfide minerals such as pyrite and chalcopyrite were noticeably less weathered than sphalerite. In general, the SAI scores for each sample ranged from 2 to 3 and showed no significant change with depth nor between trenches.

Systematic ranking of sulfide mineral weathering as described above was completed on the coarse-grained fraction of waste-rock samples. However, the average extent of sulfide mineral oxidation in the fine-grained fraction was also observed to be highest in sphalerite grains (Fig. 2.6m - r) and lowest in chalcopyrite grains (Fig. 2.6g - l). In addition, individual sphalerite, pyrite (Fig. 2.6a - f), and galena (Fig. 2.6s - x) grains also displayed a range in alteration within the same samples and between sample locations. Intricacies in the preparation of polished

grain mounts and the inherent weathering variability of sulfides made it difficult to assess any distinct difference in mineral reactivity between coarse and fine-grained fractions. Pyrite, chalcopyrite, sphalerite, and galena were common in both grain fractions and the corresponding condition of mineral alteration rims between grain size ranges was similar in most cases. On average, the number of individual sulfide mineral grains were higher in the fine-grained fraction and sometimes presented a greater intra-sample variability in mineral alteration. Furthermore, pyrite fracturing was more apparent in the fine-grained fraction and pyrite mineral cores were often observed to be smaller (Fig. 2.6d and e).

In addition to pyrite, chalcopyrite, sphalerite, and galena, the Ore Chimney waste-rock material contained additional ore minerals that were found only in a few sample locations. These mineral phases included a (Cu,Sb)S phase (potentially famatinite), a (Cu,Sb,Ag)S phase (potentially freibergite), arsenopyrite (FeAsS), magnetite (Fe₃O₄), ilmenite (FeTiO₃), rutile (TiO₂), and titanite (CaTiSiO₅) (Fig. 2.7a - f). Although below the detection limit, arsenopyrite, magnetite, and ilmenite measured trace concentrations of Co (< 1 wt.%). Each of these trace ore mineral phases were observed to be altered to some extent; however, they were not abundant enough throughout the pile to accurately supplement assessments of overall sulfide mineral alteration.

Sulfide mineral investigations of the fine-grained fraction of waste-rock material under SEM-EDX revealed that unweathered pyrite predominantly consisted of Fe and S with concentrations below detection (< 1.0 wt.%) of mercury (Hg), cobalt (Co), and nickel (Ni). Alteration zones of pyrite grains were observed as a Fe-oxide phase containing Pb, Zn, and sometimes Cu (Fig. 2.8a and b). Pyrite mineral grains also exhibited various degrees of fracturing, which revealed increased zones of alteration and were increasingly apparent with smaller grain size. Unweathered chalcopyrite grains were composed of Cu, Fe, and S with no detectable trace concentrations of other metals. Alteration zones of chalcopyrite were mostly comprised of a Fe-oxide phase with detectable concentrations of Pb, Zn, and Cu. Measured concentrations of Cu in unweathered chalcopyrite cores

ranged from 30 to 36 wt.% and were significantly lower within the alteration zones ranging from 5 to 15 wt.% (Fig. 2.8c and d).

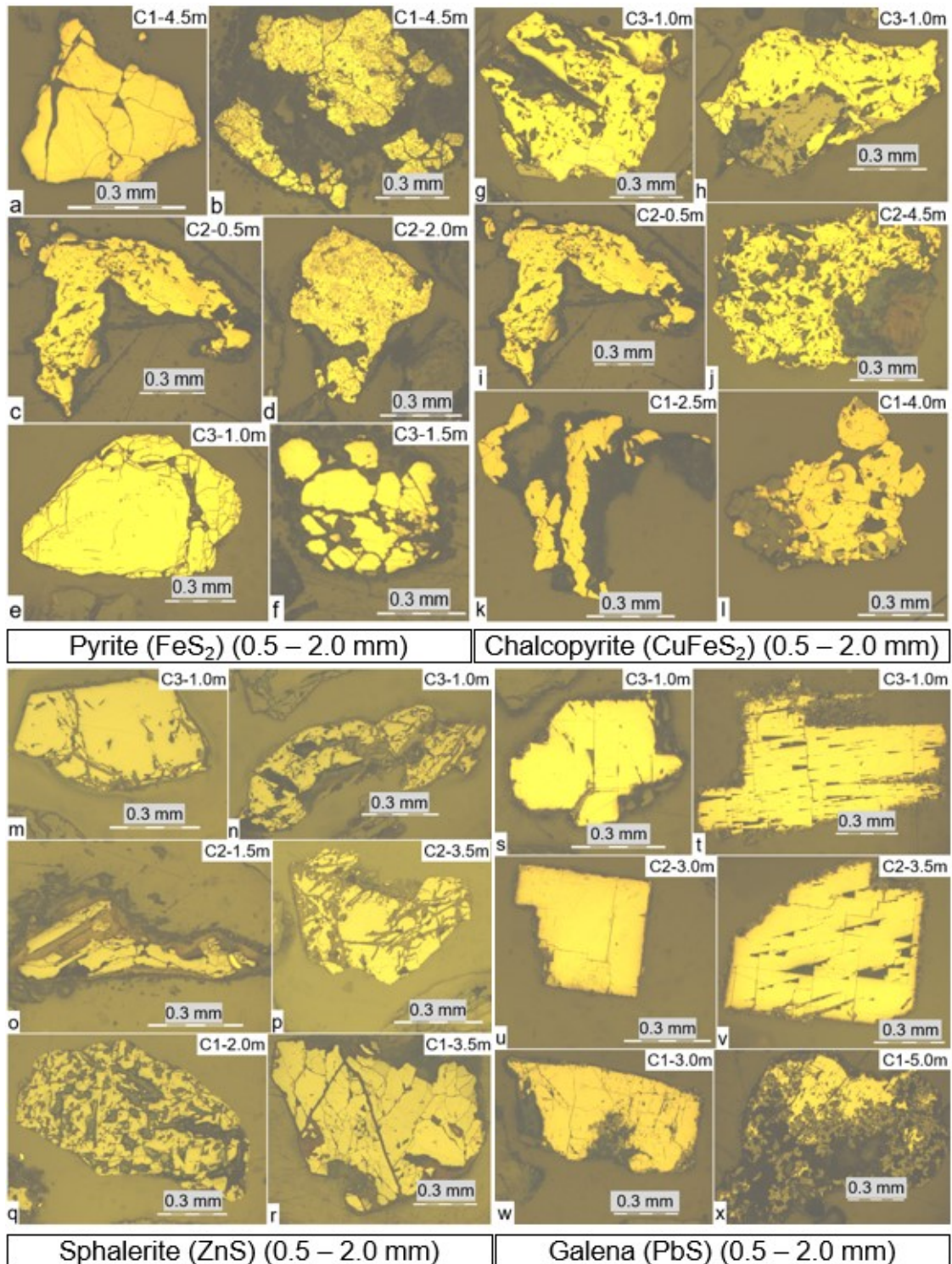


Figure 2.5: Common ore minerals under reflected light (0.5 to 2.0 mm grain size) (i.e. C1 refers to coarse grain fraction at trench 1).

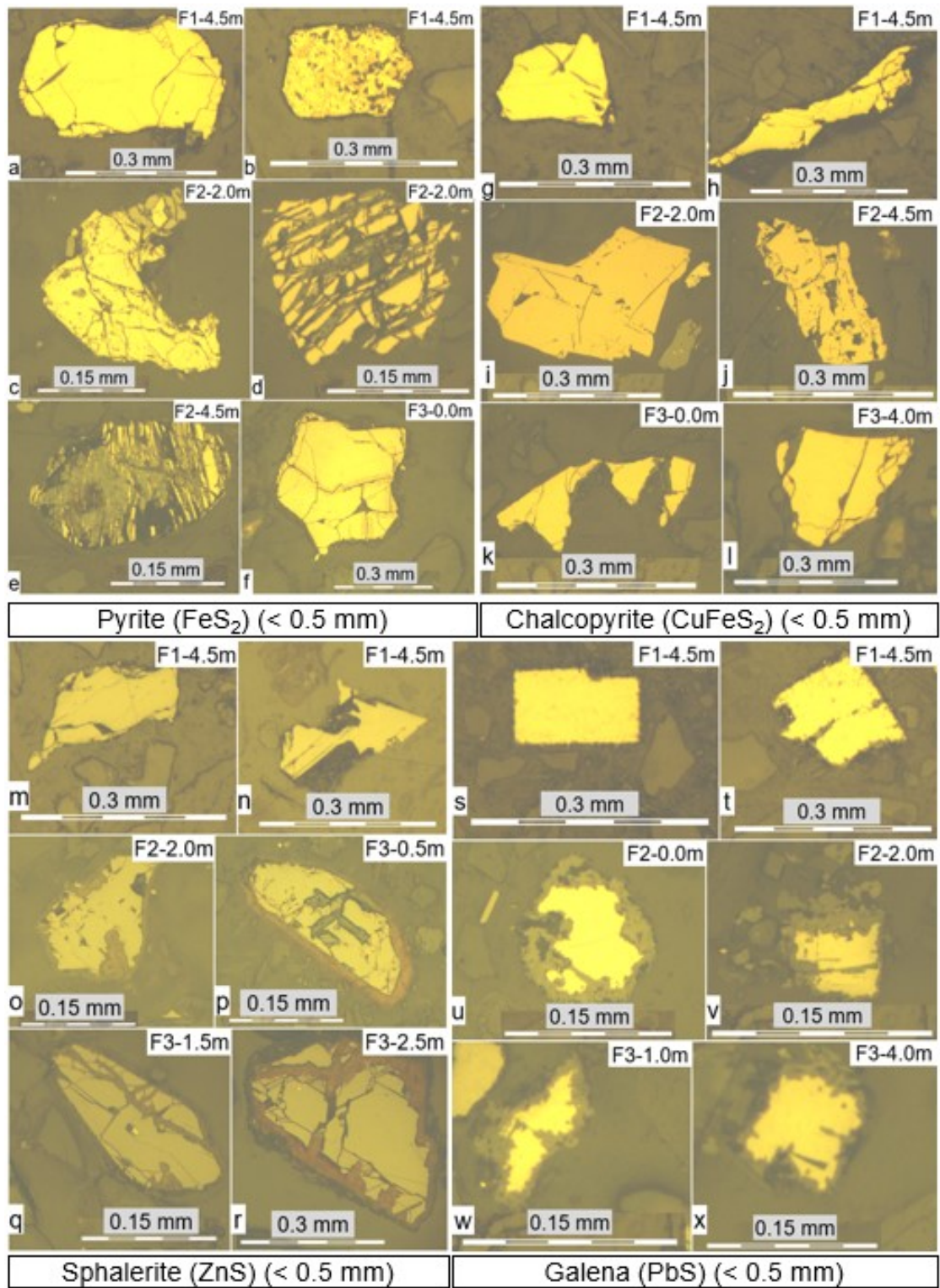


Figure 2.6: Common ore minerals under reflected light (< 0.5 mm grain size) (i.e. F3 refers to fine grain fraction at trench 3).

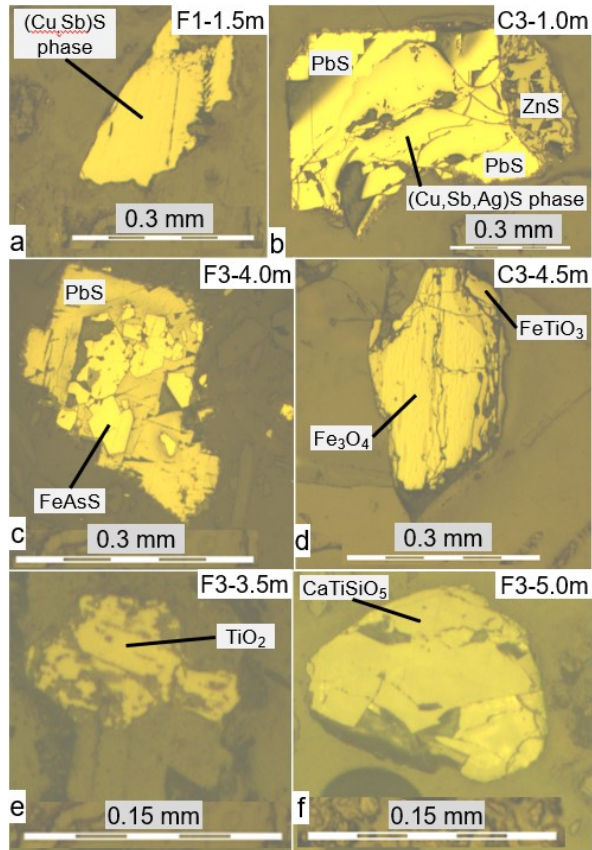


Figure 2.7: Trace ore minerals under reflected light (F: < 0.5 mm, C: 0.5 to 2.0 mm grain size).

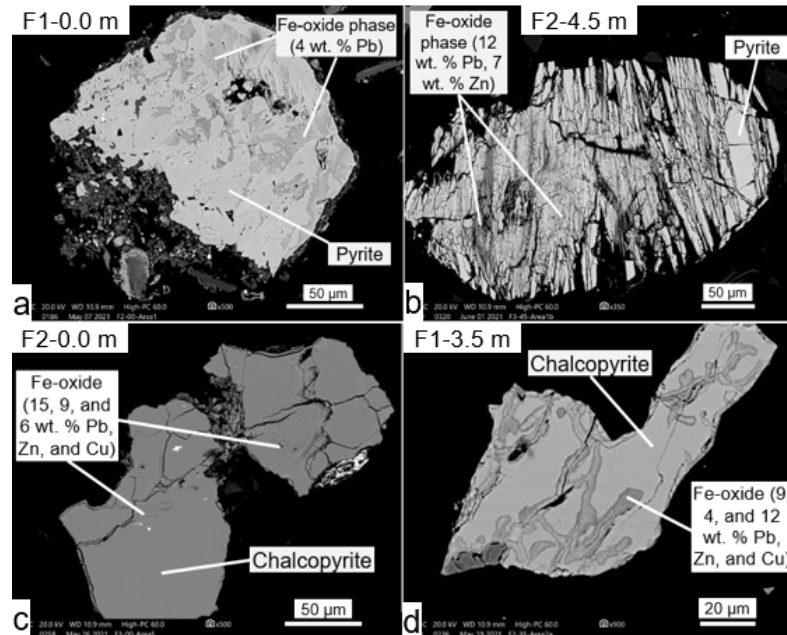


Figure 2.8: BSE images of pyrite (a and b) and chalcopyrite (c and d) weathering phases under SEM (< 0.5 mm grain size).

Unaltered sphalerite mineral cores were primarily composed of Zn and S with 7 to 10 wt.% Fe, under range Cd (1 to 2 wt.%), and < 1 wt.% Ni. Sphalerite alteration zones were typically comprised of a ZnCO_3 phase (hereafter referred to as smithsonite) and 15 to 19 wt.% Fe potentially as an accessory Fe-oxide phase with detectable concentrations of Pb and sometimes Cu (< 5.0 wt.%) (Fig. 2.9a and b). There was no detection of Cd in the alteration zones of any sphalerite grains. Pristine galena mineral cores were composed entirely of Pb and S with no presence of other trace metals. Galena alteration zones were mainly composed of a cerussite (PbCO_3) phase with detectable concentrations of Zn and sometimes Cu (< 5.0 wt.%) (Fig. 2.9c and d). Calcite measured Mg concentrations up to 2 wt.%, and although below detection, both calcite and dolomite occasionally hosted trace concentrations of Mn (< 1 wt.%). Calcite and dolomite were observed both as loose grains and within sulfide minerals such as pyrite (Fig. 2.10a and b).

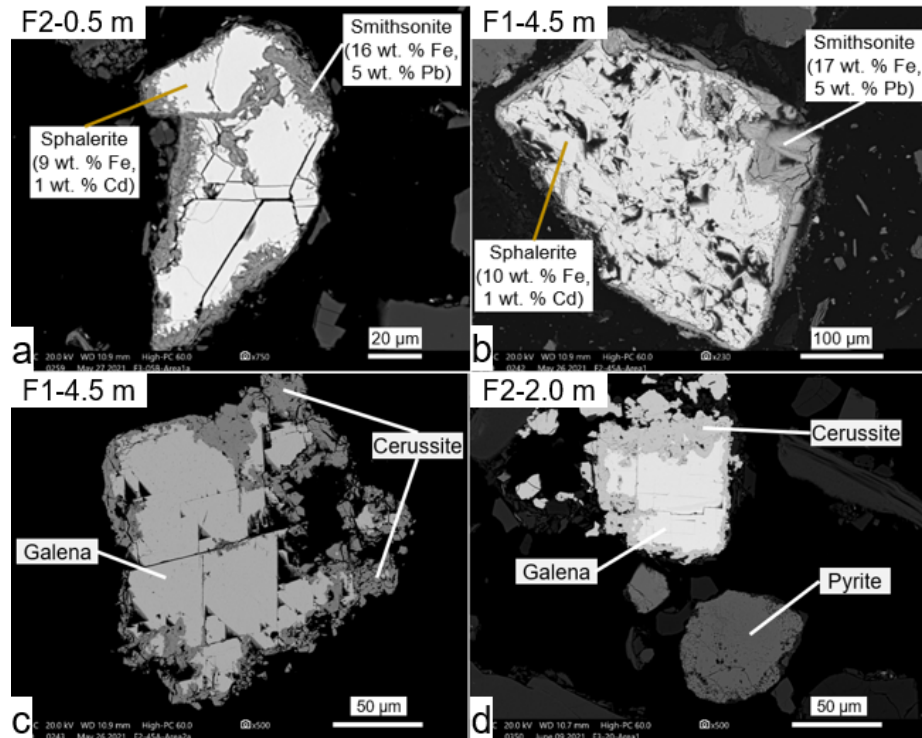


Figure 2.9: BSE images of sphalerite (a and b) and galena (c and d) weathering phases under SEM (< 0.5 mm grain size).

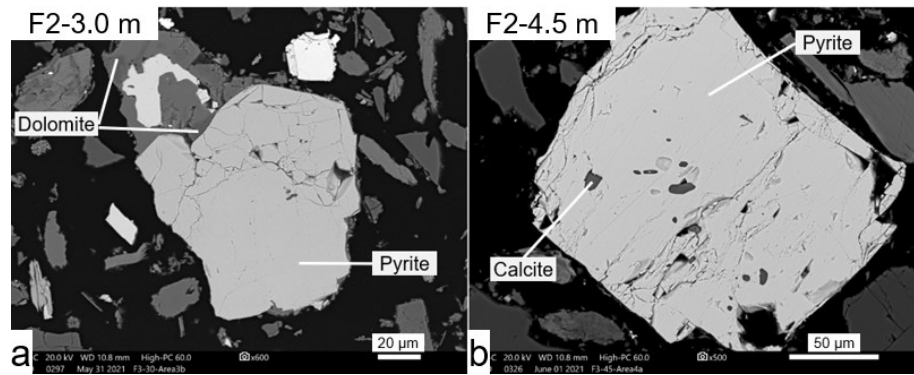


Figure 2.10: BSE images of pyrite and Ca-carbonate phases under SEM (< 0.5 mm grain size).

Although trace concentrations of certain metals (i.e. Co, Ni, Cd, Mg, and Mn) were measured below the detection limit of ~2 wt.%, the presence of these trace metals from the proposed mineral sources remains likely due to metal concentrations confirmed via solid-phase ICP-AES/MS (section 2.4.3).

2.3.3 Total Inorganic Carbon and Sulfur (C/S) Analysis

Sulfur concentrations in the waste-rock material ranged from 0.6 to 4.3 wt.% (coarse-grained $\mu = 2.4$, $\sigma = 1.1$; fine-grained $\mu = 2.3$, $\sigma = 1.1$) in trench 1, from 1.1 to 4.1 wt.% (coarse-grained $\mu = 2.0$, $\sigma = 0.8$; fine-grained $\mu = 2.0$, $\sigma = 0.6$) in trench 2, and from 0.3 to 4.0 wt.% (coarse-grained $\mu = 1.8$, $\sigma = 1.0$; fine-grained $\mu = 1.6$, $\sigma = 0.9$) in trench 3. Inorganic carbon measurements ranged from 0.2 to 2.2 wt.% (coarse-grained $\mu = 1.3$, $\sigma = 0.6$; fine-grained $\mu = 1.4$, $\sigma = 0.6$) in trench 1, from 0.9 to 1.5 wt.% (coarse-grained $\mu = 1.3$, $\sigma = 0.1$; fine-grained $\mu = 1.3$, $\sigma = 0.1$) in trench 2, and from 0.8 to 2.2 wt.% (coarse-grained $\mu = 1.5$, $\sigma = 0.3$; fine-grained $\mu = 1.5$, $\sigma = 0.4$) in trench 3. Error bars were generated based on the standard deviation (σ) of three consecutive sample measurements (Fig. 2.11a - c). The variation in S and C measurements corresponded to different depth locations in each trench and showed no indications of depth dependency. However, the range in total S and C content between trenches was similar and total inorganic carbon concentrations showed an inverse relationship to the total sulfur content across all depths within each trench. Furthermore, the average S content was statistically higher in the coarse-grained fraction than the fine-grained fraction in trench 3 by a mean difference of 0.3 wt.% ($\alpha = 0.003$).

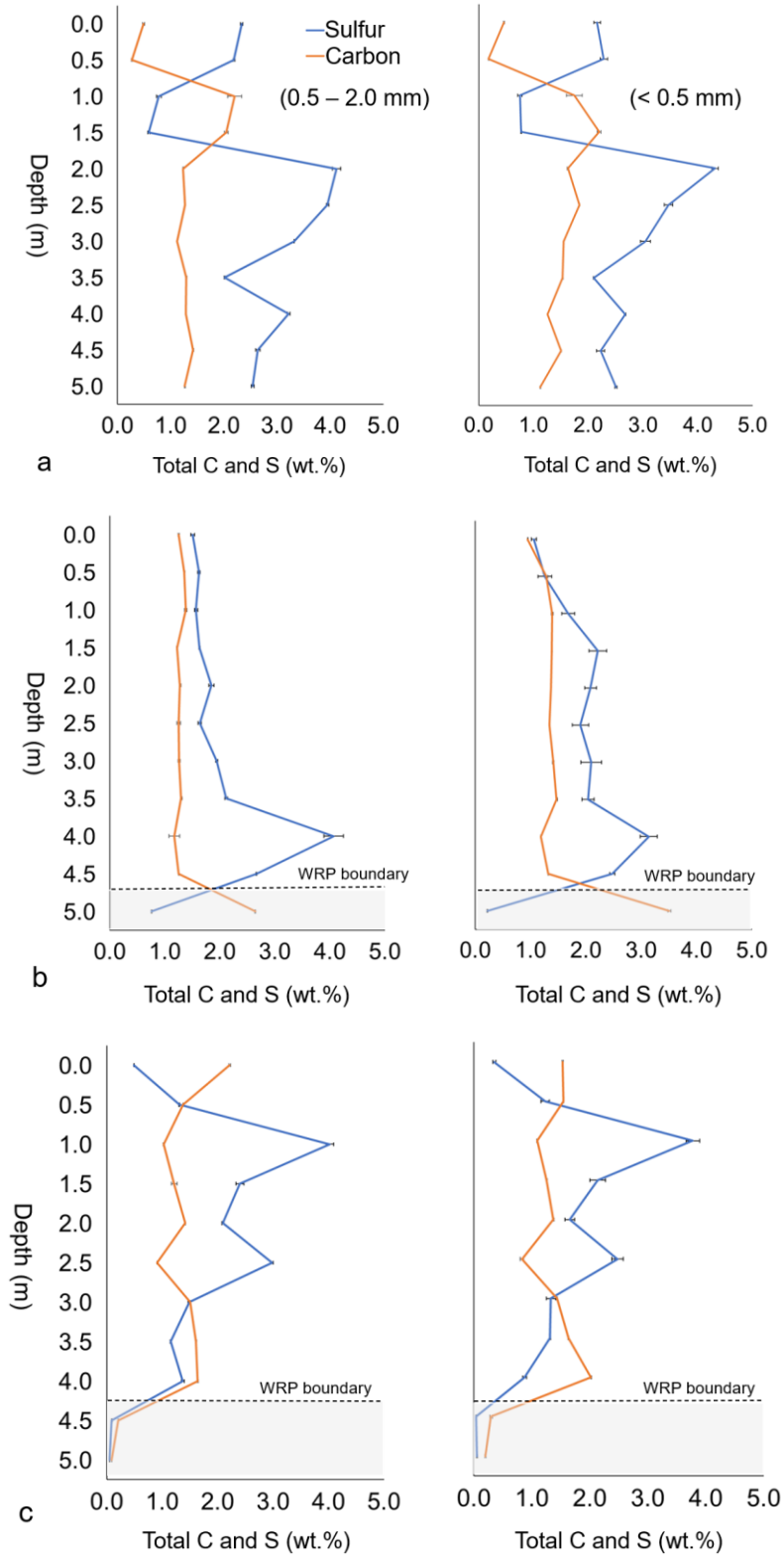
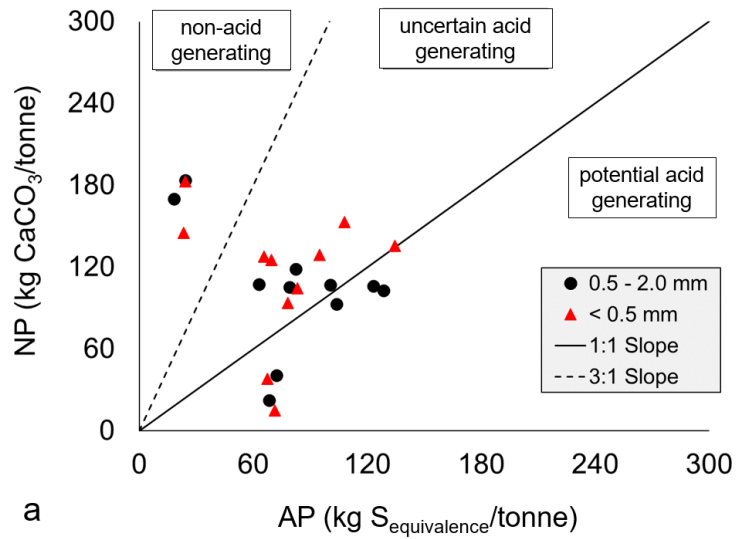
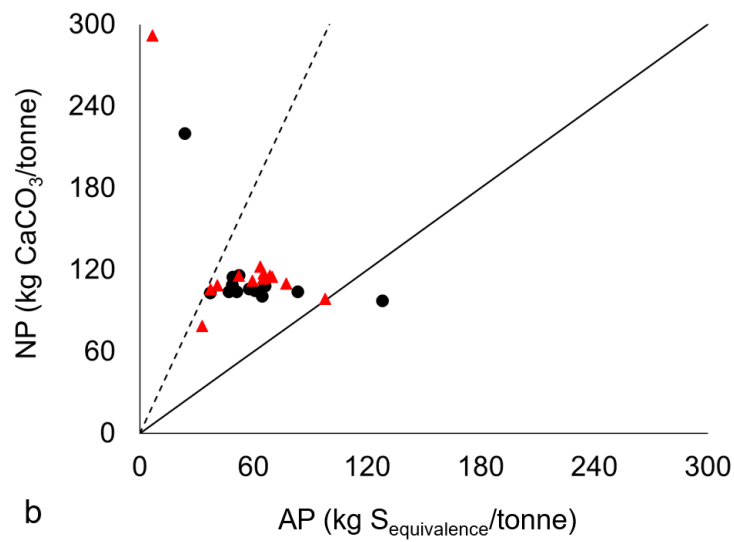


Figure 2.11: Total C and S content (wt.%) for coarse (left) and fine (right) grain fractions for a) trench 1, b) trench 2, c) trench 3. Error bars show the standard deviation from three consecutive measurements

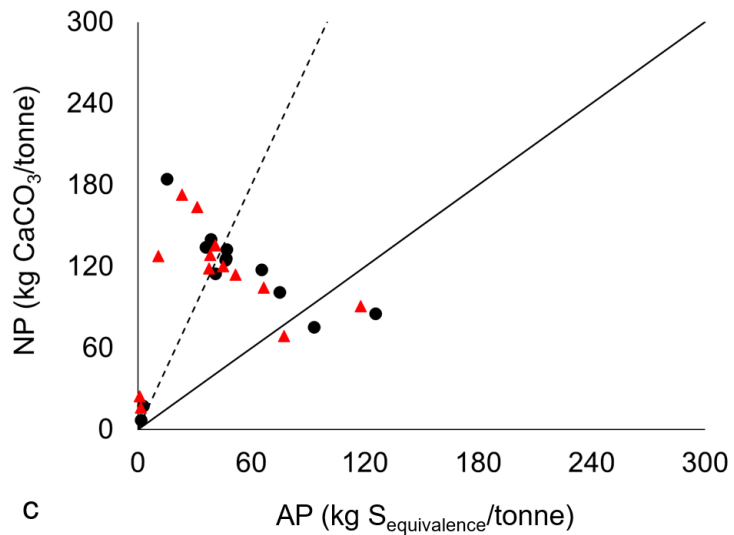
NP:AP ratios (NPR values) for coarse- and fine-grained waste-rock samples ranged from 0.21 to 9.29 (coarse-grained $\mu = 2.7$, $\sigma = 3.2$; fine-grained $\mu = 2.5$, $\sigma = 2.5$) in trench 1, from 0.76 to 2.83 (coarse-grained $\mu = 1.9$, $\sigma = 0.5$; fine-grained $\mu = 1.9$, $\sigma = 0.5$) in trench 2, and from 0.68 to 12.06 (coarse-grained $\mu = 3.2$, $\sigma = 3.1$; fine-grained $\mu = 3.9$, $\sigma = 3.3$) in trench 3 (Fig. 2.12a - c). Most waste-rock samples, both coarse- and fine-grained, across each trench, had a UAG potential. Trench 2 showed the least variability in NPR values with only the coarse-grained fraction of one sample falling into the PAG region; the remainder observed to be uncertain. Trench 1 and trench 3 showed greater variability with multiple samples of both grain size fractions in the PAG and NAG regions.



a



b



c

Figure 2.12: Acid generation potential for a) trench 1, b) trench 2, c) trench 3.

2.3.4 Solid Phase Chemistry

Iron (Fe) concentrations in the waste-rock material ranged from 65126 to 117275 ppm (coarse-grained $\mu = 74107$, $\sigma = 5466$; fine-grained $\mu = 80030$, $\sigma = 16113$) in trench 1, from 64693 to 91735 ppm (coarse-grained $\mu = 72077$, $\sigma = 7109$; fine-grained $\mu = 77206$, $\sigma = 6339$) in trench 2, and from 61406 to 93794 ppm (coarse-grained $\mu = 70600$, $\sigma = 7117$; fine-grained $\mu = 77499$, $\sigma = 7230$) in trench 3 (Fig. 2.13a - c). Iron concentrations in the fine-grained fraction were statistically higher than the coarse-grained fraction in trenches 2 and 3 with mean differences of 5129 and 6899 ppm ($\alpha = 6 \times 10^{-4}$ and 4×10^{-4}).

Copper (Cu) concentrations ranged from 376 to 4098 ppm (coarse-grained $\mu = 1657$, $\sigma = 752$; fine-grained $\mu = 2536$, $\sigma = 1206$) in trench 1, from 1224 to 7544 ppm (coarse-grained $\mu = 2047$, $\sigma = 1220$; fine-grained $\mu = 3286$, $\sigma = 1544$) in trench 2, and from 348 to 3853 ppm (coarse-grained $\mu = 1146$, $\sigma = 714$; fine-grained $\mu = 1781$, $\sigma = 991$) in trench 3 (Fig. 2.13d - f). Copper concentrations in the fine-grained fraction were statistically higher than the coarse-grained fraction in trenches 1, 2, and 3 with mean differences of 878, 1240, and 635 ppm ($\alpha = 5 \times 10^{-5}$, 4×10^{-7} , and 2×10^{-4} , respectively).

Zinc (Zn) concentrations ranged from 6416 to 25709 ppm (coarse-grained $\mu = 10357$, $\sigma = 3538$; fine-grained $\mu = 15223$, $\sigma = 5227$) in trench 1, from 14138 to 28567 ppm (coarse-grained $\mu = 16673$, $\sigma = 2493$; fine-grained $\mu = 23198$, $\sigma = 3978$) in trench 2, and from 4007 to 38899 ppm (coarse-grained $\mu = 11270$, $\sigma = 6026$; fine-grained $\mu = 17252$, $\sigma = 9164$) in trench 3 (Fig. 2.13g - i). Zinc concentrations in the fine-grained fraction were statistically higher than the coarse-grained fraction in trenches 1, 2, and 3 with mean differences of 4867, 6525, and 5982 ppm ($\alpha = 8 \times 10^{-6}$, 1×10^{-6} , and 2×10^{-4} , respectively). Furthermore, Zn concentrations in the coarse-grained fraction were observed to be highest in trench 2 and statistically lower in trench 1 by a mean difference of 6111 ppm ($\alpha = 2 \times 10^{-4}$). The same trend was observed in the fine-grained fraction with a mean difference of 7590 ppm ($\alpha = 2 \times 10^{-3}$).

Lead (Pb) concentrations ranged from 3781 to 30373 ppm (coarse-grained $\mu = 10624$, $\sigma = 5071$; fine-grained $\mu = 15926$, $\sigma = 7510$) in trench 1, from 8122 to 20971 ppm (coarse-grained $\mu = 12243$, $\sigma = 2270$; fine-grained $\mu = 16042$, $\sigma = 3184$) in trench 2, and from 4478 to 45582 ppm (coarse-grained $\mu = 12244$, $\sigma = 6916$; fine-grained $\mu = 15551$, $\sigma = 11201$) in trench 3 (Fig.2.13j - l). Lead concentrations in the fine-grained fraction were statistically higher than the coarse-grained fraction in trenches 1 and 2 with mean differences of 5302 and 3799 ppm ($\alpha = 9 \times 10^{-4}$ and 5×10^{-5}).

Manganese (Mn) concentrations ranged from 504 to 1674 ppm (coarse-grained $\mu = 1099$, $\sigma = 288$; fine-grained $\mu = 1305$, $\sigma = 255$) in trench 1, from 1049 to 1677 ppm (coarse-grained $\mu = 1210$, $\sigma = 99$; fine-grained $\mu = 1234$, $\sigma = 155$) in trench 2, and from 972 to 1790 ppm (coarse-grained $\mu = 1241$, $\sigma = 181$; fine-grained $\mu = 1379$, $\sigma = 253$) in trench 3 (Fig. 2.14a - c). Manganese concentrations in the fine-grained fraction were statistically higher than the coarse-grained fraction in trenches 1 and 3 with mean differences of 205 and 138 ppm ($\alpha = 3 \times 10^{-4}$ and 6×10^{-3}).

Cadmium (Cd) concentrations ranged from 35 to 229 ppm (coarse-grained $\mu = 107$, $\sigma = 35$; fine-grained $\mu = 134$, $\sigma = 50$) in trench 1, from 127 to 284 ppm (coarse-grained $\mu = 173$, $\sigma = 25$; fine-grained $\mu = 210$, $\sigma = 49$) in trench 2, and from 46 to 340 ppm (coarse-grained $\mu = 115$, $\sigma = 56$; fine-grained $\mu = 149$, $\sigma = 77$) in trench 3 (Fig. 2.14d - f). Cadmium concentrations in the fine-grained fraction were statistically higher than the coarse-grained fraction in trenches 1, 2, and 3 with mean differences of 27, 37, and 34 ppm ($\alpha = 1 \times 10^{-3}$, 8×10^{-3} , and 9×10^{-4} , respectively). Furthermore, Cd concentrations in the coarse-grained fraction were observed to be lowest in trench 1 and statistically higher in trench 2 by a mean difference of 65 ppm ($\alpha = 5 \times 10^{-4}$). The same trend was observed in the fine-grained fraction with a mean difference of 74 ppm ($\alpha = 1 \times 10^{-3}$).

Arsenic (As) concentrations ranged from 86 to 1106 ppm (coarse-grained $\mu = 178$, $\sigma = 123$; fine-grained $\mu = 463$, $\sigma = 282$) in trench 1, from 119 to 1607 ppm (coarse-grained $\mu = 396$, $\sigma = 137$; fine-grained $\mu = 1160$, $\sigma = 316$) in trench 2, and from

106 to 1078 ppm (coarse-grained $\mu = 205$, $\sigma = 88$; fine-grained $\mu = 550$, $\sigma = 293$) in trench 3 (Fig. 2.14g - i). Arsenic concentrations in the fine-grained fraction were statistically higher than the coarse-grained fraction in trenches 1, 2, and 3 with mean differences of 313, 764, and 345 ppm ($\alpha = 1 \times 10^{-4}$, 6×10^{-7} , and 8×10^{-4} , respectively). Furthermore, As concentrations in the coarse-grained fraction were observed to be lowest in trench 1 and statistically higher in trench 2 by a mean difference of 214 ppm ($\alpha = 0.01$). The same trend was observed in the fine-grained fraction with a mean difference of 657 ppm ($\alpha = 7 \times 10^{-4}$).

Antimony (Sb) concentrations ranged from 155 to 1313 ppm (coarse-grained $\mu = 301$, $\sigma = 122$; fine-grained $\mu = 610$, $\sigma = 344$) in trench 1, from 312 to 1560 ppm (coarse-grained $\mu = 560$, $\sigma = 176$; fine-grained $\mu = 1050$, $\sigma = 280$) in trench 2, and from 43 to 1318 ppm (coarse-grained $\mu = 279$, $\sigma = 239$; fine-grained $\mu = 532$, $\sigma = 412$) in trench 3 (Fig. 2.14j - l). Antimony concentrations in the fine-grained fraction were statistically higher than the coarse-grained fraction in trenches 1, 2, and 3 with mean differences of 308, 490, and 252 ppm ($\alpha = 4 \times 10^{-4}$, 1×10^{-7} , and 8×10^{-3} , respectively). Furthermore, Sb concentrations in the coarse-grained fraction were highest in trench 2 and statistically lower in trenches 1 and 3 by mean differences of 287 and 284 ppm ($\alpha = 5 \times 10^{-3}$ and 0.04). The same trend was observed in the fine-grained fraction with mean differences of 477 and 460 ppm ($\alpha = 0.02$ and 0.03).

Titanium (Ti) concentrations ranged from 2013 to 4274 ppm (coarse-grained $\mu = 3153$, $\sigma = 744$; fine-grained $\mu = 3376$, $\sigma = 589$) in trench 1, from 3606 to 4312 ppm (coarse-grained $\mu = 3784$, $\sigma = 244$; fine-grained $\mu = 4052$, $\sigma = 178$) in trench 2, and from 3064 to 4418 ppm (coarse-grained $\mu = 3497$, $\sigma = 365$; fine-grained $\mu = 3825$, $\sigma = 368$) in trench 3 (Fig. 2.15a - c). Titanium concentrations in the fine-grained fraction were statistically higher than the coarse-grained fraction in trenches 1, 2, and 3 with mean differences of 223, 268, and 328 ppm ($\alpha = 0.03$, 1×10^{-3} , and 7×10^{-3} , respectively). Furthermore, Ti concentrations in the coarse-grained fraction were lowest in trench 1 and statistically higher in trench 2 by a

mean difference of 757 ppm ($\alpha = 0.04$). The same trend was observed for the fine-grained fraction with a mean difference of 753 ppm ($\alpha = 0.01$).

Chromium (Cr) concentrations ranged from 152 to 294 ppm (coarse-grained $\mu = 217$, $\sigma = 42$; fine-grained $\mu = 176$, $\sigma = 15$) in trench 1, from 145 to 249 ppm (coarse-grained $\mu = 208$, $\sigma = 18$; fine-grained $\mu = 166$, $\sigma = 14$) in trench 2, and from 158 to 264 ppm (coarse-grained $\mu = 225$, $\sigma = 26$; fine-grained $\mu = 179$, $\sigma = 15$) in trench 3 (Fig. 2.15d - f). Chromium concentrations in the coarse-grained fraction were statistically higher than the fine-grained fraction in trenches 1, 2, and 3 with mean differences of 42, 43, and 46 ppm ($\alpha = 3 \times 10^{-4}$, 2×10^{-6} , and 7×10^{-6} , respectively). Furthermore, Cr concentrations in the fine-grained fraction were highest in trench 1 and statistically lower in trench 2 with a mean difference of 13 ppm ($\alpha = 6 \times 10^{-3}$).

Cobalt (Co) concentrations ranged from 17 to 45 ppm (coarse-grained $\mu = 23$, $\sigma = 4$; fine-grained $\mu = 35$, $\sigma = 6$) in trench 1, from 20 to 44 ppm (coarse-grained $\mu = 22$, $\sigma = 1$; fine-grained $\mu = 34$, $\sigma = 3$) in trench 2, and from 18 to 46 ppm (coarse-grained $\mu = 23$, $\sigma = 3$; fine-grained $\mu = 35$, $\sigma = 6$) in trench 3 (Fig. 2.15g - i). Cobalt concentrations in the fine-grained fraction were statistically higher than the coarse-grained fraction in trenches 1, 2, and 3 each with a mean difference of 12 ppm ($\alpha = 2 \times 10^{-6}$, 1×10^{-7} , and 5×10^{-5} , respectively).

Nickel (Ni) concentrations ranged from 23 to 81 ppm (coarse-grained $\mu = 44$, $\sigma = 10$; fine-grained $\mu = 58$, $\sigma = 12$) in trench 1, from 34 to 96 ppm (coarse-grained $\mu = 48$, $\sigma = 13$; fine-grained $\mu = 66$, $\sigma = 12$) in trench 2, and from 40 to 73 ppm (coarse-grained $\mu = 47$, $\sigma = 6$; fine-grained $\mu = 62$, $\sigma = 7$) in trench 3 (Fig. 2.15j - l). Nickel concentrations in the fine-grained fraction were statistically higher than the coarse-grained fraction in trenches 1, 2, and 3 by 14, 18, and 15 ppm ($\alpha = 1 \times 10^{-6}$, 2×10^{-7} , and 1×10^{-5} , respectively). Furthermore, Ni concentrations in the fine-grained fraction were highest in trench 2 and statistically lower in trench 1 by a mean difference of 9 ppm ($\alpha = 0.02$).

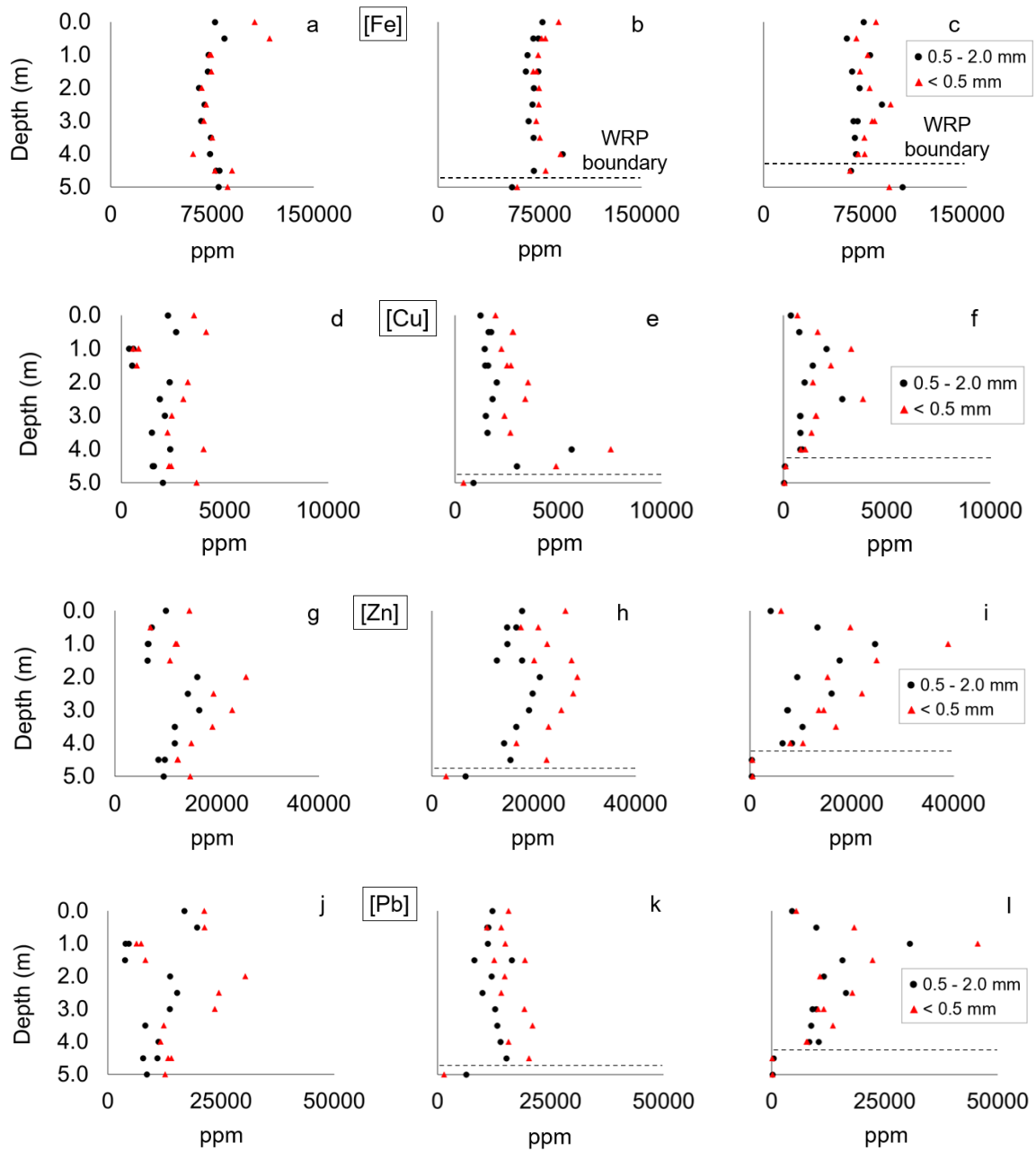


Figure 2.13: Solid-phase iron (Fe), copper (Cu), zinc (Zn), and lead (Pb) depth plots for trench 1 (left), trench 2 (middle), and trench 3 (right).

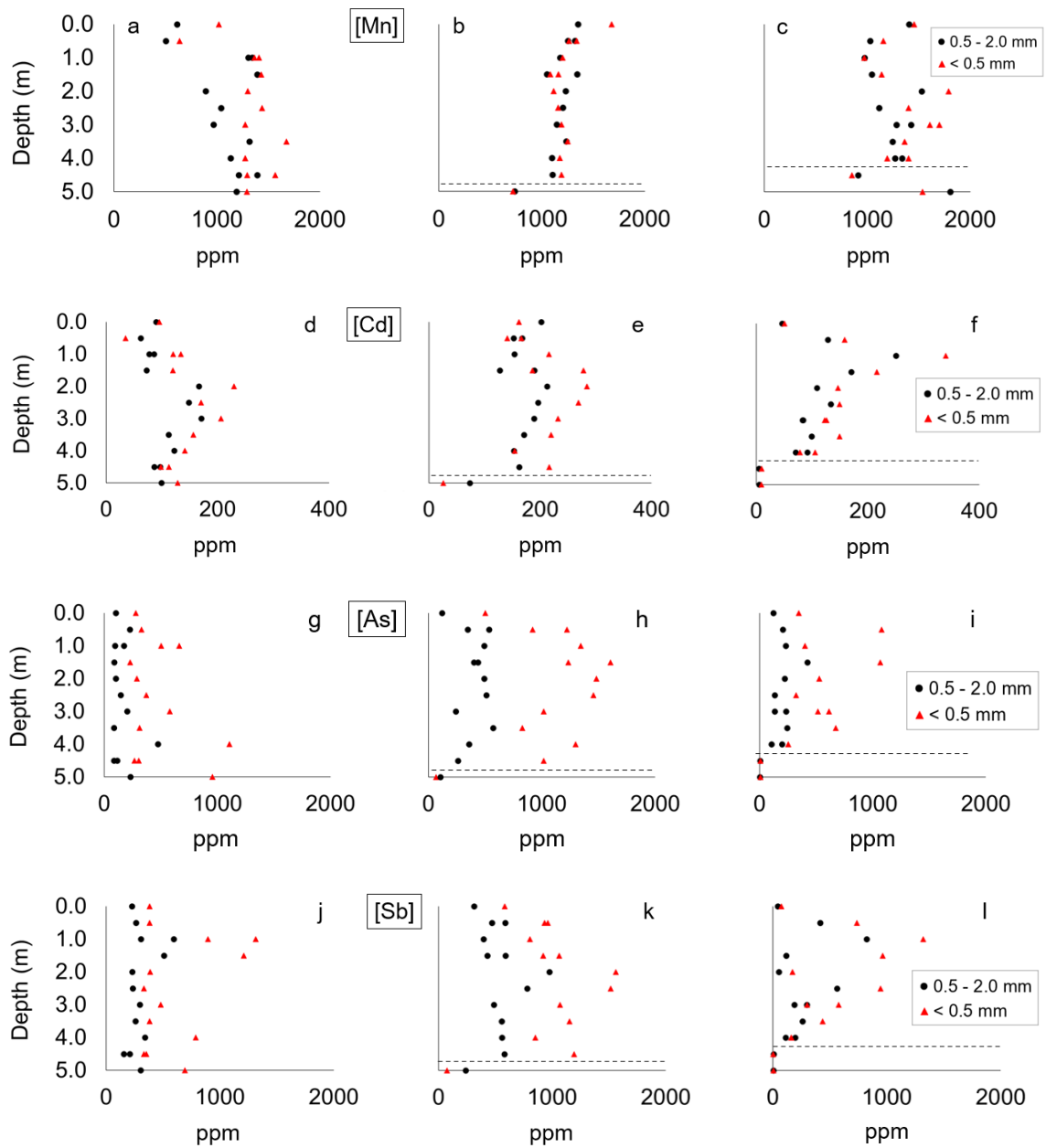


Figure 2.14: Solid-phase manganese (Mn), cadmium (Cd), arsenic (As), and antimony (Sb) depth plots for trench 1 (left), trench 2 (middle), and trench 3 (right).

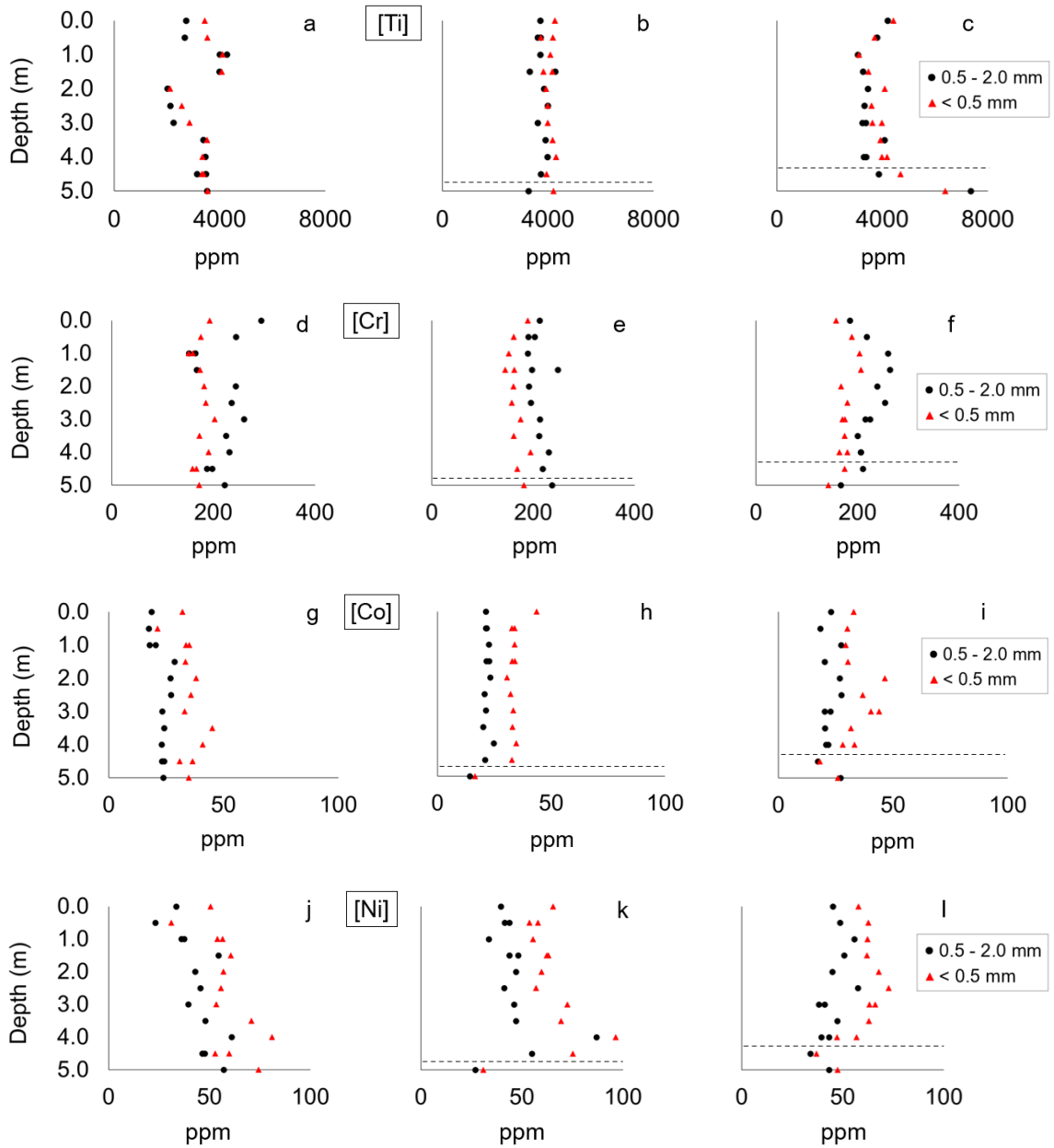


Figure 2.15: Solid-phase titanium (Ti), chromium (Cr), cobalt (Co), and nickel (Ni) depth plots for trench 1 (left), trench 2 (middle), and trench 3 (right).

In summary, there was no statistically significant relationship between concentration and depth in any trench for either grain fraction of the reported metals identified by ICP-AES/MS. Chromium was the only metal that measured higher concentrations in the coarse-grained fraction than the fine-grained fraction of waste-rock material. In order of appearance, the fine-grained fraction measured

higher relative concentrations of Cu (57% increase), Zn (45%), Pb (36%), Cd (25%), As (186%), Sb (92%), Co (53%), and Ni (34%) than the coarse-grained fraction. In trench 1, Zn, Cd, As, Sb, Ti, and Ni in fine and/or coarse-grained fractions measured statistically higher average concentrations than trench 2. Furthermore, concentrations of Zn, Pb, and Cd showed very similar depth patterns spiking at 1.0 m depth in trench 3 and deficient at 1.0 m depth in trench 1.

2.4 Discussion

2.4.1 General Lithology and Mineralogy

The primary waste-rock mineral phases at Ore Chimney included quartz, oligoclase, hornblende, and biotite and accounted for 80 to 90 wt.% of the bulk mineralogy. The minor mineral phases identified throughout the waste-rock pile accounted for the remaining 10 to 20 wt.% and included chlorite, calcite, dolomite, and sulfide minerals mainly represented by chalcopyrite, pyrite, sphalerite, and galena. Wheeler (2017) conducted a detailed petrographic study in one 4.0 m deep trench in the waste-rock pile at Ore Chimney and characterized the mineralogy to mainly consist of quartz, biotite, and hornblende with traces of calcite, galena, sphalerite, pyrite, and chalcopyrite. Moore and Thompson (1980) and Harnois and Moore (1989) identified these phases from thin section analyses from fresh in situ samples of the Ore Chimney Formation, Tudor Formation, and neighbouring quartz vein lithologies from bore holes that intersected the underground workings that generated the Ore Chimney waste-rock pile and described in detail the additional presence of plagioclase feldspar, chlorite, and dolomite.

Distribution of major mineral phases (including chlorite) was relatively uniform throughout all three vertical transects and showed only minor changes with depth. However, variation in mineral abundance with depth was different in each vertical transect and showcases the heterogeneity of blasted waste-rock material and non-uniform pile formation from underground development at Ore Chimney. The waste-rock material at Ore Chimney was stockpiled as six elongated “fingers” that overlapped and extended away from the direction of the mineshaft (Kingston,

1980; Archibald, 2012). The fingers represent stretches of geological material that were blasted and stockpiled during different stages of underground development. Vertical trenches 1, 2, and 3 were dug at fingers 3, 4, and 5, respectively, and Wheeler (2017) sampled to 4.0 m depth in a trench corresponding to finger 2 (Fig. 2.16). Two of the six elongated sections of stockpiled material (1 and 6) were masked by vegetation, yielding four distinct piling stages from aerial photography (Fig. 1.1).

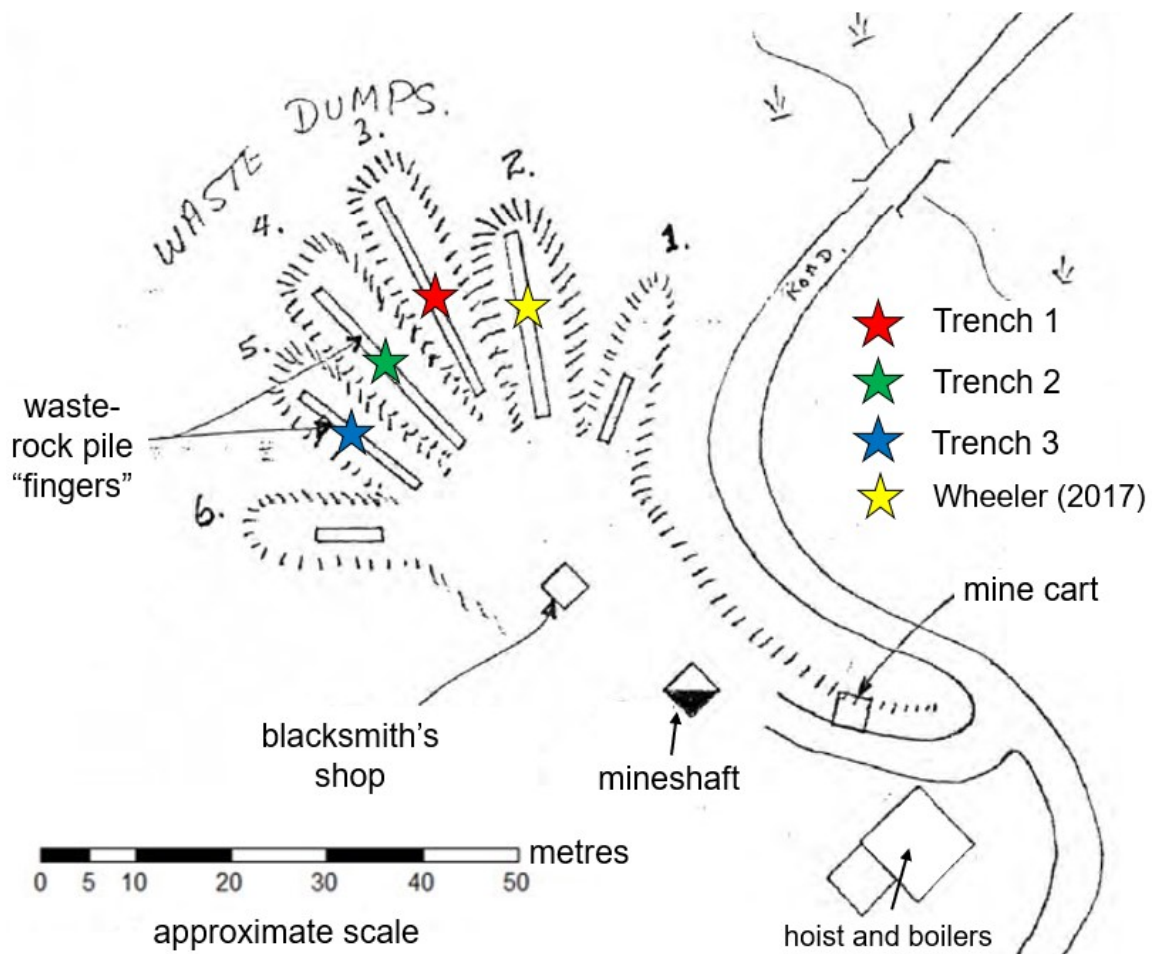


Figure 2.16: Historical sketch of the Ore Chimney waste-rock pile updated with study sampling locations (modified from Kingston, 1980).

The entrance of the vertical mineshaft at the Ore Chimney property was confined within the Tudor Formation and underground workings extended laterally at various levels targeting carbonate-rich quartz veins surrounding the Ore Chimney

Formation (Dillon, 1985; Harnois and Moore, 1989). The variation in waste-rock mineral abundance with depth along each vertical transect was not considerable enough to distinguish the different lithologies encountered during underground development. Therefore, the waste-rock pile on the property was most likely comprised of blasted rock fragments originating from the Tudor Formation, Ore Chimney Formation, and intrusive quartz veins. There are no records indicating a systematic formation of the waste-rock pile (Archibald, 2012); however, it is most likely that the waste-rock “fingers” developed in succession and represent slightly different distributions of the Tudor Formation, Ore Chimney Formation, and quartz veins, which was directly reflected in the similar bulk mineralogy and minor variation in mineral abundance from PXRD and total C/S measurements.

Quartz was observed as the dominant mineral phase in the waste-rock material, ranging from 40 to 60 wt.%. It is highly unlikely for the quartz content to originate from quartzite and/or siliceous metaconglomerate (Flinton group) since these geological units were spatially located away from underground workings and were observed to contain minimal sulfur (< 0.01 wt.%) and carbonate (0.2 wt.%) content (Harnois and Moore, 1988). The metamorphosed tholeiitic basalt comprising the Tudor Formation is mainly composed of hornblende and plagioclase feldspar but may contribute minor proportions (5 to 15 wt.%) of the quartz concentrations measured in the waste-rock material (Harnois and Moore, 1988). Measurements of oligoclase (10 to 30 wt.%) dispersed throughout the waste-rock samples can be explained by the presence of the Tudor Formation and elevated quartz measurements therefore must have been contributed by another type of lithology, likely quartz veins.

Concentrations of biotite are mainly hosted within biotite schist and provide the strongest evidence that blasted material from the Ore Chimney Formation was mixed throughout the waste-rock pile. Measurable concentrations (> 5 wt.%) were ubiquitous throughout the pile suggesting that the Ore Chimney Formation was actively targeted throughout most of the mining operations. Furthermore, apatite and titanite were trace mineral phases most commonly associated with the Ore

Chimney Formation and were identified in some instances under SEM-EDX; thus, providing additional evidence that the Ore Chimney Formation constitutes an appreciable portion of the waste-rock material (Harnois and Moore, 1988).

Hornblende has been identified as a mineral component of the Tudor Formation; however, it has also been observed to persist in the Ore Chimney Formation near the contact between the two units (Moore and Thompson, 1980). Investigations of the Ore Chimney Formation from detailed geological mapping surveys identified a variation in mineral assemblage including garnet-biotite, muscovite-biotite, and hornblende-biotite schist. The Ore Chimney Formation that was targeted underground mainly consisted of biotite schist or hornblende-biotite schist due to the absence of garnet and muscovite mineral phases in the waste rock (Harnois and Moore, 1988). Therefore, it is likely that the hornblende concentrations were contributed by both the Tudor Formation and the Ore Chimney Formation. Likewise, the Tudor Formation and the Ore Chimney Formation have both been observed to host chlorite, which may also be contributed by both formations (Harnois and Moore, 1988).

Although sometimes measured below detection, average concentrations of calcite (2.2 wt.%) and dolomite (4.1 wt.%) throughout the waste-rock pile from both grain fractions estimated by PXRD was confirmed with optical microscopy and subsequent SEM-EDX. Harnois and Moore (1988) observed carbonate minerals in the Tudor Formation at Ore Chimney; however, they were typically associated as small veinlets less than 2 cm in diameter and are mainly composed of calcite. Calcite has been observed in metasedimentary rocks and some sections of biotite schist that are located on the property; although, these localities do not intersect with the underground workings that created the waste-rock pile (Moore and Thompson, 1980; Harnois and Moore, 1988). Furthermore, dolomite was measured as a dominant carbonate phase throughout the waste-rock pile but was not observed in the Tudor, Ore Chimney, or Bishop Corners Formation (Moore and Thompson, 1980). The presence of calcite and dolomite in relatively high abundance most likely originated from the blasting of carbonate-rich quartz veins

located throughout a shear zone directly intersecting the underground workings (Archibald, 2012).

The relatively high detection limit of 2 wt.% for PXRD analyses made it difficult to compare certain mineral quantities with sufficient confidence. However, in coarse-grained samples, dolomite may be more abundant than calcite by 2.5 and 4.8 wt.% in trenches 2 and 3, respectively. Fine-grained samples in trenches 2 and 3 may also contain more dolomite than calcite by 1.5 and 2.7 wt.%, respectively. Harnois and Moore (1989) observed calcite and dolomite as the two carbonate phases hosted by the quartz vein system that was targeted at Ore Chimney and estimated that calcite and dolomite were each concentrated in the quartz veins by an average of 5 % (by volume) but ranged as high as 20 %. In addition, Harnois and Moore (1989) observed a higher proportion of calcite than dolomite, which is contrary to measurements of the waste-rock material herein that suggest higher average concentrations of dolomite. Compared to dolomite, calcite has a higher solubility (Langmuir, 1997) and has been observed to buffer low pH waters at a rate approximately one order of magnitude higher, which explains the potential depletion of calcite in the waste-rock material (Lapakko, 2002). However, measurable calcite is still present in the waste rock and has not been completely exhausted even after ~100 years of sulfide mineral weathering. The quartz vein system is likely the main contributor for the concentrations of calcite and dolomite observed throughout the pile. Likewise, the quartz vein system is the only geological body that hosted the assemblage of sulfide minerals most comparable to concentrations observed in the pile and therefore must be a significant component of the waste-rock bulk mineralogy (Archibald, 2012).

The grain size of waste-rock material varied considerably throughout the pile from < 0.5 mm particles to 20 cm diameter rock fragments. Material blasting and weathering processes may fractionate different minerals into different grain size categories depending on mineral hardness and reactivity at the surface. For example, quartz is a robust mineral with a low chemical reactivity and therefore remains relatively inert (Nesbitt et al., 1997), which explains why higher

concentrations of quartz were observed in the coarse-grained fraction than the fine-grained fraction in all three trenches. Conversely, biotite has a lower mineral hardness and is more reactive than quartz due to the oxidation of ferrous iron and inherently weaker mineral structure (Fordham, 1990), which corroborates PXRD results of higher concentrations of biotite measured in the fine-grained fraction of sampled waste-rock material.

2.4.2 Mineral-Derived Metals in the Waste Rock

Mineralogical data from PXRD indicated that solid-phase Fe concentrations in the waste rock originated from hornblende, biotite, chlorite, pyrite, and ferroan sphalerite minerals. Furthermore, ICP-AES measured higher Fe concentrations in the fine-grained fraction of waste-rock material compared to the coarse-grained fraction in trenches 2 and 3. Hornblende accounts for 5 to 15 wt.% of the bulk mineralogy; however, PXRD results did not show a difference in hornblende concentration with grain size. Biotite was slightly enriched in the fine-grained fraction of the waste rock and accounted for 10 to 25 wt.% of the bulk mineralogy, which is the highest of the Fe-bearing mineral phases. Wilson (1970) studied the weathering of a soil profile developed from a biotite-hornblende parent rock and observed enrichment of biotite-derived clay minerals in the upper soil profile where hornblende was less weathered and concentrated in closer proximity to the parent material. Therefore, elevated Fe measurements observed in the fine-grained fraction of the waste rock compared to the coarse-grained fraction in trenches 2 and 3 suggest that biotite weathers more easily than hornblende and is likely the primary source of Fe in the waste-rock material (Wilson, 1970; Wilson and Farmer, 1970).

Although often measured below the detection limit, PXRD analysis identified the presence of galena and Fe-bearing sphalerite, which are likely the main sources of Pb and Zn in the waste rock. Low ICP-AES/MS Zn and Pb concentrations observed at 1.0 and 1.5 m depth in trench 1 correlate with low total S measurements in addition to a decreased presence of sulfide minerals in the PXRD data. Likewise, elevated Zn and Pb measurements at 1.0 m depth in trench

3 correlate with elevated total S concentration and increased concentrations of sulfides. Decreased Cu signatures at 1.0 and 1.5 m depth in trench 1 also correlate with a low sulfide mineral concentration; however, Cu concentrations rarely exceeded 5000 ppm (0.5 wt.%) and were too dilute to detect a Cu-bearing sulfide phase from PXRD. Using reflected light microscopy, galena and sphalerite grains and lower levels of chalcopyrite and pyrite were identified in every fine- and coarse-grained waste-rock sample, which is consistent with the sulfide mineral assemblage identified from underground workings at Ore Chimney from past studies (Dillon, 1985; Harnois and Moore, 1988, Harnois and Moore, 1989; Archibald, 2012). Solid-phase ICP-AES/MS analyses of Cu, Zn, and Pb all measured higher relative concentrations in the fine-grained fraction. Compared to quartz, which has a mineral hardness of 7, galena, sphalerite, and chalcopyrite all have relatively lower mineral hardness of 2.5, 3.5 to 4, and 3.5 to 4, respectively (Petrescu, 1999). Therefore, blasting activities and century-long weathering may partition sulfides into smaller grain sizes, which was statistically insignificant with PXRD and total C/S measurements, but apparent in the solid-phase ICP-AES/MS results.

The biotite mineral phase identified from PXRD analysis contained Mn at a mole fraction of 1% (atomic proportion of 0.01; Fig. 2.2j - l). Comparing both grain fractions from all three trenches, the average biotite concentration in the waste-rock pile at Ore Chimney is approximately 16 wt.%. Therefore, the relative mass fraction of Mn in biotite (0.0012 g Mn/g biotite) identified by PXRD yields an average Mn contribution of 0.02 wt.%, which is sixfold lower than the average total Mn concentration of 1200 ppm (0.12 wt.%) in the waste-rock pile determined from ICP-AES. PXRD has a much lower resolution than ICP-AES and the discrepancy between average Mn concentration suggests that Mn was underestimated as a component of biotite and/or additional Mn-bearing minerals are contributing to the signatures measured in the waste rock.

Polished grain mounts of 60 μm were tailored for the preservation and investigation of ore minerals (Langman et al., 2015); thus, Mn content in biotite grains was not

verified using SEM-EDX. Although below the detection limit, SEM-EDX consistently detected Mn in calcite and dolomite grains ($n = 4$ calcite and 1 dolomite) ranging from 0.33 to 0.86 wt.% ($\mu = 0.51$, $\sigma = 0.22$). In addition, Mn concentrations were consistently detected in ilmenite grains under SEM-EDX ($n = 21$) ranging from 0.37 to 4.73 wt.% ($\mu = 1.81$, $\sigma = 1.12$). Llera et al (2019) identified ilmenite with an average Mn concentration of 4.6 wt.% in biotite-muscovite schist that underwent similar shearing and metasomatic processes as the mineralized Ore Chimney Formation (Harnois and Moore, 1988). In addition, the average Mn content of biotite was observed to increase from 0.18 wt.% in non-metasomatized schist samples to 0.28 wt.% in metasomatized samples (Llera et al., 2019) suggesting that biotite, ilmenite, and calcite in the mineralized Ore Chimney Formation may substantially contribute to waste-rock Mn concentrations measured by ICP-AES.

Waste-rock Cd, As, and Sb concentrations measured by ICP-MS were not reflected in the mineralogy identified from PXRD. Low Cd concentrations observed at 1.0 and 1.5 m depth in trench 1 correlate with low total S measurements and a decreased abundance of sulfides in the mineralogical data. Likewise, an elevated Cd measurement at 1.0 m depth in trench 3 correlates with elevated S content and an increased concentration of sulfides. SEM-EDX analysis identified Cd at 1 to 2 wt.% exclusively in sphalerite grains, which is below the detection limit, but consistent with measurements from other studies (Koski et al., 2008; Cook et al., 2009; Ye et al., 2011). Like other sulfide-derived metals (Pb, Zn, and Cu), Cd concentrations measured by ICP-MS were higher in the fine-grained fraction of waste-rock samples. Furthermore, the relationship between Cd concentrations and depth was similarly observed with Zn indicating that sphalerite is likely the principal source of Cd concentrations in the waste rock.

Reflected light microscopy and SEM-EDX analysis on polished grain mounts identified the presence of arsenopyrite, which was the only mineral observed to host measurable quantities of As. In aerobic environments, arsenopyrite has a mineral durability and alteration resistance that is proposed to be lower than pyrite

and chalcopyrite but greater than sphalerite (Moncur et al., 2009). Likewise, As concentrations were higher in the fine-grained fraction of waste-rock samples, which is consistent with measurements of other sulfide-bearing metals and suggests that arsenopyrite is the predominant source for As concentrations in the waste rock. Petrographic investigations also identified the presence of a (Cu,Sb,Ag)-bearing sulfide mineral that has been previously observed (in addition to arsenopyrite) in the mineralized zone of the Ore Chimney Formation and is described as freibergite (Harnois and Moore, 1989). In other settings, galena has been observed to substitute Pb for Sb at concentrations as high as 0.3 wt.% (George et al., 2015; Hamzeh et al., 2020) and contain inclusions with Sb concentrations as high as 4.0 wt.% (Sharp and Buseck, 1993). However, SEM-EDX measurements of galena at Ore Chimney revealed no trace of Sb and it is likely that freibergite is the primary source of Sb (and Ag) concentrations in the waste rock.

PXRD analysis estimated biotite to host Ti at an atomic proportion of 0.1 (mass fraction of 0.01). An average biotite concentration of 16 wt.% contributes a relative Ti proportion of 0.16 wt.%. Solid-phase ICP-AES/MS measurements of Ti in the waste rock averaged a concentration of 3600 ppm (0.36 wt.%), which is twofold higher than Ti estimations in biotite predicted by PXRD. Reflected light microscopy and subsequent SEM-EDX analysis identified one grain of titanite (CaTiSiO_5) at 5.0 m depth in trench 3 (Fig. 2.7f) and the occasional presence of ilmenite (FeTiO_3) and rutile (TiO_2) as additional Ti-bearing mineral phases throughout the waste-rock pile (2.17a - d). Grey and Reid (1975) proposed that rutile may be a natural weathering product of ilmenite through ferrous iron oxidation and subsequent Fe removal by leaching. However, Fe oxidation is expected to form secondary hematite (Fe_2O_3) and goethite [$\text{FeO}(\text{OH})$] along ilmenite grain boundaries (Dawson and Smith, 1977; Schroeder et al., 2002) and the presence of Fe-oxides or Fe-oxyhydroxides were not detected as an alteration phase of ilmenite in the Ore Chimney waste rock (Fig. 18a - d). Fu et al (2010) observed rutile as a stable ilmenite oxidation product under a temperature range of 500 to 800°C, which overlaps with regional metamorphic temperature estimates of 420 to 530°C at Ore

Chimney (Harnois and Moore, 1989). Therefore, it is likely that rutile and ilmenite crystallized within an underground intrusion and subsequent metamorphism under oxidizing conditions, rather than subaerial weathering and are relatively more stable above ground surface than sulfide minerals (Dawson and Smith, 1977).

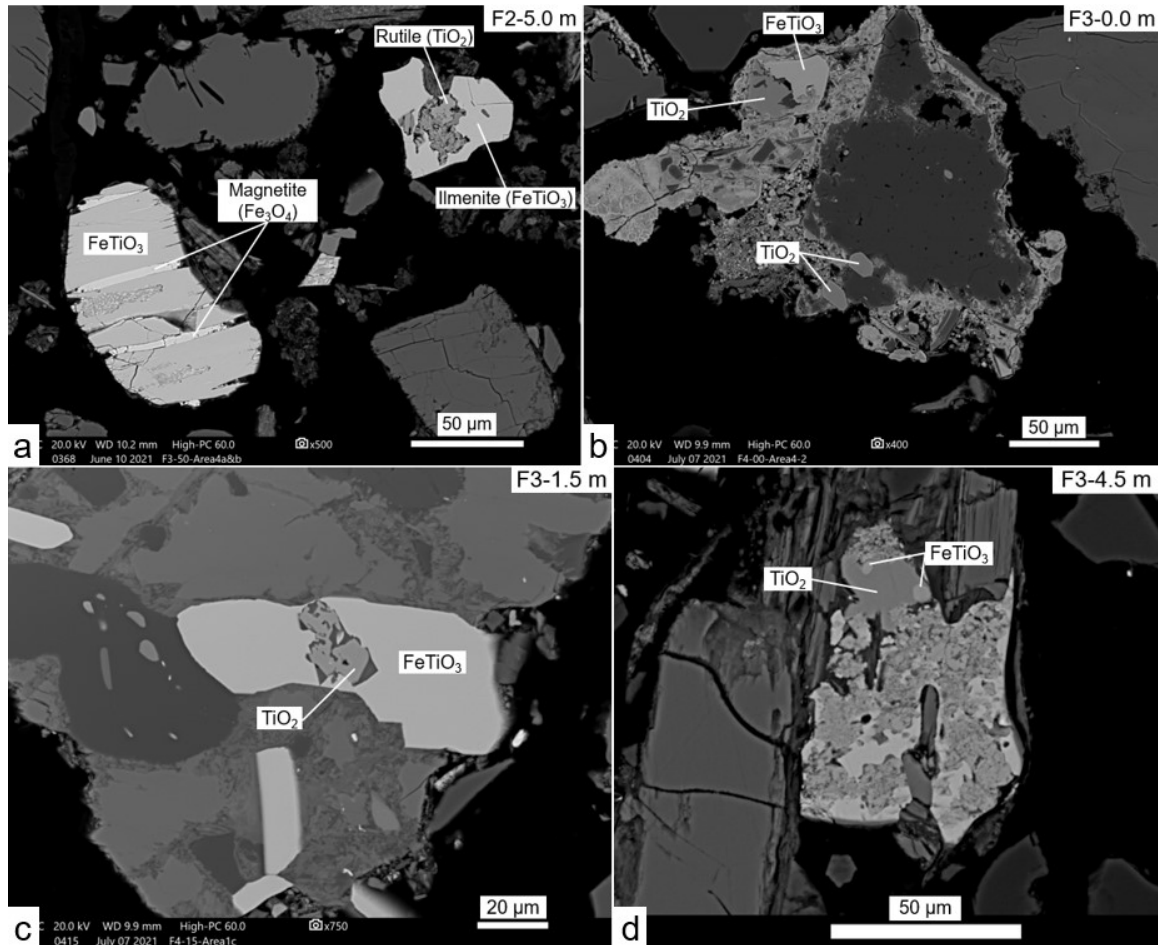


Figure 2.17: BSE images of Fe- and Ti-oxide phases in the Ore Chimney waste rock.

The average solid-phase Cr concentrations in the waste rock at Ore Chimney measured 200 ppm (0.02 wt.%) and were too low to be reflected as a stoichiometric component of mineral phases identified with PXRD. Furthermore, SEM-EDX analysis did not detect Cr as a component of any ore mineral phase except for one instance where Cr was measured (below the detection limit) in magnetite at 0.1 wt.%. In other mine-waste studies, Cr has been observed as a trace component of

chlorite, biotite, amphibole, and pyroxene minerals (Tischendorf et al., 2001; Jambor et al., 2002; Moncur et al., 2009). However, subsequent porewater Cr signatures are typically derived from the weathering of Cr-bearing magnetite in mine wastes (Moncur et al., 2005; Gunsinger et al., 2006b; Moncur et al., 2009). Chromium concentrations in the Ore Chimney waste rock were too low to be attributed to any common rock-forming or trace mineral phases. However, magnetite is a relatively robust mineral (Petrescu, 1999) and higher measurements of Cr in the coarse-grained fraction of waste rock measured by ICP-AES/MS suggests that magnetite may be the primary source of Cr in the waste rock. Solid-phase concentrations of Co and Ni throughout the waste-rock pile were lower than Cr and averaged 54 and 28 ppm (0.005 and 0.003 wt.%, respectively). Although below the SEM-EDX detection limit, spot analyses on polished grain mounts detected trace levels of Co (< 0.6 wt.%) and Ni (< 0.9 wt.%) in several pyrite, magnetite, and ilmenite grains but these metals seldomly existed together. Pyrite was observed to host trace Co and Ni concentrations more frequently than magnetite and ilmenite. In addition, pyrite is more reactive than Fe-oxides in aerobic environments (Moncur et al., 2009) and ICP-AES/MS measured higher concentrations of Co and Ni in the fine-grained fraction of waste-rock material further suggesting that pyrite is the primary source of Co and Ni at Ore Chimney.

2.4.3 Sulfide Mineral Weathering

The primary sulfide mineral assemblage identified in almost every waste-rock sample using reflected light microscopy in order of decreasing relative abundance included sphalerite > galena > pyrite > chalcopyrite. In addition, observations of arsenopyrite and a (Cu,Sb,Ag)S mineral phase (potentially freibergite) were identified as additional sulfide minerals in few samples in trace amounts. Ilmenite represented the most abundant oxide mineral phase that was detected in few samples at trace levels and all the identified ore minerals were previously observed by Harnois and Moore (1989). The average extent of weathering observed in the waste-rock material was variable between the different primary sulfide minerals indicating differences in mineral durability. The comparative weathering rates of

sulfide minerals are summarized by Nordstrom and Alpers (1999) and corroborated by empirical field studies (Blowes and Jambor, 1990; Plumlee, 1999; Moncur et al., 2005; Gunsinger et al., 2006a; Koski et al., 2008; Moncur et al., 2009). Considering only the primary sulfide mineral phases observed at Ore Chimney, the abovementioned field studies proposed a relative resistance to oxidation that typically increased in the order: sphalerite < galena < pyrite < chalcopyrite, which was consistent with the mineral weathering variability observed at Ore Chimney.

Chalcopyrite was observed as the most robust sulfide mineral, with average oxidation rankings of 1 and indicated by SEM-EDX measurements as the primary source for Cu concentrations in the waste rock. Alteration rims of chalcopyrite consisted of a Fe-oxyhydroxide phase that can suppress further oxidation and increase mineral durability in oxidizing environments (Moncur et al., 2009), which is consistent with observations of minimal alteration and low variation in oxidation ranking. Concentrations of Pb, Zn, and Cu were also detected along chalcopyrite alteration zones, which have likely co-precipitated and/or adsorbed to the Fe-oxyhydroxide surfaces (Koski et al., 2008). Alteration zones of pyrite were interpreted as a similar Fe-oxyhydroxide phase bearing Pb, Zn, and Cu from co-precipitation/adsorption reactions. Pyrite was assigned average oxidation rankings of 1.5 and alteration levels varied slightly more than chalcopyrite even though the alteration zones of both minerals were likely composed of a similar Fe-oxyhydroxide phase. However, assessing the alteration extent of sulfide minerals required an observational and semi-quantitative tactic, which provides important context on overall weathering, but restricts the ability to discriminate between minerals of similar alteration extent, such as pyrite and chalcopyrite (Moncur et al., 2005).

Harnois and Moore (1989) identified traces of pyrrhotite (FeS) within the in situ quartz veins at Ore Chimney at a lower abundance than chalcopyrite, pyrite, sphalerite, and galena. There was no pyrrhotite observed in any of the polished grain mounts of waste-rock material, which suggests that any pre-existing

pyrrhotite in the pile at Ore Chimney has been completely weathered (Moncur et al., 2009). In oxidizing environments, pyrrhotite can alter to secondary marcasite (FeS_2), which is a polymorph of pyrite (Blowes and Jambor, 1990). Marcasite has been observed to have a higher reactivity than pyrite (Plumlee, 1999), and the SEM-EDX technique applied herein could not differentiate between polymorphic FeS_2 minerals. Instead, it is likely that the SEM results potentially grouped pyrite and marcasite as the same FeS_2 phase, which may help explain why average pyrite alteration was observed to be higher and vary slightly more than chalcopyrite.

Of the primary sulfide mineral phases observed at Ore Chimney, galena showed the greatest range in alteration extent. In sulfate-laden systems developed from sulfide oxidation, a rim of anglesite (PbSO_4) often forms on galena grains, which significantly reduces galena solubility; thus, maintaining its persistence even in sphalerite-depleted aerobic environments (Moncur et al., 2009). Likewise, carbonate-rich systems with near-neutral pH may favour the formation of cerussite (PbCO_3) along the grain exterior, which is a less soluble phase than anglesite, thereby enhancing galena persistence under the appropriate conditions (Keim and Markl, 2015). Sphalerite oxidation in carbonate-rich environments may favour the precipitation of smithsonite (ZnCO_3) along the grain exterior and serve to control porewater Zn concentrations (Bain et al., 2001). However, smithsonite has a higher solubility than cerussite by two orders of magnitude; therefore, galena may have a higher persistence than sphalerite in carbonate-rich oxidizing systems (Takahashi, 1960; Keim and Markl, 2015). SEM-EDX detected cerussite as an abundant phase along alteration zones of galena and lower proportions of smithsonite along sphalerite rims suggesting that high concentrations of dissolved carbonate may have a stronger control on galena weathering, and Zn is likely being released to a greater extent than Pb. The susceptibility of galena to weathering is recognized to be highly dependent on dissolved sulfate and carbonate, which is difficult to compare across different case studies and therefore omitted from the SAI developed herein and in other settings (Jeong and Lee, 2003; Moncur et al., 2009).

Sphalerite grains were observed as the principal source of waste-rock Zn and Cd concentrations. Moreover, the average molar Fe/Zn ratio determined via SEM-EDX was 0.18 ($\sigma = 0.03$; $n = 57$ grains) yielding an average sphalerite mineral formula of $\sim\text{Zn}_{0.85}\text{Fe}_{0.15}\text{S}$. SEM-EDX spot analyses were measured directly on mineral surfaces and the high reproducibility provides greater confidence than PXRD estimations based on lower sensitivity and limited selections from the ICDD ($\text{Zn}_{0.66}\text{Fe}_{0.34}\text{S}$). SEM-EDX measurements of sphalerite alteration rims typically revealed the presence of smithsonite and/or Zn,Fe-oxyhydroxide phases. Smithsonite may be more concentrated along the outer-most boundary of some sphalerite rims with minor Fe-oxyhydroxide formation favoured near the alteration rim interior (Boulet and Larocque, 1998; Mondillo et al., 2018). However, SEM-EDX was not a sensitive enough technique to accurately distinguish these secondary mineral phases along nm-scale spatial gradients and reported the alteration rim composition as a combination of both.

Similar to pyrite and chalcopyrite, Fe oxidation in ferroan sphalerite can form Fe-oxyhydroxide phases that increase in prevalence with increasing Fe content and slow weathering rates over time (Fanfani, et al., 1996). Jeong and Lee (2003) investigated the oxidation of Fe-bearing sphalerite ($\text{Zn}_{0.84}\text{Fe}_{0.15}\text{Mn}_{0.01}\text{S}$) under a pH range of 5.6 to 6.7 and identified Fe-oxyhydroxides as the main weathering phase. However, sphalerite was still observed to be less resistant than pyrite, which is consistent with findings at Ore Chimney. Therefore, ferroan sphalerite can remain a useful proxy for evaluating the alteration extent of weathered waste-rock systems if the influence of Fe content is understood. Average SAI values ranged from 2 to 3 characterizing minor to moderate weathering of pyrite and chalcopyrite grains and moderate to extensive weathering of sphalerite. Overall, there was minimal variation in sulfide mineral weathering with depth and between trenches at Ore Chimney signifying that weathering processes are occurring at similar rates throughout the waste-rock material irrespective of depth or location.

The precise formulas of Fe-oxyhydroxide phases identified as the alteration product of weathered chalcopyrite, pyrite, and Fe-bearing sphalerite could not be

accurately determined due to a lower chemical sensitivity and spatial resolution of SEM-EDX than other non-destructive X-ray techniques such as electron microprobe analysis (EMPA) (Bao et al., 2021). However, the relative abundances of Fe and O in the alteration zones measured by SEM closely resembled goethite, which is consistent with observations from other studies of mine-waste Fe-sulfide oxidation (Jeong and Lee, 2003; Moncur et al., 2005; Moncur et al., 2009). Likewise, Cu, Pb, and Zn have relatively high adsorption affinities to goethite at a temperature of 10°C and neutral pH, which closely resembles the conditions at Ore Chimney, and corroborates measurements of Cu, Pb, and Zn on alteration zones using SEM-EDX (Rodda et al., 1993).

2.4.4 Total Carbon and Sulfur

Data calculations from total C/S analysis assumes that the total C concentration corresponds to the inorganic carbonate mineral content represented by calcite. Likewise, it is assumed that the total S concentration is directly proportional to the concentration of pyrite. Concentrations of S and C in the waste-rock material showed no depth dependencies and instances of elevated or reduced S and C measurements reflects the indiscriminate distribution of quartz vein fragments associated with the development of the waste-rock pile (Fig. 2.16).

Total C/S measurements revealed an inverse relationship along each trench and elevated S measurements corresponded to lower C concentrations (Fig. 2.11) potentially as a result from carbonate mineral dissolution that buffers sulfide mineral oxidation. Likewise, lower S concentrations corresponded to higher C content, potentially due to the reduced acid generation from less sulfides, and the subsequently lower demand for carbonate dissolution (Blowes et al., 2013). This explanation assumes that primary C/S ratios in the quartz veins proximal to the mineralized ore body were relatively consistent. Although, there is no information in the literature that describes the relative proportions between sulfide and carbonate content prior to weathering (Harnois and Moore, 1989; Archibald, 2012).

Concentrations of S in the coarse-grained fraction were statistically higher than the fine-grained fraction in trench 3, but only by a mean difference of 0.3 wt.%.

Inorganic C measurements showed no difference in concentration between coarse and fine-grained samples along any trench. Therefore, the similar total C/S measurements between coarse- and fine-grained material indicated no discernible partitioning of sulfide and carbonate mineral phases into the coarse- or fine-grained fractions. Accelerated sulfide mineral weathering assumed for the fine-grained fraction due to the higher surface area to volume ratio did not induce a noticeable difference in S concentration compared to the coarse-grained fraction (Smith et al., 2013a). Likewise, carbonate mineral content was not depleted to a greater extent in the fine-grained fraction as a possible result from buffering potentially accelerated sulfide mineral oxidation (Gleisner, 2005).

Smith et al (2013a) compared the total S and C content of waste-rock material (using an *ELTRA CS-2000* Carbon/Sulfur analyzer) across a range of grain sizes between two test piles constructed at the Diavik diamond mine that had been weathering for less than one year. Sulfur at Diavik was hosted predominantly in biotite schist and the test piles were segregated based on S content with higher S concentrations corresponding to a higher proportion of biotite schist in the waste rock (C content was consistent between test piles). The test pile with lower S content ($\mu = 0.035$ wt.% for < 50 mm fraction) measured higher average [S] in < 0.625 mm material than 0.625 to 2.50 mm material by 0.01 wt.%. Comparisons of the same grain size ranges in the test pile with higher S content ($\mu = 0.053$ wt.%) measured 0.04 wt.% higher [S] in the finer grain fraction suggesting that S content increases with decreasing grain size, which may occur to a greater extent when the average S concentration (i.e. biotite schist content) in the test pile is higher.

Harnois and Moore (1989) measured average Zn, Pb, S, and C concentrations (wt.%) of 0.30 [Zn], 0.001 [Pb], 0.26 [S] and 0.89 [C] in bulk samples of the fresh mineralized zone of the Ore Chimney Formation. From combining both grain fractions, concentrations (wt.%) of Zn, Pb, S, and C in the Ore Chimney waste-rock pile averaged 1.56 [Zn], 1.38 [Pb], 2.02 [S], and 1.38 [C]. Measurements from the waste rock are all significantly higher than findings by Harnois and Moore (1989) and this discrepancy may be partially explained by sulfide and carbonate

mineral partitioning in < 2.0 mm sieved fractions from blasting and weathering processes. However, carbonate-bearing quartz veins containing Zn and Pb concentrations (derived from sphalerite and galena) ranging from 1.90 to 6.35 wt.% and 1.60 to 3.73 wt.%, respectively (Archibald, 2012), were determined to comprise a considerable portion of the Ore Chimney waste-rock mineralogy based on quartz concentrations as high as 62 ($\mu = 43$) wt.% measured by PXRD (Fig. 2.2a - c). SEM-EDX infrequently identified sulfide minerals associated with apatite, which is a mineral more commonly observed in the Ore Chimney Formation (biotite schist). Conversely, sulfides associated with quartz grains was a more often occurrence and likely accounted for the higher S concentrations measured in the waste rock compared to observations by Harnois and Moore (1989) (Fig. 2.18a - f).

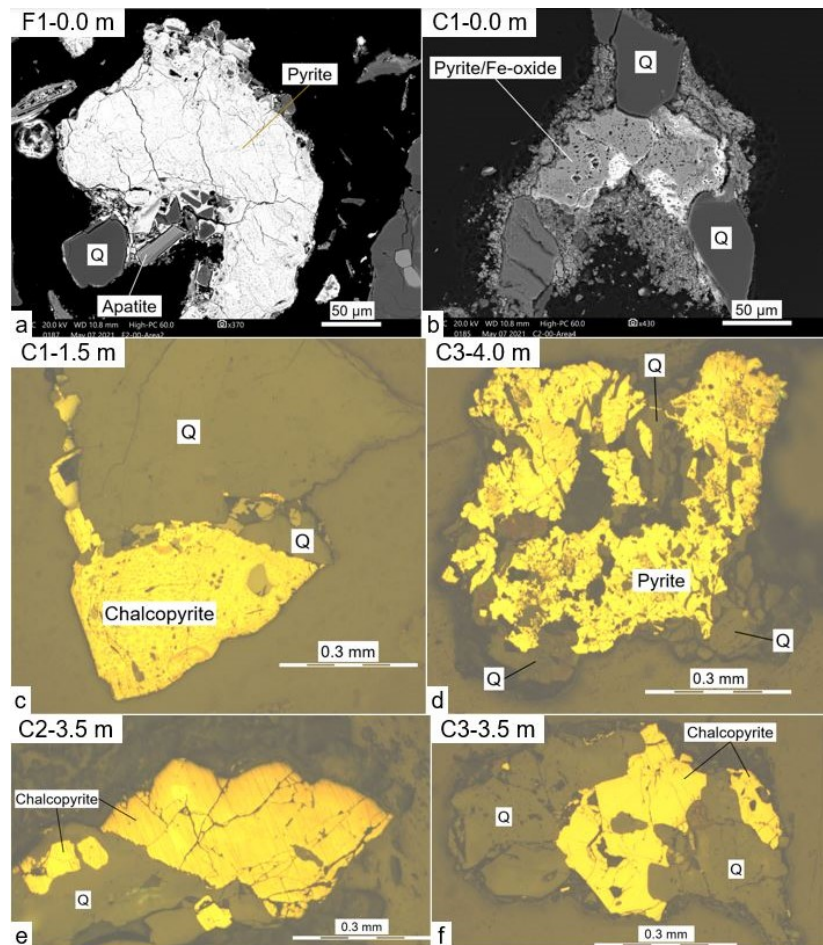


Figure 2.18: BSE images (a and b) and reflected light images (c - f) of sulfide minerals bound with quartz (Q).

Average S concentrations in the Ore Chimney waste rock were significantly higher than the Diavik test piles investigated by Smith et al (2013a). In addition, S concentrations at Ore Chimney were measured to be 0.3 wt.% higher in the coarse-grained fraction (0.5 to 2.0 mm) than the fine-grained fraction (< 0.5 mm) in trench 3 with no measurable differences in trenches 1 and 2 even after ~100 years of exposure. This suggests that sulfides in waste rock sourced from quartz veins have a different resistance to blasting and weathering processes than sulfide minerals hosted in biotite schist. However, ICP-AES/MS measured an increase in Zn and Pb concentrations (in addition to Cu, Cd, Co, and Ni) in the fine-grained fraction of the Ore Chimney waste-rock material by 0.58 and 0.42 wt.%, respectively, suggesting that the partitioning of sphalerite and galena into finer grain sizes was occurring to a smaller extent than what can be resolved with total C/S analysis and emphasizes the importance of incorporating high-resolution solid-phase ICP-AES/MS analyses into geochemical investigations of waste rock. It is likely that a proportion of sulfide minerals are encapsulated within quartz fragments, which are more resistant to blasting and subaerial weathering processes than biotite schist and the lower extent of grain size fractionation of sulfide minerals mainly derived from quartz can be interpreted from ICP-AES/MS but not from total C/S data. It is also important to consider that the proposed “encapsulation effect” may also entrap carbonate minerals, which may inhibit carbonate mineral buffering to some extent and can explain why total C/S analysis did not measure higher C concentrations in the fine-grained fraction of waste-rock material at Ore Chimney.

NPR calculations from total C/S data indicated that grain size has a negligible effect on acid generating capacity and registered most fine- and coarse-grained samples in the UAG ($1 < \text{NPR} < 3$) and NAG ($\text{NPR} > 3$) regions. Only two sample locations (surface and 0.5 m depth in trench 1) measured NPR values < 0.6 and were attributed to relatively low neutralization potentials in the waste rock. Samples with the lowest measurements of both neutralization (NP) and acidification potentials (AP) were observed in trench 3 and situated below the WRP boundary at 4.5 and 5.0 m depth. AP calculations from total C/S analysis assumes that S

measurements are represented by the sulfide (pyrite) content in the waste rock; however, sulfide mineral oxidation generates sulfate, which can achieve saturation in the porewaters and precipitate as common secondary minerals such as gypsum, which is not a pH dependent process and can overestimate AP values if left unquantified (Nordstrom and Alpers, 1999; Atherton, 2017). The solid-phase sulfide and sulfate content was not distinguished herein; however, several analytical methods to quantify sulfate content exist and are described by Pillai et al, (2007) and Mussa et al, (2009).

AP calculations also assume that the S concentrations are derived exclusively from pyrite where both ferrous iron and sulfide are oxidized to produce two moles of acidity per mole of sulfur (Jambor et al., 2002; Blowes et al., 2013). At Ore Chimney, sphalerite and galena grains were observed by reflected light microscopy and SEM-EDX to comprise a substantial component of the sulfide mineral assemblage (Fig. 2.9a - d). Sphalerite and galena can generate eight moles of acidity per mole of sulfur when oxidized by ferric iron; however, only sulfide undergoes oxidation and oxidative dissolution in the presence of oxygen (O_2) is a non-acid generating process (equation 1) (Plumlee, 1999; Seal and Foley, 2002; Moncur et al., 2009; Heidel et al., 2013). The aerobic conditions at Ore Chimney likely favour oxygen as the primary oxidant, which may result in overexaggerated AP estimations. Likewise, NPR calculations assume that the entire S and C content is available to be utilized, which may not be the case for S and C content derived from quartz vein material due to potential embedment of sulfide and carbonate grains within the robust mineral structure of quartz (Sobek et al., 1978).

Pedretti et al (2017) performed reactive transport simulations with the modeling software MIN3P (Mayer et al., 2002) to investigate how different spatial distributions of acid-generating and acid-neutralizing minerals of the same proportions can influence the pH of drainage waters. Results indicated that effluent pH had a stronger dependence on the random spatial distribution of acid-producing and acid-consuming minerals than bulk NPR values, and subtle reconfigurations

of throughflow media in some instances predicted the likelihood of systems with NPR values of 2 to produce AMD after ~100 years. The spatial distribution of total C/S concentrations at Ore Chimney was considerably different between the three trenches (Fig. 2.11a - c) implying that NPR predictions are rather uncertain. However, abundant inorganic carbon detected in the waste rock from total C/S analysis and PXRD suggests that it is unlikely for Ore Chimney to generate AMD in the near future.

2.4.5 Implications

The solid-phase geochemical signatures that remain in the waste-rock pile after ~100 years of weathering indicate that different sulfide minerals altered to different extents with pyrite and chalcopyrite showing minimal alteration and sphalerite showing the highest degrees of weathering. Galena weathering was highly variable, which may be attributed to inconsistencies in secondary cerussite formation due to variable carbonate content and the absence of pyrrhotite may suggest complete removal from the waste-rock pile. All the sulfide minerals showed evidence of weathering that was consistent with depth and between sampling locations indicating that aerobic conditions are consistent throughout the entire waste-rock pile, which may be a function of coarser grain size accumulation at the base of the pile from edge dumping coupled with long-term subaerial exposure (Lahmira et al., 2016).

The rich carbonate content (1.38 wt.% C) at Ore Chimney has been observed to counteract the aerobic oxidation of high concentrations of sulfur (2.02 wt.% S) and subjected the waste-rock pile to neutral mine drainage for ~100 years. Comprehensive studies on young waste rock (i.e. < 1 year of exposure above ground surface), such as the Diavik mine (Smith et al., 2013a; Smith et al., 2013b) contain much lower carbon (~0.02 wt.%) and sulfur (0.16 wt.%) content that was observed to generate acidic drainage waters after as early as five years (Langman et al., 2014). Results indicate that significantly higher carbonate concentrations are required to prevent potential acid generation after ~100 years of weathering as observed at Ore Chimney.

Moncur et al (2009) observed the entire removal of low Fe-bearing sphalerite [$Zn_{0.96}Fe_{0.04}S$; (Moncur et al., 2005)] from the upper portion of a tailings profile that was associated with low pH and 70 years of oxidation. In contrast, Jeong and Lee (2003) investigated carbonate-rich waste rock that was subjected to 50 years of weathering under circumneutral pH and observed that Fe-bearing sphalerite ($Zn_{0.84}Fe_{0.15}Mn_{0.01}S$) was extensively weathered but still abundant in the upper portions of the pile indicating that sphalerite mineral resistance increases with increasing Fe content and may weather at slower rates when pH is maintained at circumneutral levels. Likewise, sphalerite ($\sim Zn_{0.85}Fe_{0.15}S$) in the ~ 100 -year-old Ore Chimney waste-rock pile was moderately to extensively weathered but persisted throughout the entire pile including the upper portions. The extent of sphalerite oxidation at Ore Chimney was similar to observations by Jeong and Lee (2003) indicating that Fe content in sphalerite coupled with a high carbonate content in the waste rock can significantly slow weathering rates over time especially between 50 to 100 years of exposure above ground surface.

The remaining presence of moderately to extensively weathered sphalerite throughout the waste-rock pile, especially in the fine-grained fraction of waste rock indicates continual weathering after ~ 100 years and predicts sphalerite to deplete before chalcopyrite, pyrite, and galena. The relatively high carbonate content comprised of calcite and dolomite has prevented the generation of AMD and will continue to buffer acidity until calcite is depleted where dolomite is expected to become the primary mineral buffering phase and may elevate dissolved concentrations of Mg and maintain near-neutral pH over an extended period. Total sulfur concentrations were consistent between grain size fractions, but ICP-AES/MS detected a slight enrichment of Zn and Pb in the fine-grained fraction of waste-rock material providing some indication that blasting and weathering processes partitions sulfides into finer grain sizes. However, the partitioning of sulfur into finer grain sizes is more evident for sulfide minerals derived from biotite schist (Smith et al., 2013a) compared to sulfidic quartz veins at Ore Chimney, suggesting that the source lithology for sulfide minerals plays an important role in sulfide weathering.

Chapter 3: Porewater Chemistry

3.1 Introduction

The oxidation of sulfide minerals is thermodynamically favourable in ambient aerobic settings and predicts the release of metals and acidity into proximate porewaters, which has long been recognized and described as “acid mine drainage” (AMD) (Nordstrom, 1982; Akcil and Koldas, 2006). However, waste rock piles are multi-component systems that often host carbonate minerals with an affinity to counteract the release of acidity through neutralization reactions that maintain near-neutral pH, with the most common examples being calcite and dolomite (Parbhakar-Fox and Lottermoser, 2017; Bao et al., 2020). As such, carbonate-rich waste-rock piles have been observed to maintain near-neutral pH throughflow waters, which is appropriately described as “neutral mine drainage” (NMD) (Jeong and Lee, 2003; Nordstrom et al., 2015). However, carbonate buffering minerals persist in mine-waste systems in finite amounts and acid generation from the continual weathering of sulfides can deplete carbonate minerals entirely (Moncur et al., 2005). The neutralization potential of mine-waste systems is both a function of buffering availability (i.e. abundance) and exposure time (Blowes et al., 2013). Under longer exposure times or in systems with carbonate deficiency, pH levels may be regulated by the availability of less reactive primary and secondary carbonate, hydroxide, and aluminosilicate minerals in a succession summarized by Johnson et al (2000) and Bain et al (2001).

Transition metals dissolved in waste-rock porewaters are primarily derived by the oxidative dissolution of sulfide minerals, which is often generalized as “weathering” (Amos et al., 2015). Iron-bearing sulfide oxidation typically favours the formation of Fe-oxyhydroxide phases and the adsorption of metals onto these alteration surfaces has been observed as a common sink in a variety of mine-waste settings (Zhixun, 1996; Balistrieri et al., 2008; Demers et al., 2013; Skierszkan et al., 2016). In many cases, amorphous ferrihydrite is the expected Fe-oxyhydroxide phase above a pH of 4 and conditions in aerobic subaerial systems favour the

recrystallization and transformation of ferrihydrite into goethite over time (Lee et al., 2002; Stipp et al., 2002). Likewise, the adsorption of transition metals onto the surface of goethite has been observed as a pH-dependent equilibrium process where metal adsorption affinities decrease at lower pH due to competition with hydronium ions (Kooner, 1993; Rodda et al., 1993; Rose and Bianchi-Mosquera, 1993; Abdus-Salam and Adekola, 2005). The relationship between goethite adsorption affinity and pH usually differs among divalent transition metals where a reduction in pH from alkaline to acidic levels generally desorbs metals into solution in the order $Ni \geq Co > Cd > Zn > Pb \geq Cu$ (Blowes and Jambor, 1990; Rose and Bianchi-Mosquera, 1993; Jurjovec et al., 2002; Swedlund et al., 2009; Mohapatra et al., 2011; Komárek et al., 2018).

Progressive research involving seasonal and yearly monitoring of drainage quality comprises a substantial component of the mine-waste literature with examples including Diavik (Neuner et al., 2013; Pham et al., 2013; Smith et al., 2013b), Faro (Lewkowicz and Bonnaventure, 2011; Mead, 2011; Bao et al., 2020), and Meadowbank (Borgne et al., 2018; Boulanger-Martel et al., 2021; Yi, 2021) mine. However, these mining operations are situated in high-latitude regions influenced by permafrost and lower levels of precipitation, which can mitigate the transport of contaminants (Pham et al., 2015). Vriens et al (2019) investigated the changing geochemical signatures of five waste-rock test piles of varying lithologies that weathered over a ten-year time frame at an average annual temperature of 6°C at the Antamina mine. Results indicated that dissolved metals in the porewaters at the base of the waste-rock piles were controlled by secondary minerals such as gypsum, Cu,Zn-hydroxysulfate, -hydroxycarbonate, and Fe-oxyhydroxides and adsorption to Fe-oxyhydroxide surfaces during the incipient stages of weathering (i.e. < 1 year), which remained relatively consistent throughout the ten-year study. Vriens et al (2019) discovered that evaluating weathering mechanisms over multi-year timescales was difficult to interpret by monitoring only the basal porewaters, which can be influenced by overlying geochemical signatures. Furthermore, unique climatic conditions at Antamina and mineralogical heterogeneities between

test piles made it difficult to compare results in a broader context without investigating in situ porewater chemistry at different pile depths.

Smith et al (2021) collected porewaters from in situ waste-rock samples along the surface, middle, and base of a deconstructed 15 m deep waste-rock pile at the Detour Lake mine that had weathered for approximately 30 years. Porewaters were observed to maintain near-neutral pH throughout the entire depth profile suggesting that carbonate mineral buffering had been an active process over the past 30 years. However, NPR estimations predicted samples to be potentially acid generating or have uncertain acid generation capacity suggesting that the Ca-carbonate content was depleting from the waste-rock pile. A 30-year timescale is long for waste-rock mineral weathering studies in the literature but is still quite short in comparison to actual timeframes of weathering for real waste-rock piles, especially those from abandoned mine sites. This chapter aims to supplement solid-phase metal release mechanisms at high spatial resolution (0.5 m) examined in chapter 2 by investigating relationships in the porewaters to better understand the overall mobility of metals after ~100 years of weathering.

3.2 Methods

3.2.1 Sample Preparation

For a description of sample locations of the waste-rock site at Ore Chimney and methods for waste-rock sampling for porewater extractions, refer to section 2.2.1 in Chapter 2. Samples of raw waste-rock material (i.e. undried and unsieved) were transferred into modified Falcon™ tubes for porewater extraction (Atherton, 2017; Smith et al., 2021). Conical 50 mL Falcon™ centrifuge tubes were shortened to 45 mL and a 2 mm hole was drilled at the base and lined with glass wool (*Sigma-Aldrich*, product number: 18421). An additional set of Falcon™ centrifuge tubes were shortened to 10 mL and placed underneath the modified 45 mL tubes in the centrifuge holder to collect the separated porewaters (Fig. 3.1a and b). Porewater samples were separated from waste-rock material using a *Hettich Rotofix 32A* benchtop centrifuge rotating at 4000 RPM for five minutes. Centrifuging the same

sample for another five minutes did not separate any additional volume of porewater, which justified five minutes as an appropriate time for centrifugation. All sample vials and porewater sampling vessels were thoroughly washed in a 2% ultra-pure nitric acid and deionized water solution. A minimum volume of 25 mL of porewater sample for chemical analyses was obtained from 16-24 aliquots of waste-rock material weighing approximately 100 g (1 aliquot = 1 modified Falcon™ tube filled with 40 mL of sample material; Fig. 3.1a). All porewater samples for ion analyses were filtered to 0.45 μm. Porewater samples were transferred into unacidified 15 mL sample vials for anion chromatography and 5 mL sample vials acidified with 0.1 mL of ultra-pure nitric acid for ICP-AES/MS measurements. Additional aliquots were collected for immediate laboratory analysis and small volumes of porewater sample and sample reagents (0.1 to 5.0 mL) were measured and transferred using a VWR VE1000 micropipette.

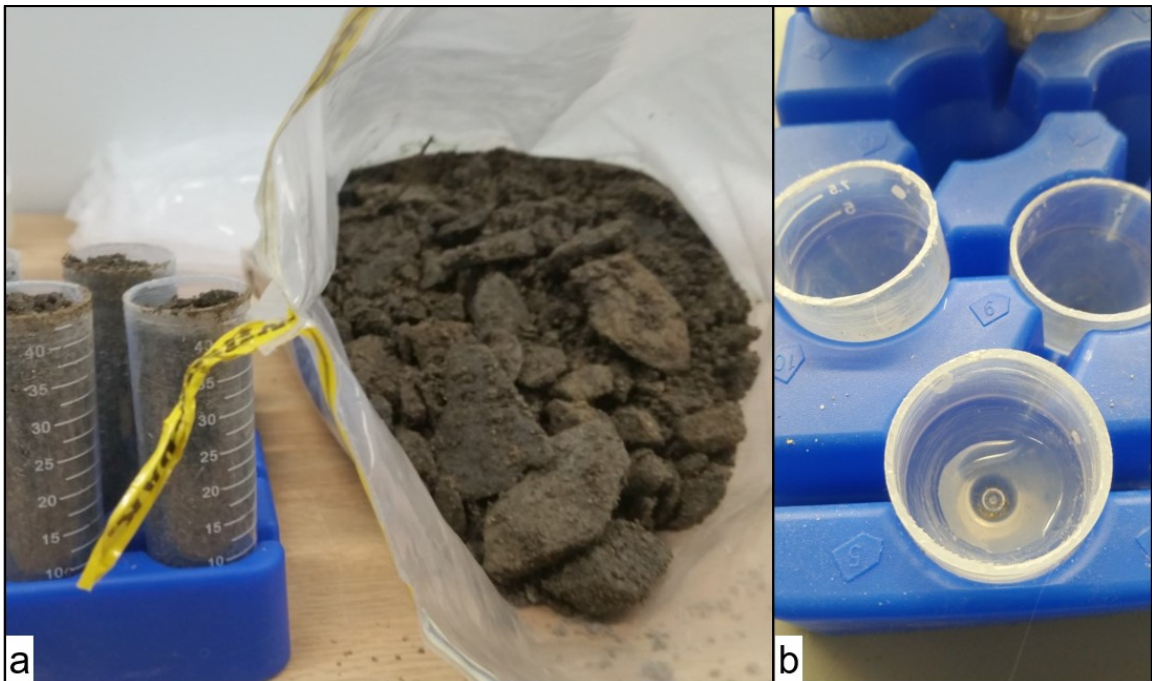


Figure 3.1: a) Falcon™ tubes shortened to 45 mL and filled with loose waste-rock material (2 mm hole drilled at the base and lined with glass wool), b) Falcon™ tubes shortened to 10 mL and placed underneath for porewater collection.

3.2.2 Analytical Methods

Porewater pH and Eh were determined using a VWR model *H30PCO symphony™* handheld probe. A *Hach DR 1900* portable spectrophotometer was used to perform immediate chemical analyses for sulfate (SO_4^{2-}) (Method 10248; Hach, 2013), sulfide (HS^-) (Method 10254; Hach, 2014a), alkalinity ($CaCO_3$) (Method 10239; Hach, 2014b), and ferrous iron (Fe^{2+}) (Method 8146; Hach, 2014c). Porewater samples for major and trace cation analyses (ICP-AES/MS) and anion chromatography (IC) were performed at the Geochemistry Laboratory at the University of Ottawa. Porewater samples for major and trace cation analyses were diluted with deionized water to contain 1% molar concentration of ultra-pure nitric acid. Major cations were quantified by ICP-AES using an *Agilent 5110 SVDV CCD* spectrometer. Trace metal concentrations were determined by ICP-MS using an *Agilent 8800 QQQ triple quadrupole* mass spectrometer. All calibration standards for cation analyses were prepared using an ultra-pure 1% nitric acid solution. Anion concentrations were measured in un-acidified water samples via anion IC using a *DIONEX ICS-2100* chromatograph and all analyses were calibrated using external standards (N. De Silva, personal communications, 2021).

Porewater chemistry data compiled from probe and spectrophotometry methods, ICP-AES/MS, and anion IC were used to generate mineral saturation indices at 10°C using PHREEQC software version 3.4.0-12927 with the minteq.v4 database (Parkhurst and Appelo, 1999). Depth plot saturation indices (SI) were fitted with vertical dashed lines to indicate the SI boundary between -0.5 and +0.5 and samples registering within this range were considered to be near saturation (Ettler et al., 2009; Chidambaram et al., 2012; Gawdzik et al., 2015).

3.3 Results

Waste-rock samples for solid-phase analyses (Chapter 2) and porewater extractions were collected in tandem. Therefore, the beginning of the estimated transitional boundary between the waste-rock pile and natural overburden material (between 4.5 to 5.0 metres deep in trench 2 and 4.0 to 4.5 metres deep in trench

3) also applied to the samples collected for porewater extractions. The porewater chemical depth plots presented hereafter indicate these non-discrete boundary estimations accordingly as “WRP boundary” and the samples located above these boundaries were referred to as the waste-rock porewaters (n = 13 in trench 1, n = 12 in trench 2, and n = 11 in trench 3). Likewise, only the samples representing waste-rock porewaters (i.e. excluding the samples below the WRP boundary) were included in statistical comparisons and the annotated results summary unless indicated otherwise.

The results presented herein compare average concentration measurements between trenches and spatial differences within a given trench (i.e. vertical trends) but only trends and differences with a statistical significance are reported. Vertical trends were interpreted from a two-tailed Pearson linear regression analysis with 95% confidence and compared to critical Pearson correlation (R^2_{critical}) values of 0.553, 0.576, and 0.602 for trenches 1, 2, and 3, respectively (Degrees of Freedom = n - 2) (Weatherington et al., 2012). Rank sum two-tailed t-tests were conducted to compare samples between trenches. Two-tailed t-test comparisons did not include data from duplicate samples and only considered samples between 0.0 to 4.0 m depth to account for the transition between waste rock and overburden material observed in trenches 2 and 3 (n = 9). Vertical trends with statistically insignificant correlation coefficients ($R^2_{\text{calculated}} < R^2_{\text{critical}}$) and t-test comparisons of population means (μ) with standard deviations (σ) yielding no statistical difference ($\alpha > 0.05$) were interpreted as such and not reported herein.

3.3.1 Porewater Chemistry

Spectrophotometric analysis performed immediately after porewater extractions revealed concentrations of dissolved ferrous iron (Fe^{2+}) and sulfide (HS^-) below the detection limit. Furthermore, sulfate (SO_4^{2-}) measurements were conducted both immediately after porewater extractions via spectrophotometry and subsequently thereafter by anion IC. Sulfate concentrations from anion IC were consistently higher than spectrophotometry measurements by an average of 15% ($\sigma = 9\%$). Spectrophotometry has a lower sensitivity than anion IC and was

therefore omitted from the results presented below especially considering that pre-sampled in situ waste rock was likely at equilibrium with atmospheric oxygen from under-range Fe^{2+} and HS^- measurements and therefore not redox-sensitive.

The average pH in the Ore Chimney waste-rock porewaters was 7.0 ($\sigma = 0.5$), 7.3 ($\sigma = 0.4$), and 7.5 ($\sigma = 0.5$) in trenches 1, 2, and 3, respectively (Fig. 3.2a - c). The lower average pH values measured in trench 1 correspond to pH readings of 6.5 and 6.4 at 0.5 and 4.0 m depth, respectively. Porewater Eh measurements averaged 434 ($\sigma = 50$), 414 ($\sigma = 40$), and 414 ($\sigma = 20$) mV in trenches 1, 2, and 3, respectively (Fig. 3.2d - f). The higher average Eh reading and standard deviation observed in trench 1 were attributed to elevated readings of 547 and 486 mV at 0.5 and 4.0 m depth. However, porewater pH and Eh measurements were not statistically different between trenches nor signified a relationship with depth in any trench.

The average porewater alkalinity concentrations were 53.7 ($\sigma = 17.7$), 52.3 ($\sigma = 23.2$), and 76.4 ($\sigma = 38.6$) mg/L CaCO_3 in trenches 1, 2, and 3, respectively (Fig. 3.2g - i). Alkalinity concentrations were lowest in trench 2 and statistically higher in trench 3 by a mean difference of 30.6 mg/L CaCO_3 ($\alpha = 0.01$). None of the trenches showed a statistical relationship between concentration and depth. Sulfate (SO_4^{2-}) concentrations averaged 1,046.0 ($\sigma = 499.0$), 541.1 ($\sigma = 324.7$), and 1,111.8 ($\sigma = 835.4$) ppm in trenches 1, 2, and 3, respectively (Fig. 3.2j - l). Average SO_4^{2-} concentrations were lowest in trench 2 and statistically higher in trenches 1 and 3 by mean differences of 497.9 and 513.9 ppm ($\alpha = 0.007$ and 0.05). Concentrations of SO_4^{2-} statistically increased from 629 to 1578 (0.0 to 5.0 m depth), from 338 to 1293 (0.0 to 4.5 m depth), and from 140 to 1883 ppm (0.0 to 4.0 m depth) in trenches 1, 2, and 3 ($R^2_{\text{calc}} = 0.56, 0.63, \text{ and } 0.85$, respectively).

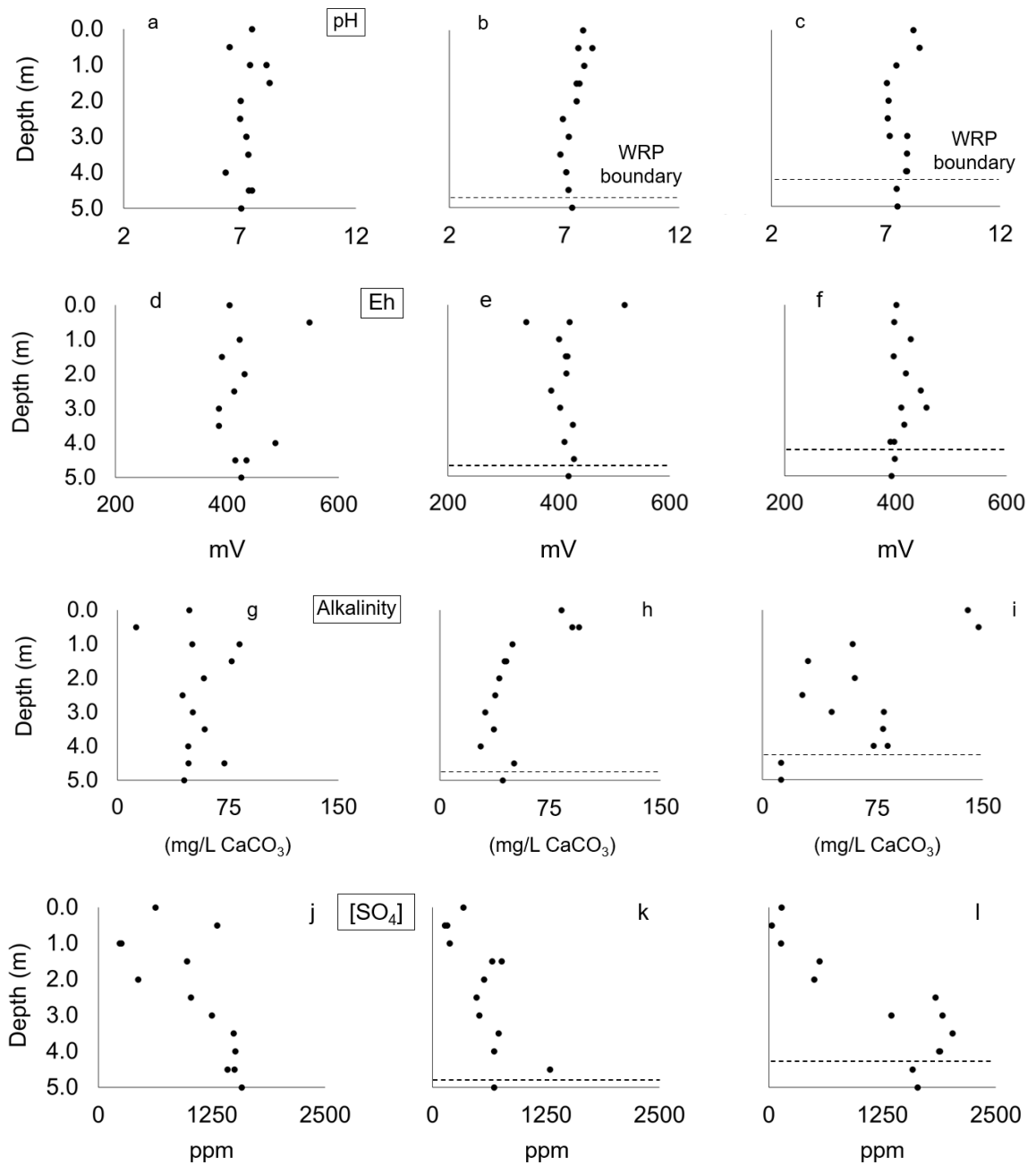


Figure 3.2: Aqueous-phase pH, Eh, alkalinity, and sulfate (SO₄²⁻) depth plots for trench 1 (left), trench 2 (middle), and trench 3 (right).

The average sodium (Na) concentrations were 28.1 ($\sigma = 6.4$), 22.8 ($\sigma = 4.1$), and 31.5 ($\sigma = 8.7$) ppm in trenches 1, 2, and 3, respectively (Fig. 3.3a - c). Average Na concentrations were lowest in trench 2 and statistically higher in trenches 1 and 3 by mean differences of 7.6 and 8.3 ppm ($\alpha = 0.004$ and 0.05). Sodium concentrations were observed to statistically increase from 20.2 ppm at the surface of the pile (0.0 m) to 46.1 ppm at 4.0 m depth in trench 3 ($R^2_{\text{calc}} = 0.72$). Porewater potassium (K) concentrations averaged 32.3 ($\sigma = 8.7$), 24.6 ($\sigma = 5.5$), and 37.0 (21.6) ppm in trenches 1, 2, and 3, respectively (Fig. 3.3d - f). Average K concentrations were lowest in trench 2 and statistically higher in trench 1 by a mean difference of 7.5 ppm ($\alpha = 0.02$). Moreover, K concentrations statistically increased from 20.2 ppm at the surface of the pile to 58.5 ppm at 4.0 m depth in trench 3 ($R^2_{\text{calc}} = 0.72$).

Porewater calcium (Ca) concentrations averaged 268.4 ($\sigma = 110.9$), 159.2 ($\sigma = 79.6$), and 247.7 ($\sigma = 155.2$) ppm in trenches 1, 2, and 3, respectively (Fig. 3.3g - i). Average Ca concentrations were lowest in trench 2 and statistically higher in trench 1 by a mean difference of 107.2 ppm ($\alpha = 0.006$). Calcium concentrations statistically increased from 176.6 to 366.3 (0.0 to 5.0 m depth), from 115.3 to 335.1 (0.0 to 4.5 m depth), and from 61.7 to 412.2 ppm (0.0 to 4.0 m depth) in trenches 1, 2, and 3 ($R^2_{\text{calc}} = 0.59, 0.59, \text{ and } 0.89$, respectively). The average magnesium (Mg) concentrations were 40.0 ($\sigma = 18.7$), 14.6 ($\sigma = 5.4$), and 51.8 ($\sigma = 44.4$) ppm in trenches 1, 2, and 3, respectively (Fig. 3.3j - l). Average Mg concentrations were lowest in trench 2 and statistically higher in trenches 1 and 3 by mean differences of 25.8 and 37.6 ppm ($\alpha = 0.002$ and 0.04). Porewater Mg concentrations may increase with depth; however, the relationship was not statistically significant ($R^2_{\text{calc}} = 0.50, 0.35, \text{ and } 0.51$ for trenches 1, 2, and 3, respectively).

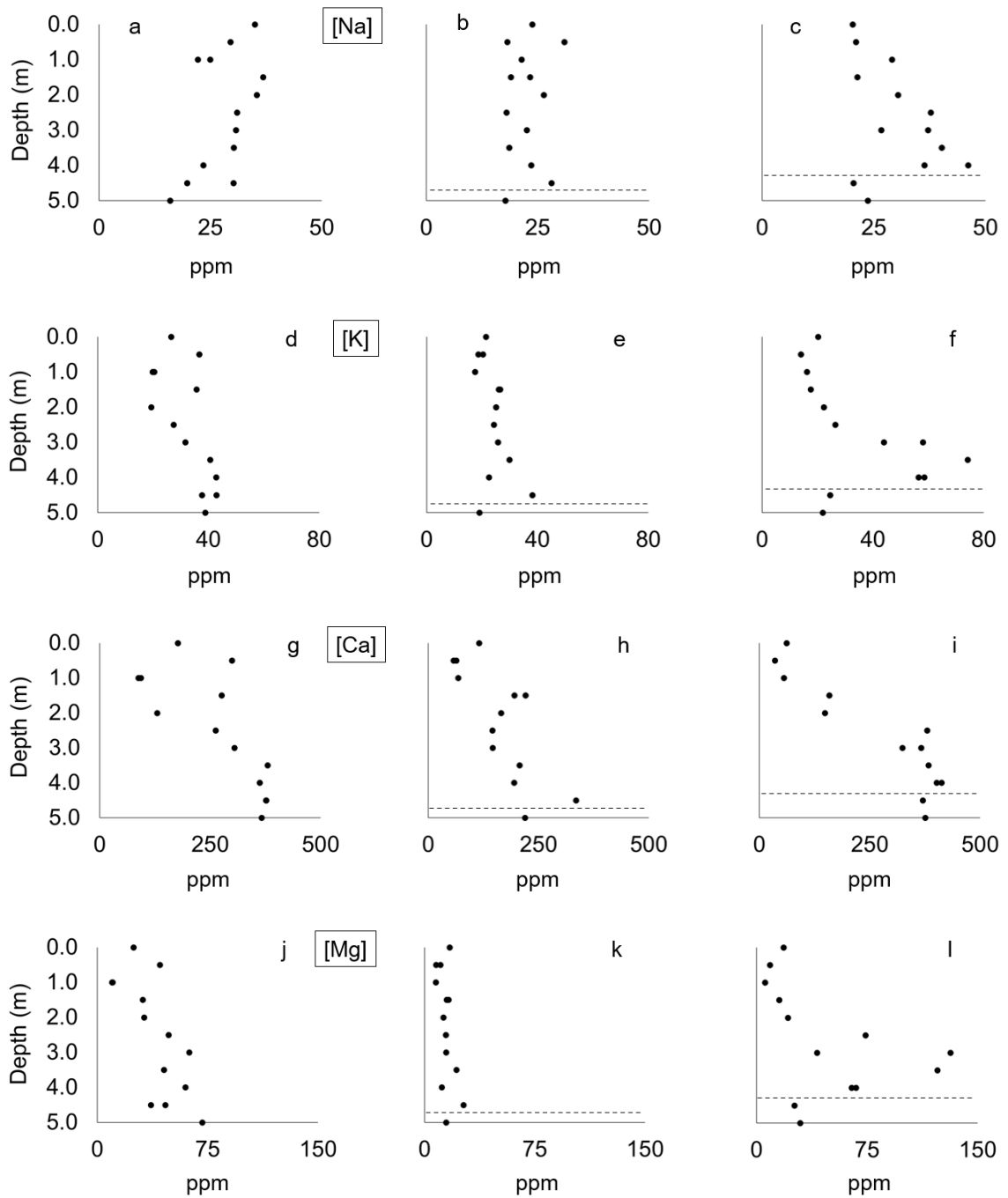


Figure 3.3: Aqueous-phase sodium (Na), potassium (K), calcium (Ca), and magnesium (Mg) depth plots for trench 1 (left), trench 2 (middle), and trench 3 (right).

Iron (Fe) concentrations in the porewaters averaged 9.2 ($\sigma = 5.9$), 5.9 ($\sigma = 1.5$), and 11.1 ($\sigma = 8.1$) ppb in trenches 1, 2, and 3, respectively (Fig. 3.4a - c). Average Fe concentrations were lowest in trench 2 and statistically higher in trenches 1 and 3 by mean differences of 2.9 and 6.1 ppb ($\alpha = 0.04$ and 0.05). There was no statistically significant relationship between Fe concentration and depth in any trench. The average Copper (Cu) concentrations measured 16.1 ($\sigma = 20.6$), 15.0 ($\sigma = 6.8$), and 11.7 ($\sigma = 11.7$) ppb in trenches 1, 2, and 3, respectively (Fig. 3.4d - f). The higher relative standard deviations measured in trenches 1 and 3 corresponded to anomalously high Cu readings at 0.5 m in trench 1 (82.6 ppb) and 2.5 m depth in trench 3 (45.7 ppb). A statistical increase in Cu concentrations was observed in trench 2 (7.2 ppb at the surface of the pile to 23.3 ppb at 4.5 m depth; $R^2_{\text{calc}} = 0.84$). No depth dependent trends were observed in trenches 1 and 3 even if the anomalies are excluded.

Porewater zinc (Zn) concentrations averaged 19,400 ($\sigma = 23,300$), 15,900 ($\sigma = 12,200$), and 14,100 ($\sigma = 22,000$) ppb in trenches 1, 2, and 3, respectively (Fig. 3.4g - i). Anomalously high Zn measurements at 0.5 m in trench 1 (87,500 ppb) and 2.5 m depth in trench 3 (74,900 ppb) accounted for their higher relative standard deviations. Zinc concentrations statistically increased from 700 ppb at the surface of the pile to 31,600 ppb at 4.5 m depth in trench 2 ($R^2_{\text{calc}} = 0.76$) but not in trenches 1 and 3 despite excluding the anomalous readings. The average lead (Pb) concentrations measured 68.5 ($\sigma = 79.2$), 49.4 ($\sigma = 18.7$), and 35.4 ($\sigma = 16.6$) ppb in trenches 1, 2, and 3, respectively (Fig. 3.4j - l). The high relative standard deviation measured in trench 1 corresponded to an anomalously high reading at 0.5 m depth (322.3 ppb). Lead concentrations statistically increased in trench 2 from 31.4 ppb at the surface of the pile to 72.3 ppb at 4.5 m depth ($R^2_{\text{calc}} = 0.79$).

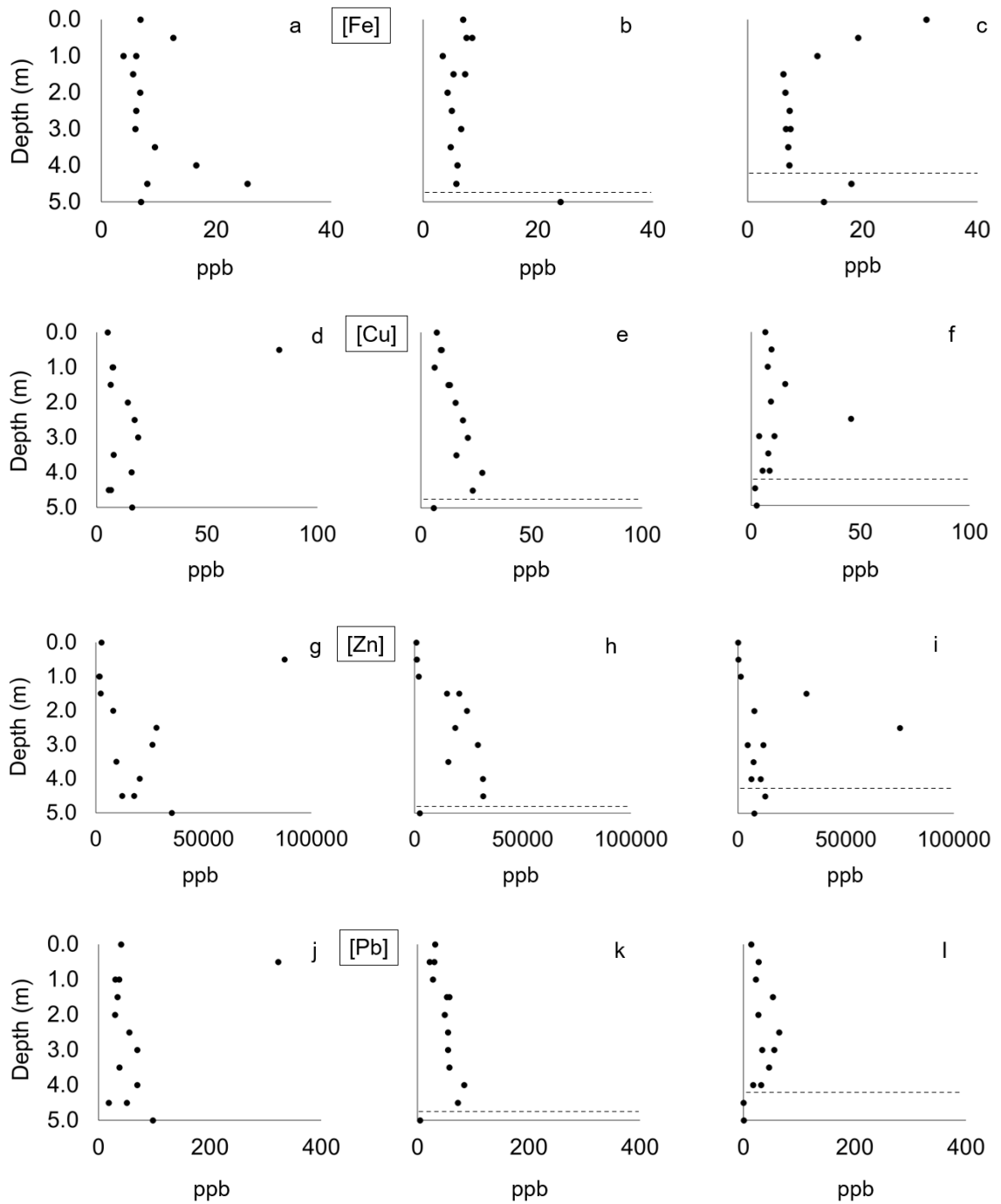


Figure 3.4: Aqueous-phase iron (Fe), copper (Cu), zinc (Zn), and lead (Pb) depth plots for trench 1 (left), trench 2 (middle), and trench 3 (right).

The average manganese (Mn) concentrations were 348.7 ($\sigma = 598.6$), 64.5 ($\sigma = 44.1$), and 351.0 ($\sigma = 1,075.5$) ppb in trenches 1, 2, and 3, respectively (Fig. 3.5a - c). The higher relative standard deviations measured in trenches 1 and 3 corresponded to anomalously high Mn readings at 0.5 m in trench 1 (2,214.9 ppb) and 2.5 m depth in trench 3 (3,592.2 ppb). Manganese concentrations showed no statistical relationship with depth in any trench. However, trench 1 yielded a R^2_{calc} value of 0.544 when the anomalous measurement at 0.5 m depth was removed, which is statistically insignificant (< 0.553) but may signify that Mn concentrations increased from 53.2 ppb at the surface of the pile to 679.1 ppb at 5.0 m depth. Porewater cadmium (Cd) concentrations averaged 448.4 ($\sigma = 353.5$), 475.1 ($\sigma = 330.5$), and 339.0 ($\sigma = 403.1$) ppb in trenches 1, 2, and 3, respectively (Fig. 3.5d - f). Anomalously high Cd measurements at 0.5 m depth in trench 1 (1,226.1 ppb) and 2.5 m depth in trench 3 (1,336.2 ppb) accounted for their higher relative standard deviations. Cadmium concentrations in trench 2 statistically increased from 69.2 ppb at the surface of the pile to 895.1 ppb at 4.5 m depth ($R^2_{\text{calc}} = 0.69$). No depth dependent trends were observed in trenches 1 or 3, even when the anomalies are excluded.

Porewater arsenic (As) concentrations averaged 1.4 ($\sigma = 0.7$), 1.5 ($\sigma = 1.8$), and 3.0 ($\sigma = 3.8$) ppb in trenches 1, 2, and 3, respectively (Fig. 3.5g - i). Average As concentrations were highest in trench 3 and statistically lower in trench 2 by a mean difference of 1.9 ppb ($\alpha = 0.05$). There was no statistically significant relationship between As concentration and depth in any trench. The average antimony (Sb) concentrations measured 15.0 ($\sigma = 13.2$), 22.4 ($\sigma = 9.3$), and 12.0 ($\sigma = 4.8$) ppb in trenches 1, 2, and 3, respectively (Fig. 3.5j - l). Average Sb concentrations were lowest in trench 3 and statistically higher in trench 2 by a mean difference of 9.2 ppb ($\alpha = 0.05$). Concentrations of Sb were not observed to statistically change with depth in any trench.

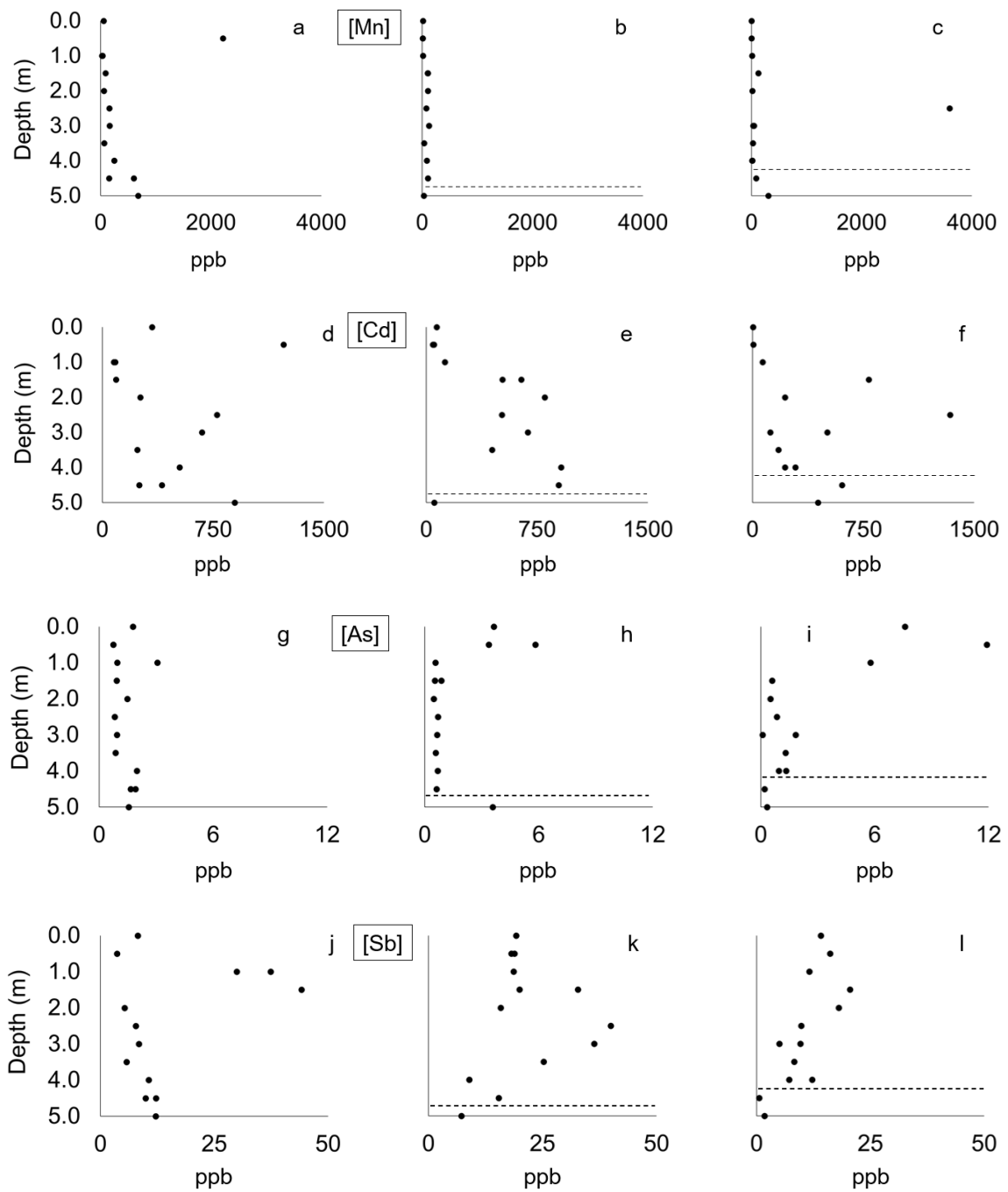


Figure 3.5: Aqueous-phase manganese (Mn), cadmium (Cd), arsenic (As), and antimony (Sb) depth plots for trench 1 (left), trench 2 (middle), and trench 3 (right).

The average titanium (Ti) concentrations measured 1.1 ($\sigma = 1.1$), 0.2 ($\sigma = 0.2$), and 0.5 ($\sigma = 0.5$) ppb in trenches 1, 2, and 3, respectively (Fig. 3.6a - c). Average Ti concentrations were observed to be lowest in trench 2 and higher in trenches 1 and 3 by mean differences of 0.7 and 0.4 ppb ($\alpha = 0.04$ and 0.04). However, several Ti measurements in trenches 2 and 3 were below the detection limit of 0.13 ppb and created difficulties for quantitative comparisons. Titanium concentrations showed no relationship with depth in any trench. Porewater chromium (Cr) concentrations averaged 0.3 ($\sigma = 0.1$), 0.2 ($\sigma = 0.03$), and 0.2 ($\sigma = 0.05$) ppb in trenches 1, 2, and 3, respectively (Fig. 3.6d - f). Chromium concentrations were consistent with depth and showed no statistical difference in concentration between any of the trenches.

Average porewater cobalt (Co) concentrations were 16.2 ($\sigma = 25.0$), 7.1 ($\sigma = 5.3$), and 11.6 ($\sigma = 27.7$) ppb in trenches 1, 2, and 3, respectively (Fig. 3.6g - i). The higher relative standard deviations measured in trenches 1 and 3 corresponded to anomalously high Co readings at 0.5 m depth in trench 1 (95.9 ppb) and 2.5 m depth in trench 3 (94.8 ppb). Linear regression analysis of the raw data revealed no statistical relationship between concentration and depth. However, trench 1 yielded a R^2_{calc} value of 0.59 when the anomalous measurement at 0.5 m depth was removed, which may indicate an increase from 2.9 ppb at the surface of the pile to 29.3 ppb at 5.0 m depth.

The average nickel (Ni) concentrations measured 37.1 ($\sigma = 42.1$), 17.5 ($\sigma = 14.0$), and 35.4 ($\sigma = 70.1$) ppb in trenches 1, 2, and 3, respectively (Fig. 3.6j - l). Anomalously high Ni measurements at 0.5 m depth in trench 1 (166.0 ppb) and 2.5 m depth in trench 3 (244.8 ppb) accounted for their higher relative standard deviations. With the anomalies excluded from the dataset, Ni concentrations increased from 13.1 to 66.4 (0.0 to 5.0 m depth), from 3.3 to 36.9 (0.0 to 4.5 m depth), and from 1.4 to 22.2 ppm (0.0 to 4.0 m depth) in trenches 1, 2, and 3 ($R^2_{\text{calc}} = 0.68, 0.69, \text{ and } 0.63$, respectively).

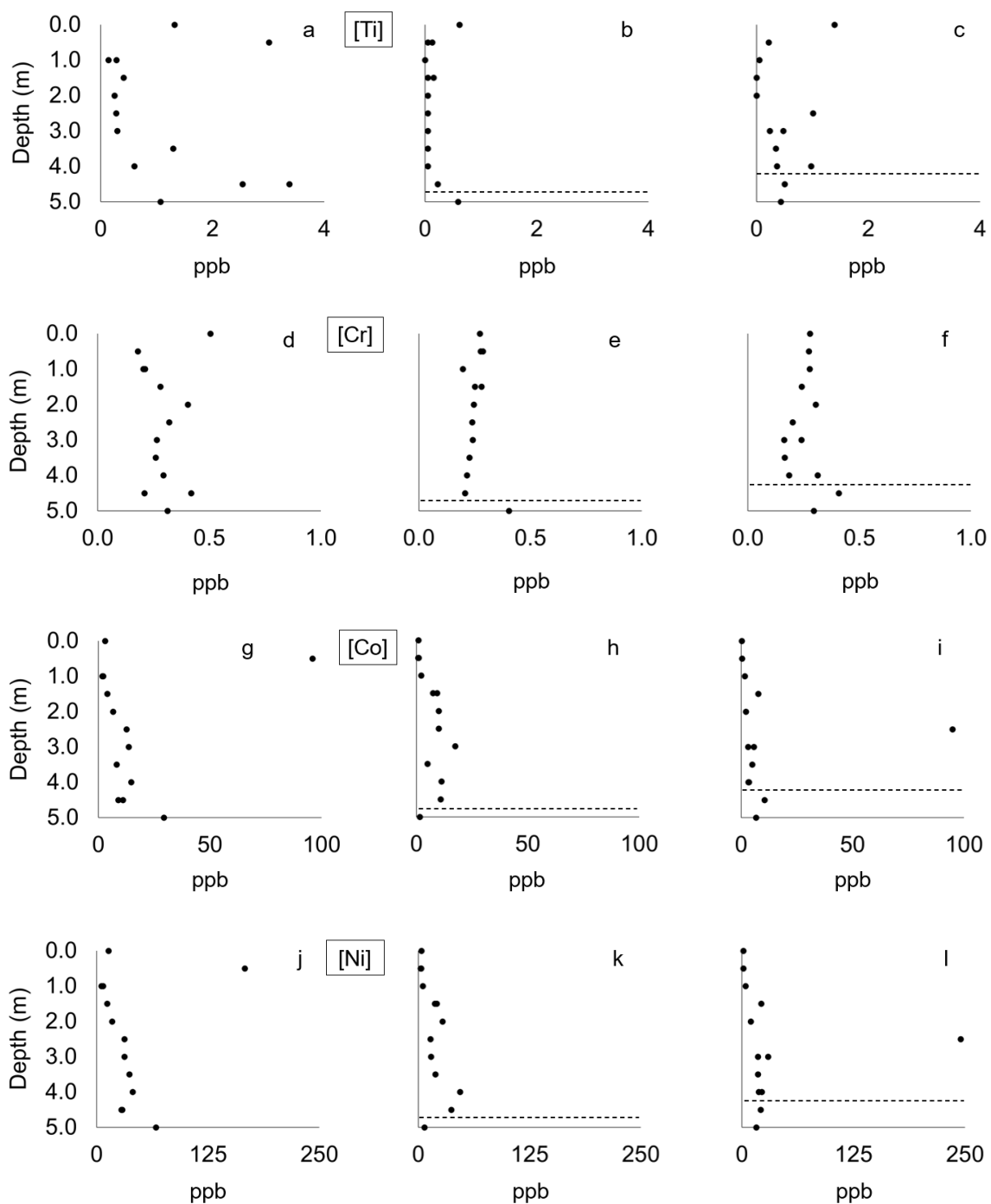


Figure 3.6: Aqueous-phase titanium (Ti), chromium (Cr), cobalt (Co), and nickel (Ni) depth plots for trench 1 (left), trench 2 (middle), and trench 3 (right).

The average aluminum (Al) concentrations were 4.9 ($\sigma = 5.2$), 2.0 ($\sigma = 1.4$), and 4.9 ($\sigma = 3.5$) ppb in trenches 1, 2, and 3, respectively (Fig. 3.7a - c). Average Al concentrations were highest in trench 3 and statistically lower in trench 2 by a mean difference of 3.4 ppb ($\alpha = 0.006$). No statistical relationship between Al concentration and depth was observed in any trench. Porewater chloride (Cl^-) concentrations averaged 23.1 ($\sigma = 16.2$), 10.1 ($\sigma = 2.6$), and 9.9 ($\sigma = 3.2$) ppm in trenches 1, 2, and 3, respectively (Fig. 3.7d - f). Average Cl concentrations were highest in trench 1 and statistically lower in trenches 2 and 3 by mean differences of 14.9 and 15.1 ppm ($\alpha = 0.03$ and 0.03). Chloride measurements did not reveal a statistically significant relationship with depth in any trench. The average phosphate (PO_4^{3-}) concentrations were 0.15 ($\sigma = 0.02$), 0.14 ($\sigma = 0.01$), and 0.15 ($\sigma = 0.04$) ppm for trenches 1, 2, and 3, respectively (Fig. 3.7g - i). Porewater PO_4^{3-} concentrations were relatively consistent between trenches and did not show a statistically significant relationship with depth.

In summary, SO_4^{2-} , Na, Mg, Fe, and Ti measured the lowest average concentrations in trench 2 and were consistently higher in trenches 1 and 3. Alkalinity and Ca measurements also reported the lowest average concentrations in trench 2 with statistically higher average alkalinity readings in trench 1 and higher Ca readings in trench 3. Concentrations of Na and K increased with depth in trench 3 and Cu, Zn, Pb, and Cd concentrations increased with depth in trench 2. Furthermore, all three trenches showed increasing concentrations of SO_4^{2-} and Ca with depth. Magnesium concentrations may also show some indication of increasing concentrations with depth in all three trenches; however, the relationship was not statistically significant ($R^2_{\text{calc}} = 0.50, 0.35, \text{ and } 0.51$ for trenches 1, 2, and 3, respectively). Likewise, Ni concentrations were observed to increase with depth in all three trenches but only when anomalous readings at 0.5 m depth in trench 1 and 2.5 m depth in trench 3 were excluded from the dataset ($R^2_{\text{calc}} = 0.68, 0.69, \text{ and } 0.63$ for trenches 1, 2, and 3, respectively). Alkalinity and pH recorded relatively low readings and Eh and Pb measurements were anomalously high at 0.5 m depth in trench 1 and Cu, Zn, Mn, Cd, Co, and Ni all

measured anomalously high concentrations at 0.5 m depth in trench 1 and 2.5 m depth in trench 3.

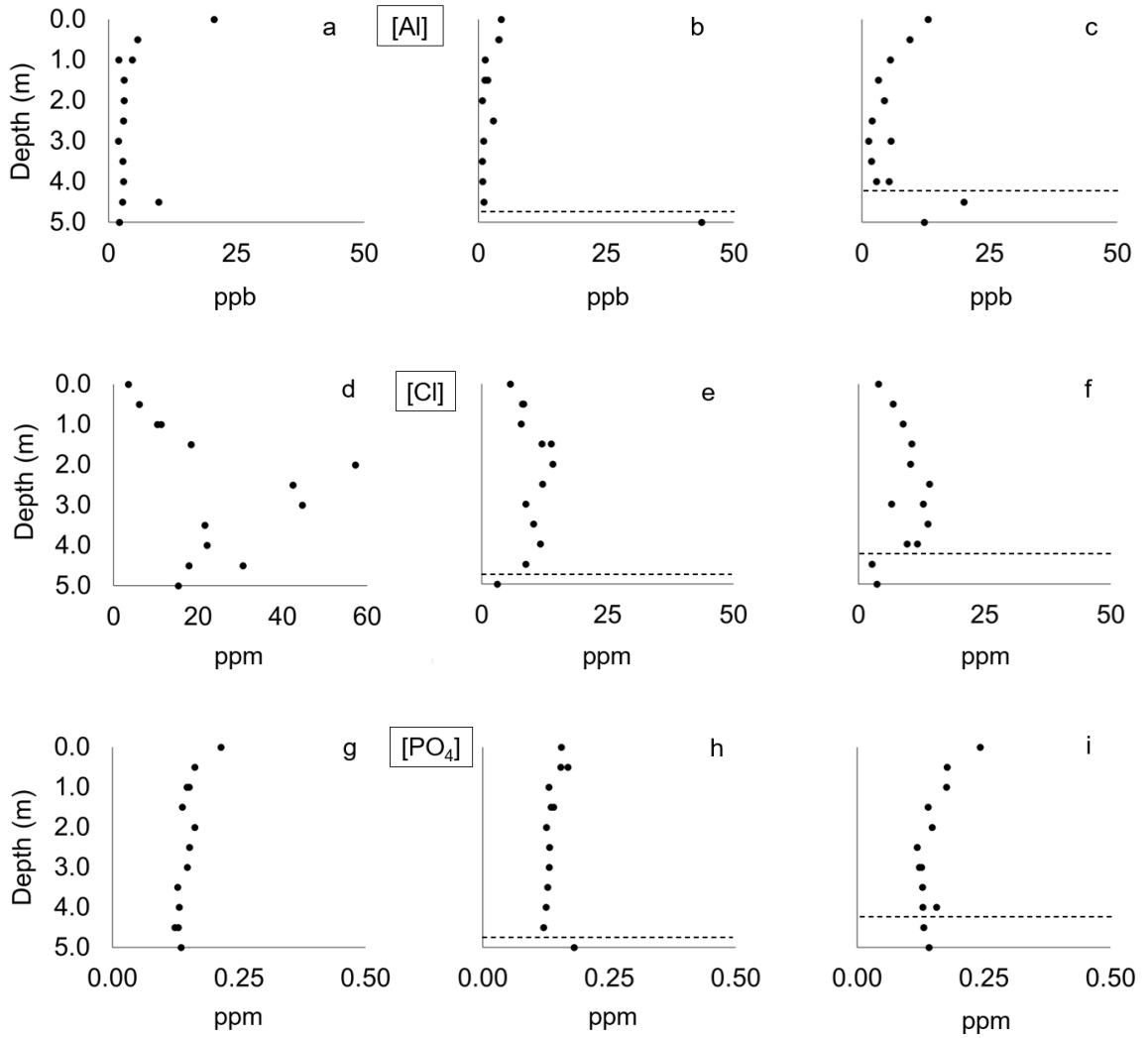


Figure 3.7: Aqueous-phase aluminum (Al), chloride (Cl⁻), and phosphate (PO₄³⁻) depth plots for trench 1 (left), trench 2 (middle), and trench 3 (right).

3.3.2 Mineral Saturation Indices

Calcite was typically undersaturated throughout the waste-rock pile with average SI values of -0.8 ($\sigma = 0.7$), -0.8 ($\sigma = 0.5$), and -0.4 ($\sigma = 0.7$) in trenches 1, 2, and 3, respectively (Fig. 3.8a - c). The lowest calcite SI measurements of -2.1 and -1.6 were observed at 0.5 and 4.0 m depth in trench 1. Porewaters were near saturation ($-0.5 \leq SI \leq +0.5$) with respect to calcite at 1.0 to 1.5 and 4.5 m in trench 1, from surface to 1.5 m in trench 2, and from surface to 0.5 and 3.0 to 4.0 m depth in trench 3. Dolomite was also frequently undersaturated with average SI values of -2.3 ($\sigma = 1.3$), -2.4 ($\sigma = 1.0$), and -1.4 ($\sigma = 1.5$) in trenches 1, 2, and 3, respectively (Fig. 3.8d - f). Similar to calcite, the lowest dolomite SI measurements of -4.9 and -3.9 were observed at 0.5 and 4.0 m depth in trench 1. Porewaters were near saturation with dolomite at 1.5 m in trench 1 and from surface to 0.5 and 3.0 to 4.0 m depth in trench 3.

Porewaters were undersaturated with gypsum above 1.5 m depth in all three trenches with average SI values of -0.8 ($\sigma = 0.4$), -1.3 ($\sigma = 0.2$), and -1.7 ($\sigma = 0.4$) in trenches 1, 2, and 3, respectively (Fig. 3.8g - i). Below (and including) 1.5 m, all three trenches approached saturation with average SI values of -0.3 ($\sigma = 0.2$), -0.5 ($\sigma = 0.2$), and -0.2 ($\sigma = 0.2$) in trenches 1, 2, and 3, respectively. Porewaters were undersaturated with jarosite throughout all three trenches with average SI values of -1.5 ($\sigma = 1.1$), -2.4 ($\sigma = 0.6$), and -1.4 ($\sigma = 1.5$) in trenches 1, 2, and 3, respectively (Fig. 3.8j - l). Jarosite only neared saturation at 0.5 and 4.0 to 4.5 m depth in trench 1. Saturation index values of jarosite shifted closer to equilibrium with depth in the waste-rock porewaters in all three trenches; however, remained undersaturated throughout the entire profile of trenches 2 and 3.

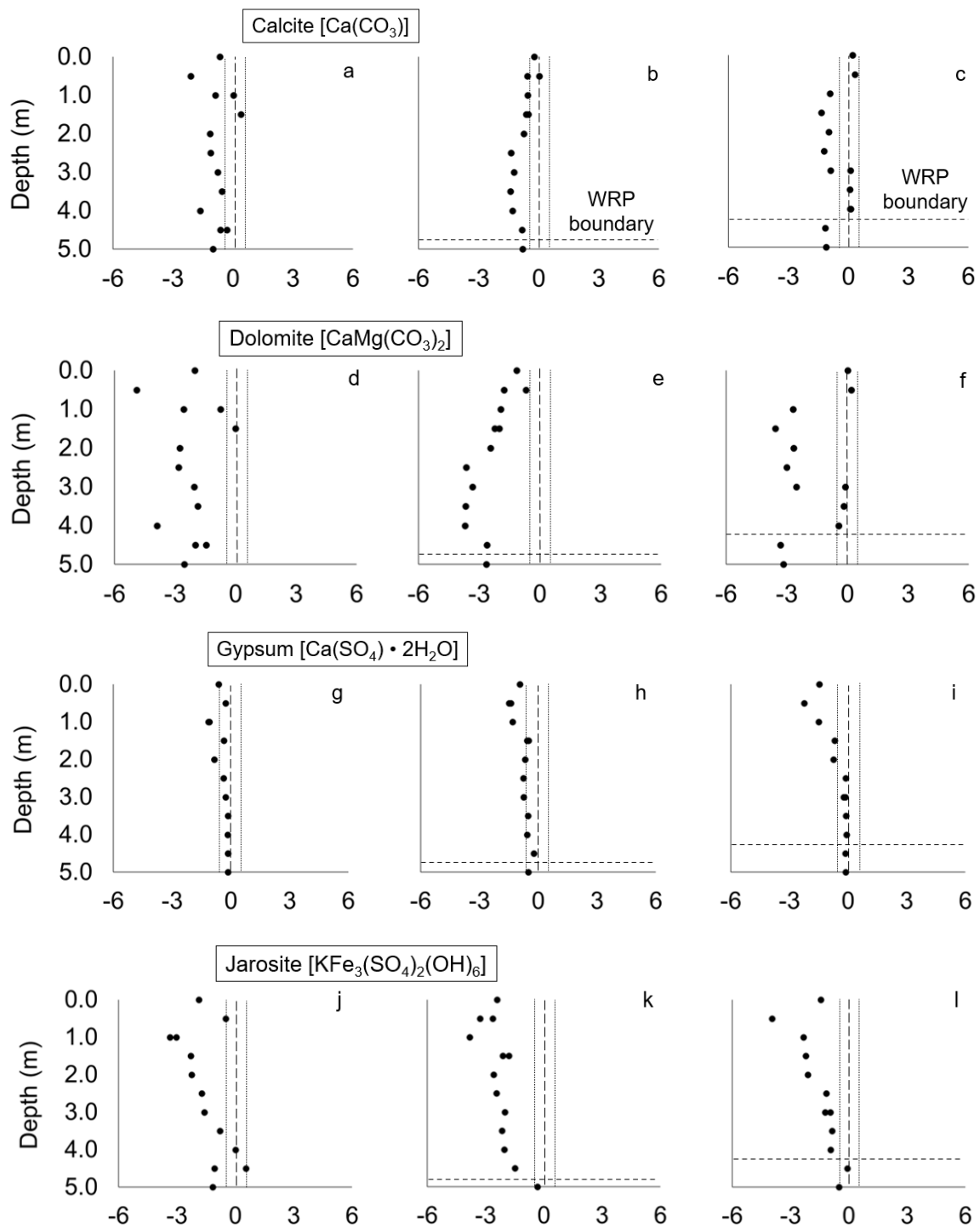


Figure 3.8: Calcite, dolomite, gypsum, and jarosite depth plot saturation indices for trench 1 (left), trench 2 (middle), and trench 3 (right). Dashed lines indicate SI boundary between -0.5 and +0.5.

Porewaters were consistently near saturation with respect to both gibbsite and boehmite in all three trenches ranging from -0.3 to 1.1 ($\mu = 0.2$, $\sigma = 0.3$) and from -0.8 to 0.6 ($\mu = -0.3$, $\sigma = 0.3$), respectively (Fig. 3.9a - f). Ferrihydrite was slightly oversaturated in all three trenches with average SI values of 1.1 ($\sigma = 0.4$), 1.1 ($\sigma = 0.4$), and 1.5 ($\sigma = 0.7$) in trenches 1, 2, and 3, respectively (Fig. 3.9g - i). Ferrihydrite was near saturation at 0.5 and 4.0 m in trench 1 and 2.5 and 3.5 m depth in trench 2 but remained slightly oversaturated throughout the entire depth profile of trench 3. Saturation index values of $\text{Cr}(\text{OH})_3$ (am) averaged -1.2 ($\sigma = 1.8$), -0.8 ($\sigma = 1.4$), and -0.7 ($\sigma = 0.5$) in trenches 1, 2, and 3, respectively and most samples were slightly undersaturated throughout each trench (Fig. 3.9j - l). However, waste-rock porewaters were near saturation with $\text{Cr}(\text{OH})_3$ (am) at the surface of the pile, 1.0, 3.5, and 4.5 m in trench 1, from 0.5 to 2.0 m in trench 2, and at 1.0 and 4.0 m depth in trench 3.

Manganite was frequently undersaturated throughout each trench with average SI values of -2.0 ($\sigma = 1.5$), -2.3 ($\sigma = 1.3$), and -2.1 ($\sigma = 0.9$) in trenches 1, 2, and 3, respectively (Fig. 3.10a - c). Porewaters were undersaturated with manganite throughout the entire depth profile of trench 3 and neared saturation at 1.5 m depth in trench 1 and at the surface of trench 2. Porewaters were almost always near saturation with respect to $\text{Mn}(\text{HPO}_4)$ with average SI values of 0.4 ($\sigma = 0.4$), 0.1 ($\sigma = 0.3$), and -0.3 ($\sigma = 0.7$) in trenches 1, 2, and 3, respectively (Fig. 3.10d - f). Except for an oversaturated SI reading of 1.5 at 2.5 m depth in trench 3, $\text{Mn}(\text{HPO}_4)$ showed only minor variation in SI values and was especially consistent in trenches 1 and 2.

Malachite was either near saturation or undersaturated throughout the waste-rock pile with average SI values of -1.0 ($\sigma = 0.8$), -0.4 ($\sigma = 0.5$), and -0.5 ($\sigma = 0.7$) in trenches 1, 2, and 3, respectively (Fig. 3.10g - i). Porewaters were near saturation with malachite most consistently in trench 2 and only reported undersaturated SI values of -1.1 and -1.6 at 2.5 and 3.5 m depth. Malachite was also observed to be near saturation at 1.0 to 1.5 and 3.0 m in trench 1 and from the surface to 0.5 and from 2.5 to 4.0 m depth in trench 3. Porewaters were almost always near saturation

with otavite with average SI values of -0.6 ($\sigma = 0.5$), -0.3 ($\sigma = 0.3$), and -0.4 ($\sigma = 0.3$) in trenches 1, 2, and 3, respectively (Fig. 3.10j - l). Trench 1 yielded the greatest SI variability with observed values of -1.4 and -1.4 at 0.5 and 4.0 m depth; however, the variation in otavite SI values was relatively minor, especially in trenches 2 and 3.

Cerussite was either near saturation or undersaturated in the porewaters with average SI values of -0.7 ($\sigma = 0.3$), -0.5 ($\sigma = 0.2$), and -0.6 ($\sigma = 0.3$) in trenches 1, 2, and 3, respectively (Fig. 3.11a - c). Cerussite was near saturation from 1.0 to 1.5 and 3.0 m in trench 1, from the surface to 2.0 m in trench 2, and from the surface to 1.0 and from 3.0 to 4.0 m depth in trench 3. However, remaining locations were observed to only be slightly undersaturated with cerussite and SI values were relatively consistent throughout all three trenches. Porewaters were typically undersaturated with respect to $\text{Pb}(\text{OH})_2$ with average SI values of -1.6 ($\sigma = 0.7$), -1.2 ($\sigma = 0.5$), and -1.2 ($\sigma = 0.6$) in trenches 1, 2, and 3, respectively (Fig. 3.11d - f). The higher relative standard deviation in trench 1 corresponds to the lowest overall SI value of -3.1 at 4.0 m depth. Porewaters were undersaturated with $\text{Pb}(\text{OH})_2$ throughout the entire depth profile of trench 2 and neared saturation from 1.0 to 1.5 m in trench 1 and at 0.5 m depth in trench 2.

Smithsonite monohydrate was either near saturation or slightly undersaturated with average SI values of -0.6 ($\sigma = 0.4$), -0.4 ($\sigma = 0.3$), and -0.5 ($\sigma = 0.5$) in trenches 1, 2, and 3, respectively (Fig. 3.11g - i). Smithsonite monohydrate was typically undersaturated from the surface to 1.0 m depth in all three trenches with an average SI value of -0.9 and neared saturation beyond 1.0 m with an average SI value of -0.4. Porewaters were typically undersaturated with respect to $\text{Zn}(\text{OH})_2$ throughout all three trenches with averages of -1.4 ($\sigma = 0.7$), -1.1 ($\sigma = 0.6$), and -1.1 ($\sigma = 0.6$) in trenches 1, 2, and 3, respectively (Fig. 3.11j - l). The lowest $\text{Zn}(\text{OH})_2$ SI measurement of -3.0 was observed at 4.0 m depth in trench 1 accounting for the higher relative standard deviation. Furthermore, $\text{Zn}(\text{OH})_2$ was observed to approach saturation with depth in trench 3. Porewaters were also near

saturation with $\text{Zn}(\text{OH})_2$ from 1.0 to 1.5 m in trench 1 and 0.5 and from 1.5 to 2.0 m depth in trench 2.

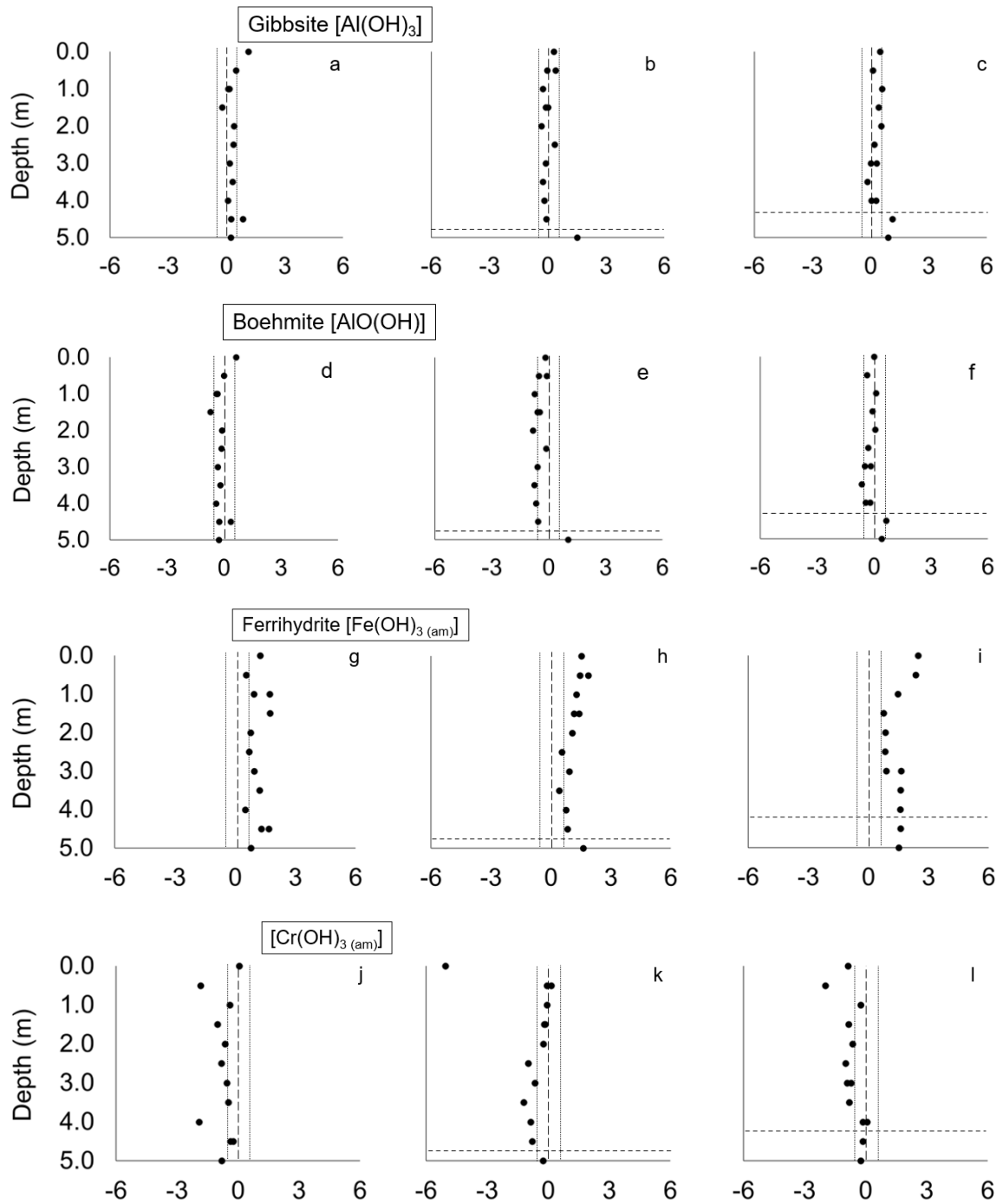


Figure 3.9: Gibbsite, boehmite, ferrihydrate, and $\text{Cr}(\text{OH})_{3(\text{am})}$ depth plot saturation indices for trench 1 (left), trench 2 (middle), and trench 3 (right).

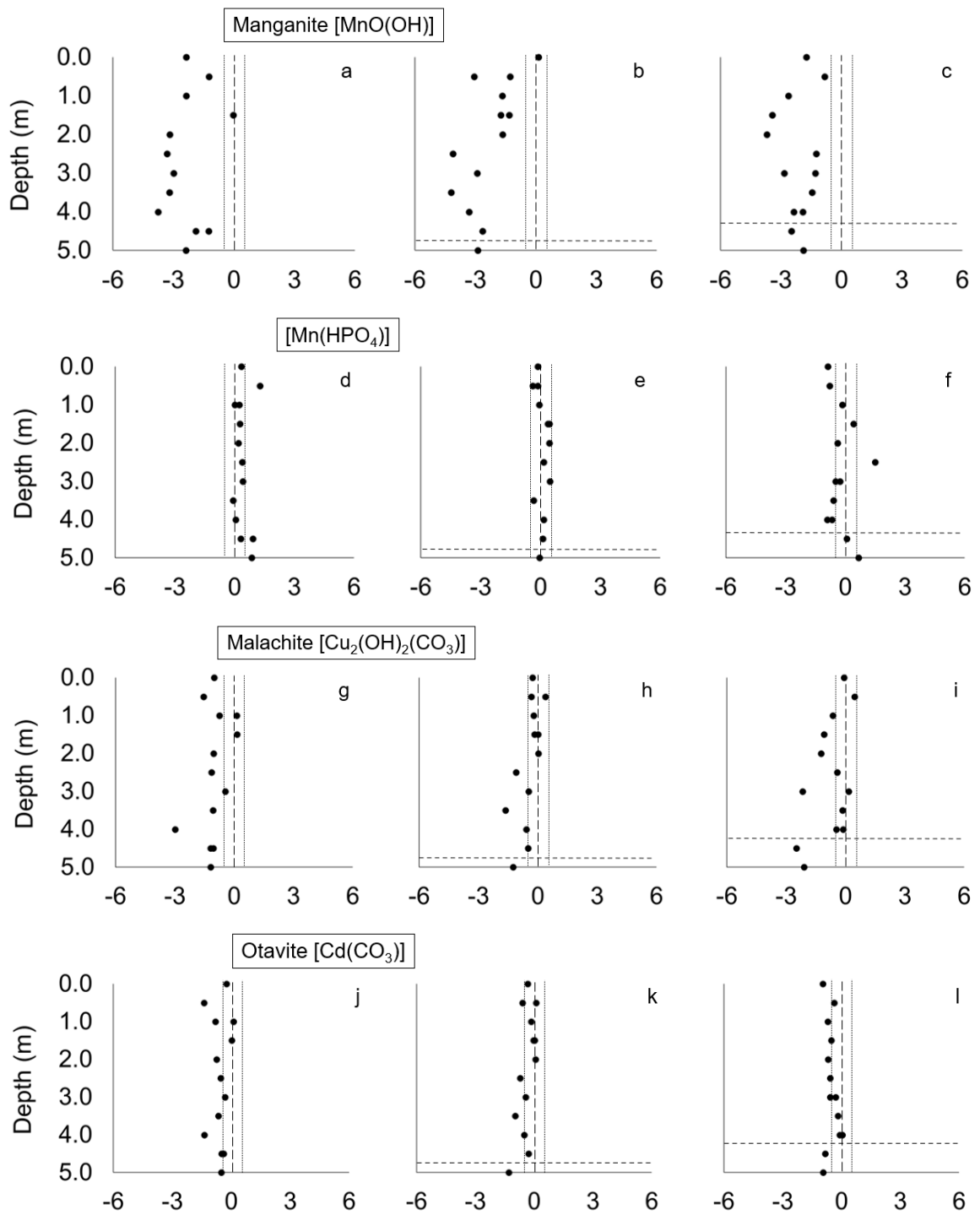


Figure 3.10: Manganite, $\text{Mn}(\text{HPO}_4)$, malachite, and otavite depth plot saturation indices for trench 1 (left), trench 2 (middle), and trench 3 (right).

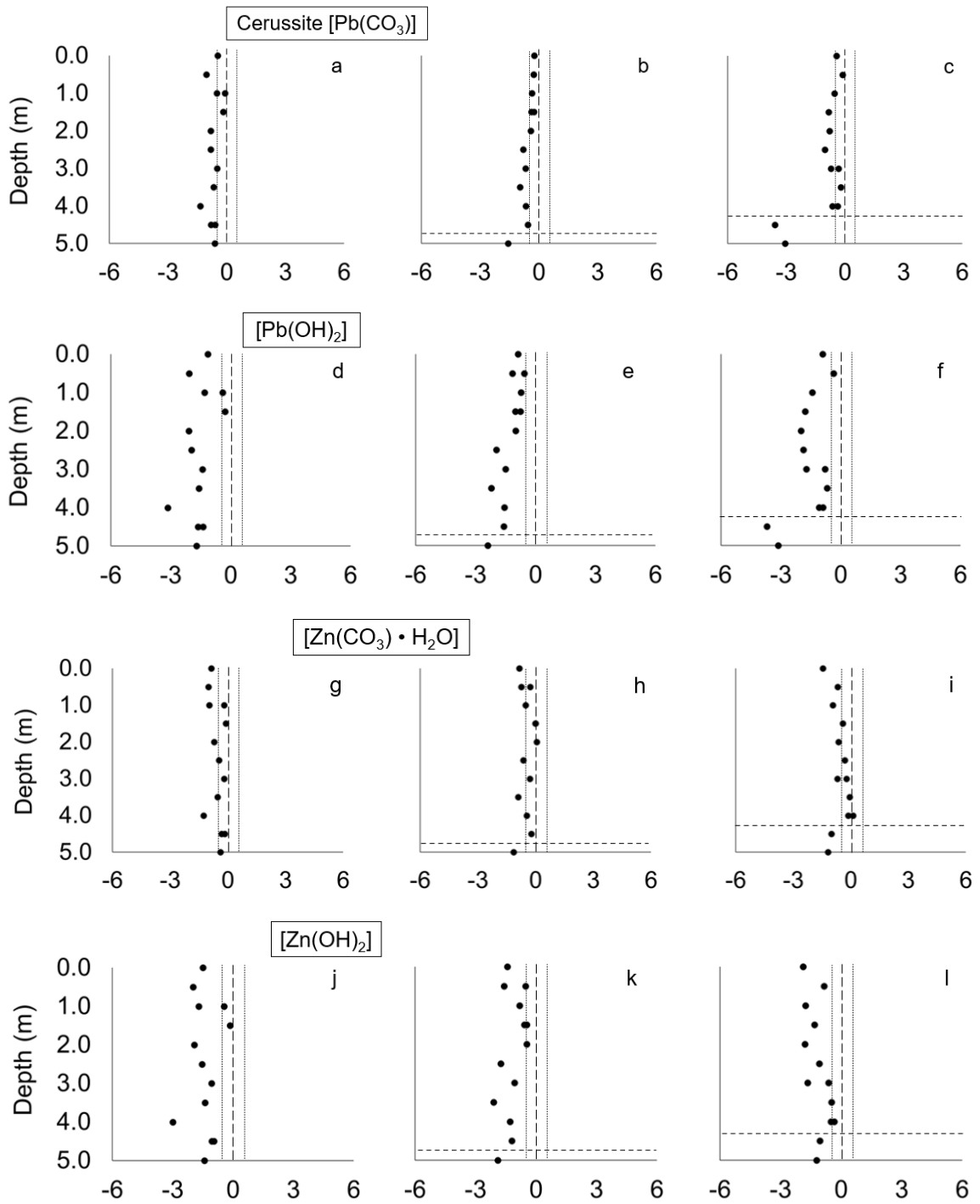


Figure 3.11: Cerussite, $Pb(OH)_2$, smithsonite monohydrate, and $Zn(OH)_2$ depth plot saturation indices for trench 1 (left), trench 2 (middle), and trench 3 (right).

In summary, gypsum, jarosite and smithsonite monohydrate were the only minerals that were undersaturated towards the surface and approached saturation with depth in all three trenches. Otavite, cerussite, and $Zn(OH)_2$ were also observed to approach saturation with depth, but only in trench 3. Calcite, dolomite, gypsum, and jarosite all showed lower relative average SI readings in trench 2. Furthermore, calcite, dolomite, otavite, and cerussite (carbonate-bearing) all recorded the lowest relative SI readings at 0.5 and 4.0 m depth in trench 1. The mineral phases that were near or slightly above saturation for at least ten porewater samples between all three trenches included calcite, gypsum, gibbsite, boehmite, ferrihydrite, $Cr(OH)_3$ (am), $Mn(HPO_4)$, malachite, otavite, cerussite, and smithsonite monohydrate.

3.4 Discussion

3.4.1 Porewater Chemistry and Secondary Controls

Porewater pH at the Ore Chimney waste-rock pile was near-neutral (6.4 to 8.4) and showed minor variability throughout all three trenches. Alkalinity concentrations always exceeded 25 mg/L $CaCO_3$ except for a 13 mg/L measurement at 0.5 m depth in trench 1, which correlated with lower pH (6.4), lower total inorganic carbon content measured by total C/S analysis, and reduced calcite and dolomite concentrations predicted by PXRD (Ch. 2). Calcite and dolomite SI values were near saturation in many locations and are therefore the likely sources of alkalinity, Ca, and Mg in the porewaters. Calcite and dolomite typically buffer acidity to a pH range of 6.2 to 8.3 (Parbhakar-Fox and Lottermoser, 2017) and are likely controlling the near-neutral pH levels observed throughout the entire waste-rock pile even after ~100 years of weathering above ground surface.

Measurements of bisulfide (HS^-) and ferrous iron (Fe^{2+}) were consistently under range indicating that oxidizing conditions likely prevail throughout the entire depth profile of the waste-rock pile. Sulfate was observed as the dominant anion with concentrations ranging from 31 to 2,023 ppm and average molar concentrations accounting for 84% of the total anion concentration including bicarbonate [HCO_3^-].

Elevated SO_4^{2-} concentrations observed in the porewaters are indicative of sulfide oxidation processes (Blowes et al., 2013). Likewise, porewater Eh measurements ranged from (+341) to (+547) mV corroborating observations of a strongly oxidizing system, which is required for sulfide mineral oxidation (Langmuir, 1997). Measurements of Eh did not significantly change with depth, which coincides with petrographic observations of consistent sulfide mineral weathering throughout the entire depth profile of the waste-rock pile (Ch. 2). Consistencies with elevated porewater Eh measurements and apparent sulfide mineral oxidation throughout the entirety of each trench suggests that atmospheric oxygen has infiltrated the entire waste-rock pile and is the main oxidizing agent irrespective of depth (Amos et al., 2015).

Moncur et al (2005) measured porewater chemistry from the surface to 4.0 m depth of the Sheritt-Gordon tailings profile in Manitoba, Canada, to investigate mineral alteration and metal transport after 70 years of subaerial weathering. Observations indicated the formation of a 1.5 m thick hardpan layer primarily composed of consolidated secondary mineral phases including melanterite ($\text{Fe}^{2+}\text{SO}_4 \cdot 7\text{H}_2\text{O}$), rozenite ($\text{Fe}^{2+}\text{SO}_4 \cdot 4\text{H}_2\text{O}$), goethite [$\text{Fe}^{3+}\text{O}(\text{OH})$], gypsum ($\text{CaSO}_4 \cdot 2\text{H}_2\text{O}$), and jarosite [$\text{KFe}^{3+}_3(\text{SO}_4)_2(\text{OH})_6$]. The hardpan layer was observed to limit oxygen infiltration, which was indicated by a sharp decline in Eh readings from +802 mV at the surface (0.0 m) to +300 mV at approximately 1 m depth (Moncur et al., 2005). The particle size composition of tailings and subsequent moisture retention properties are usually similar to ordinary silts and clays (Qiu and Segó, 2001), which are finer-grained, less permeable, and have a greater resistance to the ingress of oxygen than coarser-grained material that typically represents waste rock (Gorakhki and Bareither, 2017; Azam et al., 2020).

Tailings material often contains higher concentrations of sulfur than waste rock (Goumih et al., 2013). The accelerated weathering of finer-grained tailings material has the potential to establish a pH and redox gradient showing elevated acidity and Eh readings near the surface that significantly reduce beyond 1 m depth even after 70 years of weathering (Moncur et al., 2005; Moncur et al., 2009). Porewater

pH and Eh depth profiles from coarser grained waste-rock material at Ore Chimney did not reveal the development of a gradient nor the formation of a hardpan layer and maintained relatively consistent pH and Eh readings from the surface to 5.0 m depth. However, the formation of a hardpan layer observed by Moncur et al (2005) did not completely restrict the vertical movement of water as indicated by the accumulation of SO_4^{2-} in the porewaters at greater depth. Ore Chimney also revealed sulfate accumulation with depth but is likely due to transport processes plus additional oxidation at depth.

Calcium was observed as the dominant cation in the porewaters accounting for an average of 59% of the total (molar) cation concentration measured by ICP-AES/MS. Furthermore, Ca concentrations, in addition to SO_4^{2-} , significantly increased with depth suggesting that Ca and SO_4^{2-} were being leached from upper portions of the waste-rock pile and accumulating towards the base (Shum and Lavkulich, 1999). The average solid-phase sulfur concentration above 2.0 m depth in the Ore Chimney waste-rock pile is 1.6 wt.% ($\sigma = 0.9$) and sulfide alteration extent did not significantly change with depth (Ch. 2) suggesting that mineral weathering is ongoing and gravity-assisted vertical transport through the pile is elevating Ca and SO_4^{2-} in the porewaters at greater depth. Although grain size distributions and the vertical flow velocity of water through the waste-rock pile at Ore Chimney was not determined, other unsaturated waste-rock piles have observed thawing periods that permeate water at an average rate on the order of 2 to 3 cm/day (Zak, 2013).

Smith et al (2013b) observed SO_4^{2-} and Ca accumulation from waste-rock effluent at a test pile at the Diavik mine that plateaued at 2,000 and 350 ppm, respectively, after only four months of subaerial weathering. Similar to Diavik, elevated SO_4^{2-} (2,000 ppm) and Ca (400 ppm) concentrations near the base of the Ore Chimney waste-rock pile suggest that Ca and SO_4^{2-} concentrations are controlled primarily by the formation of gypsum, which was maintained near saturation at Ore Chimney below (and including) 1.5 m depth and is consistent with carbonate-bearing waste-rock weathering studies at both four-month (Smith et al., 2013b) and 30-year

(Smith et al., 2021) time scales. The Ca and SO_4^{2-} signatures at Ore Chimney are likely not a function of long-term weathering processes but rather an indication that Ca and SO_4^{2-} are mobile, and concentrations are being controlled to a similar extent even after ~100 years of sulfide oxidation (Smith et al., 2013b; Moncur et al., 2015).

Calcium is typically released into porewaters from Ca-bearing carbonate minerals that dissolve into solution from neutralization reactions buffering acidity that is generated from the oxidation of sulfide minerals (Blowes et al., 2013; Amos et al., 2015). Sulfide mineral oxidation and PXRD measurements of calcite and dolomite phases (Ch. 2) coupled with observations of near-neutral pH and instances of calcite and dolomite phases near saturation provides a strong indication that carbonate mineral dissolution has been an active process within the waste rock at Ore Chimney over the past ~100 years. The dissolution of dolomite from pH buffering can strongly influence dissolved Mg concentrations in mine wastes (Jurjovec et al., 2002). Magnesium concentrations exhibited a strong positive relationship with Ca measuring R^2_{calc} values of 0.63, 0.73, and 0.66 in trenches 1, 2, and 3, respectively (Fig. 3.12a - c), which suggests that dolomite and calcite are both being weathered in the system. However, calcite dissolution neutralizes acidity at a higher rate than dolomite by one order of magnitude (Lapakko, 2002) and porewater Mg concentrations were observed to be at least twofold lower than Ca suggesting that calcite has been the primary carbonate buffering phase at Ore Chimney.

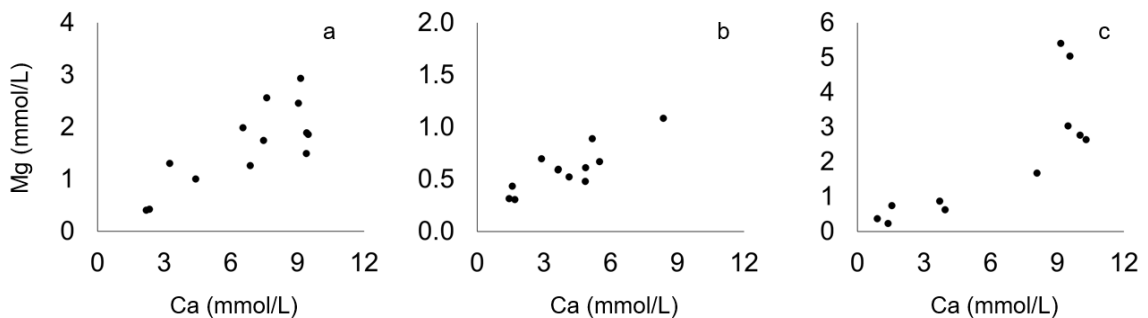


Figure 3.12: Ca correlation plot with Mg for trench 1 (left), trench 2 (middle), and trench 3 (right).

Magnesium-bearing mineral phases identified by PXRD included hornblende, biotite, chlorite, and dolomite (Ch. 2). Porewater Mg concentrations were statistically higher in trench 1 than trench 2 by a mean difference of 25.8 ppm; however, Mg-bearing mineral content was relatively consistent. Alternatively, average calcite concentrations from both grain fractions in trench 1 were 50% higher than trench 2 (Ch. 2). Calcite often hosts trace concentrations of Mg in its mineral structure (Lane and Dalton, 1994; Zaitsev and Polezhaeva, 1994) and SEM analysis of calcite at Ore Chimney revealed up to 2 wt.% Mg (Ch. 2). Furthermore, calcite dissolution is typically favoured over dolomite in weathering systems (Lapakko, 2002; White et al., 2005) thereby suggesting that calcite may also be contributing to dissolved Mg in the porewaters.

Relative to trenches 1 and 2, PXRD measured under range calcite content ($\mu = 1.4$ wt.%) and the highest dolomite concentrations ($\mu = 5.8$ wt.%) in trench 3 (Ch. 2). Likewise, elevated porewater Mg concentrations towards the base of trench 3 correspond to low calcite content (below detection) and a significantly higher proportion of dolomite from 3.0 to 4.0 m depth suggesting that dolomite may have begun to replace calcite as the principal carbonate buffering phase in this locality. Moreover, dolomite was observed to be near saturation from 3.0 to 4.0 m depth in trench 3 and may act as the primary control for elevated Mg in the porewaters. The lower average calcite content and subsequently higher concentrations of dissolved Ca in the porewaters may indicate that calcite has depleted to a greater extent than dolomite but remains in the waste-rock pile after ~100 years of weathering. Should the remaining portion of calcite continue to react with acidity from oxidizing sulfide minerals, it is proposed that dolomite will eventually transition into the primary carbonate buffering mineral and the relatively high dolomite concentrations measured from both grain size fractions throughout each trench ($\mu_{\text{pile}} = 4.1$ wt.%) should maintain near-neutral pH as the pile continues to weather (Parbhakar-Fox and Lottermoser, 2017).

Dissolved concentrations of Fe, Mg, and K are often derived from the subaerial weathering of biotite (Strömberg and Banwart, 1999; Moncur et al., 2009).

Furthermore, biotite typically weathers at a faster rate than most silicate minerals due to its layered structure and the incorporation of ferrous iron that is reactive with oxygen (Fordham, 1990; Bhatti et al., 2011). Monovalent cations, typically as potassium, are present between the biotite sheet structures and are released into porewaters approximately two orders of magnitude higher than Mg and Fe^{2+} , which are more tightly bound within the internal layers of the mineral lattice (Malmstrom and Banwart, 1997). Therefore, biotite is likely subsidiary to carbonate minerals as a source for dissolved Mg but the principal source for the observed K concentrations in the porewaters (Langman et al., 2014).

The biotite mineral phase identified by PXRD was predicted to host trace concentrations of Na, which would substitute for weakly bonded K ions and be released into solution at a similar rate (Ch. 2) (Malmstrom and Banwart, 1997). Sodium-bearing plagioclase feldspar (oligoclase) and hornblende are more resistant to weathering than biotite but are still predicted to dissolve into solution at near-neutral pH at very slow rates (Stillings et al., 1996; Frogner and Schweda, 1998). Therefore, dissolved Na concentrations observed at Ore Chimney may originate from biotite, oligoclase, and hornblende and indicates that aluminosilicate weathering is occurring to some extent. There were no controls observed for porewater Na; however, dissolved concentrations of K, and to a lesser extent SO_4^{2-} and Fe, may be controlled by the formation of jarosite at 0.5 and 4.0 m depth in trench 1, which favours acidic conditions and corresponds to the lowest relative pH readings of 6.5 and 6.4 (Elwood Madden et al., 2012; Blowes et al., 2013).

Under-range measurements of Fe^{2+} by spectrophotometry coupled with under range HS^- and elevated Eh and SO_4^{2-} readings provides a strong indication that porewater ICP-MS Fe measurements predominantly consisted of ferric iron (Fe^{3+}). Ferric iron content in the porewaters was relatively consistent with depth and is likely being controlled by the precipitation of ferrihydrite, which may play a significant role in masking Fe correlations with other dissolved metals (Nordstrom, 1982). Ferrous iron-bearing mineral phases such as siderite ($\text{Fe}^{2+}\text{CO}_3$), melanterite, and rozenite, have been observed to control porewater Fe

concentrations in some mine-waste systems (Moncur et al., 2005; Moncur et al., 2009) but correspond to lower Eh/pH conditions than what was observed herein and are not considered to limit Fe porewater concentrations at Ore Chimney. Ferrihydrite precipitation is favoured under circumneutral pH (Blowes et al., 2013) and was slightly oversaturated; thus, potentially controlling Fe in the porewaters. Investigations along the alteration rims of Fe-bearing sulfides by SEM-EDX revealed an Fe-oxyhydroxide phase that most likely resembled goethite (Ch. 2), which was predicted to be more saturated than ferrihydrite in the porewaters. Goethite has been observed as a more stable Fe-oxyhydroxide phase that is transformed from ferrihydrite over time (Combes et al., 1989) and is likely the long-term mechanism that is controlling the rates of pyrite and chalcopyrite oxidation and the low ppb-level porewater Fe concentrations at Ore Chimney (Moncur et al., 2009).

Measurable concentrations of Zn, Cu, and Pb in the porewaters indicate that sphalerite, chalcopyrite, and galena are being weathered throughout the waste-rock pile. Analysis of Fe-oxyhydroxide weathering phases of Fe-bearing sulfide alteration rims by SEM-EDX also detected Zn and Cu concentrations up to 5 wt.% and Pb concentrations as high as 10 wt.% (Ch. 2). The adsorption capacity of Zn, Cu, and Pb onto goethite significantly increases at pH values greater than 5, and the near-neutral pH levels measured at Ore Chimney suggest that Fe-oxyhydroxide alteration phases may be retaining portions of Zn, Cu, and Pb from the porewaters through adsorption processes (Kooner, 1993; Rodda et al., 1993). However, dissolved Zn, Cu, and Pb were all observed to increase with depth suggesting that despite co-precipitation/adsorption processes, these metals are still being transported through the waste-rock pile.

On average, porewater Zn content measured via ICP-AES accounted for 92% of total metalloid, transition, and post-transition metal (molar) concentrations. Elevated concentrations of Zn may be attributed to high relative abundance and prolonged subaerial weathering of sphalerite (Moncur et al., 2009). Carbonate mineral dissolution often occurs in tandem with sulfide mineral oxidation (Blowes

et al., 2013) and the weathering of sphalerite under the presence of calcite is expected to simultaneously elevate dissolved Zn, SO_4^{2-} , and possibly Ca in the porewaters (Fig. 3.13a - f). However, once Zn concentrations exceeded approximately 0.5 mmol/L, both SO_4^{2-} and Ca concentrations were observed to plateau at around 16 and 10 mmol/L, respectively, indicating that they were likely being controlled by the formation of gypsum (Jurjovec et al., 2002).

The porewater alkalinity was high enough at Ore Chimney for pH levels to always remain above 6.4; however, elevated Zn concentrations were observed to correspond with lower pH readings (Fig. 3.13g - i). Among all metals, Zn concentrations exhibited the strongest positive correlation with Cd with R^2_{calc} values of 0.86, 0.94, and 0.96 for trenches 1, 2, and 3, respectively (Fig. 3.13j - l). The presence of solid-phase Cd was measured exclusively in sphalerite grains as high as 2 wt.% (Ch. 2) and the average molar Cd concentration in the porewaters was approximately tenfold and thirtyfold higher than Pb and Cu, respectively, which may be due to the fact that the secondary controls for Zn and Cd [i.e. smithsonite monohydrate ($K_{\text{sp}}: 10^{-10.3}$) and otavite ($K_{\text{sp}}: 10^{-12.1}$)] have higher solubilities than cerussite ($K_{\text{sp}}: 10^{-13.1}$) and malachite ($K_{\text{sp}}: 10^{-33.2}$), and sphalerite may be more susceptible to mineral weathering than galena and chalcopyrite (Parkhurst and Appelo, 1999). Cadmium was not detected as a component of secondary Fe-oxyhydroxides, which may be because the available sorption sites are entirely occupied by Pb, Zn, and Cu. Likewise, Cd has a lower relative adsorption affinity onto goethite, which may enhance Cd mobility under these conditions (Swedlund et al., 2009; Mohapatra et al., 2011; Komárek et al., 2018).

SEM-EDX analysis along sphalerite alteration rims occasionally detected the presence of a zinc carbonate phase (Ch. 2), which coincides with the relatively high carbonate content and subsequent porewater alkalinity. These findings are consistent with Zn porewater concentrations nearing saturation with smithsonite monohydrate beyond 1.0 m depth in all three trenches. Anhydrous zinc carbonate (i.e. pure smithsonite) was slightly less saturated than its hydrated counterpart by a mean difference of 0.4 ($\sigma = 0$). Therefore, it is likely that Zn first precipitates as

a hydrous zinc carbonate phase and recrystallizes into a more stable anhydrous product over time and “smithsonite” can be generalized as the main Zn control in the porewaters (Bain et al., 2001). Cadmium was not detected as a component of any secondary mineral phase along sphalerite alteration rims; however, otavite (CdCO_3) was predicted to be consistently near saturation potentially controlling porewater Cd throughout the waste-rock pile, which is typical for carbonate and sphalerite-rich systems (Eary, 1999; Bain et al., 2001; Laurenzi et al., 2015).

Among the sulfide minerals, solid-phase Co concentrations were only detected in pyrite grains and Ni concentrations were measured exclusively in both pyrite and sphalerite grains via SEM-EDX. Although they often measured below the SEM-EDX detection limit, ICP-AES/MS analyses accurately measured concentrations of these elements in the solid phase. Moreover, molar concentrations of Co and Ni were found to be at least twofold higher than Fe in the porewaters despite measuring thousandfold lower concentrations from solid-phase ICP-MS and measuring below detection (< 1 wt.%) in pyrite grains (Ch. 2). Therefore, Fe concentrations in the porewaters were likely being restricted by the formation of ferrihydrite whereas no secondary controls were observed for Co or Ni. SEM-EDX analysis on pyrite alteration zones did not detect Co nor Ni (Ch. 2) suggesting that they are not well retained within the structure of secondary ferric oxyhydroxides and may have a higher relative affinity than Fe to be released into the porewaters from long-term subaerial exposure under neutral pH (Lehner et al., 2007). Furthermore, the absence of Co and Ni on Fe-oxyhydroxide alteration phases indicates no attenuation via surface complexation reactions, which is consistent with Rose and Bianchi-Mosquera (1993) who observed lower adsorption affinities of Co and Ni onto goethite than Pb, Zn, and Cu at near-neutral pH. Therefore, it is suggested that accelerated incipient weathering of sphalerite and galena compared to pyrite enriches porewaters with Zn and Pb that preferentially occupy available sorption sites on Fe-oxyhydroxides. Consequently, Co and Ni attenuation is restricted and their mobilities are increased, which coincided with increasing porewater concentrations with depth in trenches 1 and 2 and the suspected relative

adsorption affinities of Co and Ni are similar to observations made by Blowes and Jambor (1990) and Jurjovec et al. (2002).

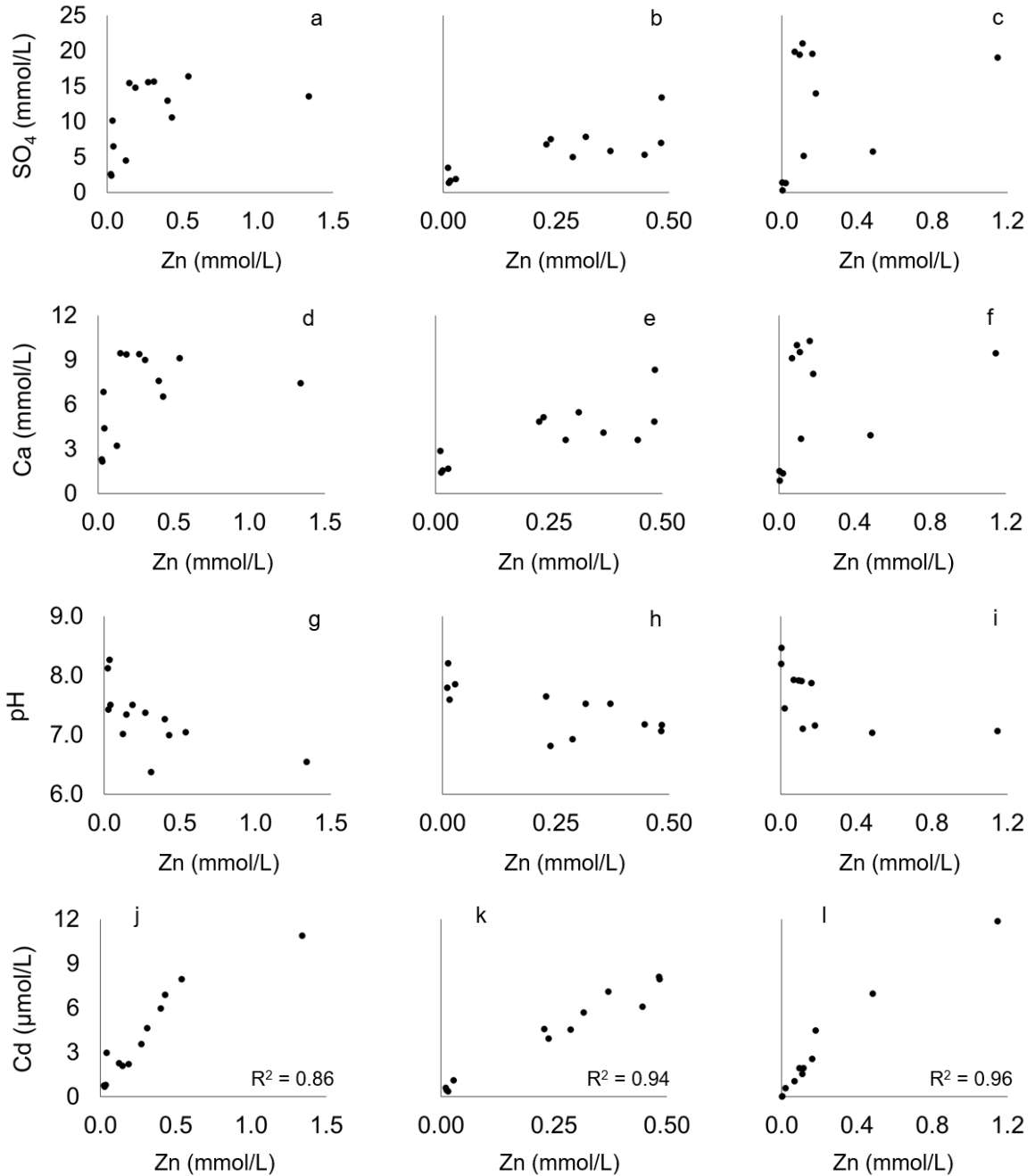


Figure 3.13: Zn correlation plots with SO₄²⁻, Ca (mmol/L), pH, and Cd (µmol/L) for trench 1 (left), trench 2 (middle), and trench 3 (right).

The strong positive correlations between Zn with Pb, Cu, Co, and Ni indicates ongoing simultaneous sphalerite, galena, chalcopyrite, and pyrite weathering (Fig. 3.14a - l). Relatively abundant carbonate content and subsequently high alkalinity suggests porewater concentrations of Pb and Cu are controlled by the formation of cerussite and malachite, respectively, throughout most of the waste-rock pile and is consistent with SEM-EDX measurements of cerussite along the alteration rims of galena grains (Ch. 2). Undersaturated cerussite SI values of -1.0 (0.5 m) and -1.4 (4.0 m depth) in trench 1 corresponded to lower pH readings of 6.4 and 6.5, respectively, which also applied to calcite, dolomite, malachite, otavite, and smithsonite. Likewise, the highest porewater pH readings of 8.3 at 1.5 m in trench 1 and 8.4 at 0.5 m depth in trench 3 indicated near saturation with $\text{Pb}(\text{OH})_{2(s)}$ and $\text{Zn}(\text{OH})_{2(s)}$ and may also control dissolved Pb and Zn concentrations but to a lesser extent than cerussite and smithsonite.

Anomalously high porewater concentrations of Zn, Cd, Pb, Cu, Co, and Ni measured at 0.5 m in trench 1 and 2.5 m depth in trench 3 were not observed to coincide with elevated metal concentrations from solid-phase ICP-MS/AES nor elevated sulfur content from total C/S analysis suggesting that the porewater chemistry was not directly proportional to the in situ solid-phase sulfide content presented in Chapter 2. Elevated signatures may be influenced by the presence of colloidal material (Aiken et al., 2011); However, porewater signatures of Zn, Cd, Pb, Cu, Co, and Ni at 0.5 m in trench 1 and 2.5 m depth in trench 3 corresponded with low alkalinity. Metal-carbonate complexes were the strongest/only secondary controls predicted for Zn, Cd, Pb, and Cu and undersaturated SI values corresponded with insufficient alkalinity concentrations. Therefore, elevated Zn, Cd, Pb, and Cu at 0.5 m in trench 1 and 2.5 m depth in trench 3 are likely due to the absence of a secondary (carbonate) control due to decreased alkalinity, which was attributed to relatively low solid-phase inorganic carbon content (Ch. 2). In addition, the subsamples for porewater analyses in the abovementioned localities may have represented finer-grained waste-rock material where accelerated sulfide oxidation further depleted the alkalinity supply. The magnitude of porewater metal concentrations may depend on both mineralogy and grain size thus outlining the

importance of collecting a high sample density across multiple vertical transects (Atherton, 2017; Barsi, 2017; Vriens et al., 2019).

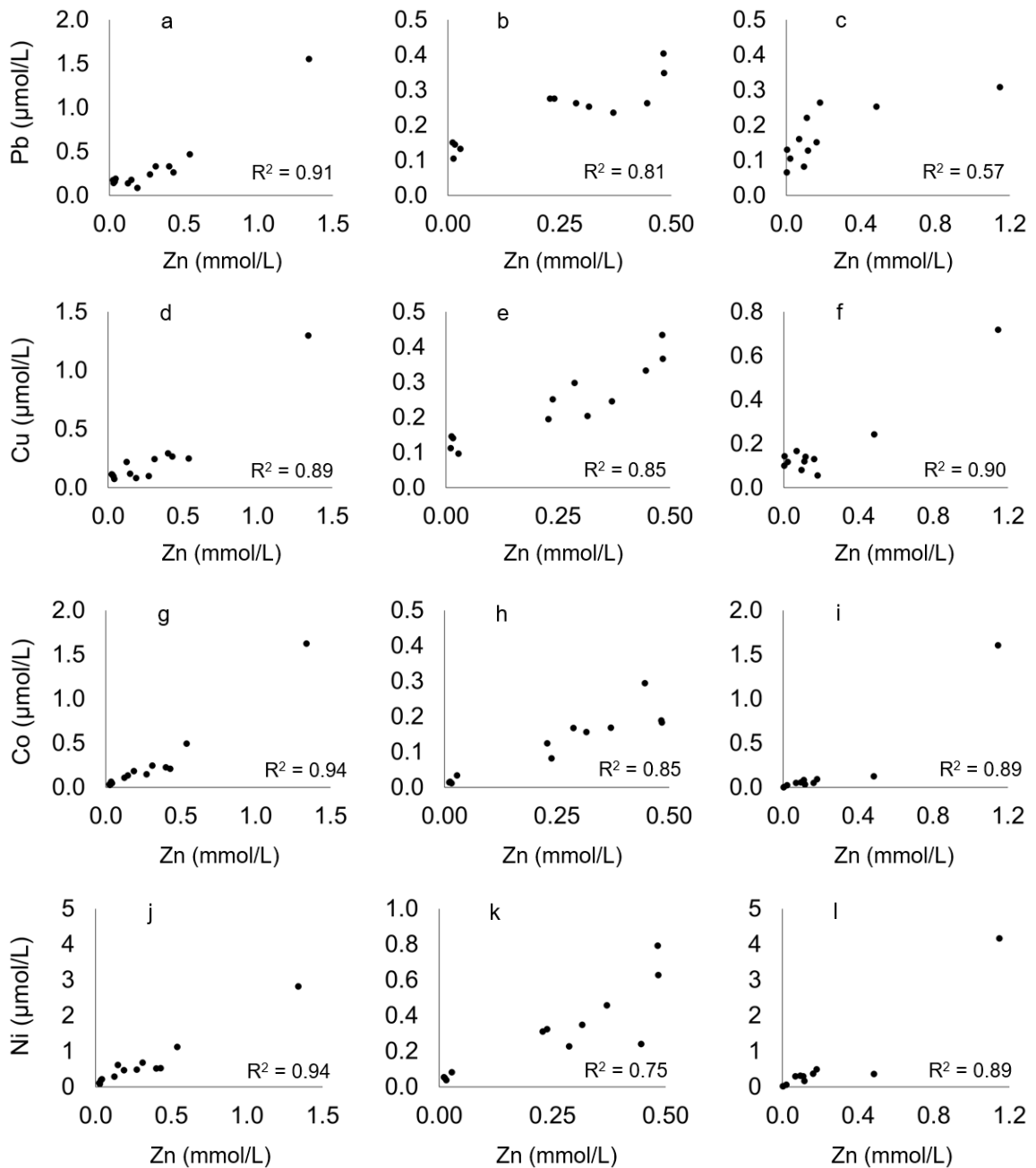


Figure 3.14: Zn (mmol/L) correlation plots with Pb, Cu, Co, and Ni (µmol/L) for trench 1 (left), trench 2 (middle), trench 3 (right).

Manganese was the only other metal that measured anomalously high concentrations at 0.5 m in trench 1 and 2.5 m depth in trench 3, which also did not correspond with solid-phase chemical data. Manganese was not detected as a trace component of any sulfide mineral, so it was less likely that Mn was being released from oxidizing sulfides. Alternatively, under range (≤ 1 wt.%) Mn was detected in calcite and dolomite grains (Ch. 2) and the anomalously high concentrations of Mn in these localities may be a function of continual carbonate buffering from accelerated long-term sulfide oxidation in finer-grained fractions of waste-rock material (McCreadie et al., 2000). In most cases, concentrations of Mn in the porewaters were three orders of magnitude lower than dissolved Ca and did not show a positive correlation beyond Ca concentrations of approximately 9 mmol/L indicating that Ca porewater concentrations are being controlled by secondary minerals, likely gypsum and calcite (Fig. 3.15a - c), whereas rhodochrosite was too undersaturated for the removal of Mn^{2+} (Langmuir, 1997; Blowes et al., 2013).

Jeong and Lee (2003) measured seepage water Mn, Ca, and Zn concentrations of 9.10 $\mu\text{mol/L}$, 3.27 mmol/L, and 0.16 mmol/L, respectively, from a waste-rock pile at the Dadeok mine subjected to 50 years of sphalerite ($\text{Zn}_{0.84}\text{Fe}_{0.15}\text{Mn}_{0.01}\text{S}$) weathering and subsequent circumneutral pH buffering primarily by manganoan calcite ($\text{Ca}_{0.84}\text{Mn}_{0.16}\text{CO}_3$). Manganese was not contained in sphalerite at Ore Chimney and under range Mn signals from SEM-EDX analysis of calcite in the Ore Chimney waste rock revealed a conservative mineral formula with a Mn content no greater than $\sim\text{Ca}_{0.98}\text{Mn}_{0.02}\text{CO}_3$, which has an eightfold lower Mn content than observations by Jeong and Lee (2003). Therefore, despite Mn being significantly less concentrated in Ore Chimney carbonates in contrast to Dadeok, the similar concentrations of dissolved Mn (12.36 $\mu\text{mol/L}$ at 5.0 m in trench 1) and comparable Ca/Mn ratios (Ca:Mn = ~ 360 at Dadeok; Ca:Mn = ~ 740 at 5.0 m depth in trench 1 at Ore Chimney) coupled with higher porewater Zn (0.54 mmol/L) at Ore Chimney may have resulted from the nearly doubled exposure time and additional 50 years of weathering.

SEM-EDX observations indicate apatite (Ch. 2; Fig. 2.18a) as a potential source for PO_4^{3-} in the porewaters, which measured an average of 0.15 ($\sigma = 0.03$) ppm (PO_4^{3-}) and was very consistent with depth. It is likely that dissolved concentrations of PO_4^{3-} and Mn (as Mn^{2+}) are being constrained by the formation of $\text{Mn}^{2+}\text{HPO}_4$, which has been proposed as an important Mn control under near-neutral pH with available PO_4^{3-} , whereas rhodochrosite is favoured in more alkaline environments (Boyle and Lindsay, 1985; Eary, 1999; Enviromin, 2017). Porewater Eh and pH readings at Ore Chimney predict Mn to be metastable in the Mn^{3+} oxidation state (Pourbaix, 1974), which explains why SI simulations also predicted manganite [$\text{Mn}^{3+}\text{O}(\text{OH})$] as a potential control at 0.5 m depth in trench 1 and at the surface of trench 2, which corresponded to the highest Eh readings of +547 and +518 mV, respectively.

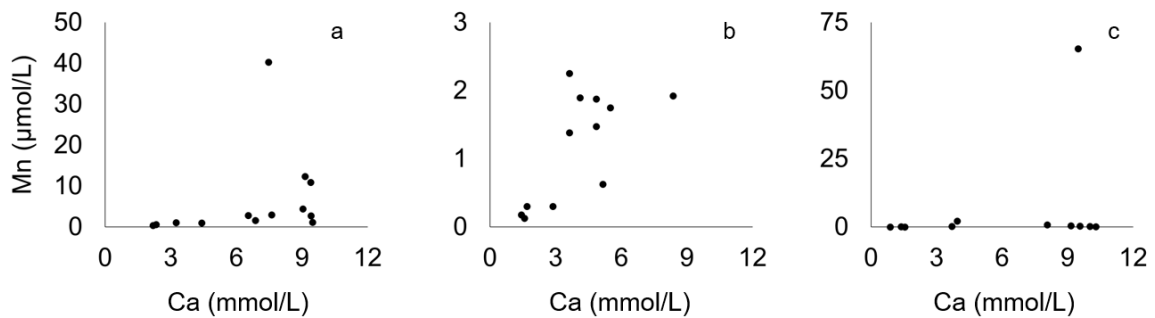


Figure 3.15: Ca (mmol/L) correlation plot with Mn ($\mu\text{mol/L}$) for trench 1 (left), trench 2 (middle), and trench 3 (right).

Eh and pH conditions throughout the waste-rock pile at Ore Chimney also predicted polyvalent Fe and Cr to be most stable in the (3+) oxidation state and subsequently controlled by the formation of amorphous $\text{Fe}(\text{OH})_{3(s)}$ and $\text{Cr}(\text{OH})_{3(s)}$ phases, which have the lowest solubilities at near-neutral pH thus maintaining considerably lower porewater concentrations compared to most other metals (Pourbaix, 1974; Langmuir, 1997). Similar to Fe and Cr, porewater Al concentrations were consistent with depth and showed minimal variation between trenches. Dissolved Al was predicted to be consistently near saturation with

boehmite and gibbsite, which also have relatively low solubilities, especially at near-neutral pH, explaining why the porewaters at Ore Chimney measured low average Al concentrations of 5.6 ($\sigma = 3.9$) ppb throughout the entire pile (Langmuir, 1997). Higher dissolved concentrations of Fe^{3+} and Al are ordinarily observed in acidic mine-waters due to the accelerated dissolution of Al/Fe-hydroxides and aluminosilicates, which have increased solubilities at lower pH (Bigam and Nordstrom, 2019; Vriens et al., 2019), whereas the dissolution of $\text{Al}(\text{OH})_3$ and $\text{Fe}(\text{OH})_3$ was not favoured at Ore Chimney due to the neutral pH levels maintained by the abundance of calcite and dolomite. Furthermore, the geochemical signatures at Ore Chimney provide empirical evidence that dissolved concentrations of in situ Fe and Al that may leach through weathered waste-rock can be regulated significantly for at least ~100 years by maintaining a sufficient Ca-carbonate neutralization capacity.

The blasting of waste rock is often facilitated by perchlorate (ClO_4^-), which can be enriched in the stockpiled material and contribute to measurable porewater Cl concentrations (Cox, 2005; Bailey et al., 2013). Chloride also acts as a conservative tracer that can be measured to help elucidate waste-rock permeability and the downward migration of water through the vadose zone (Neuner et al., 2013). However, if mining activities at Ore Chimney incorporated perchlorate as a blasting agent, the contaminated signature would have likely flushed through the pile within the first few years (Bailey et al., 2013). Porewater Cl was not observed to be controlled by secondary phases and measurements likely resembled natural signatures derived from a variety of minerals hosting Cl in trace amounts. Likewise, no controls were observed for porewater concentrations of Ti. Although concentrated in the solid phase by an average of 3600 ppm, Ti concentrations in the porewaters measured average concentrations of 0.6 ppb indicating that ilmenite and rutile have a very high resistance to weathering (Sudom and St. Arnaud, 1971) and partition into porewaters at extremely low ppb levels (Skrabal and Terry, 2002) even after ~100 years of exposure above ground surface.

SEM-EDX analysis did not detect As nor Sb as a solid-phase component for pyrite, chalcopyrite, sphalerite, or galena. Instead, As and Sb concentrations were exclusively contained by arsenopyrite (FeAsS), and a (Cu,Sb,Ag)-bearing sulfide mineral (freibergite), respectively, found only in a few sample locations (Ch. 2). Dissolved As and Sb concentrations are likely derived from the oxidative dissolution of arsenopyrite and freibergite (Koski et al., 2008) and these minerals have been previously documented to exist within the mineralized Ore Chimney Formation (Harnois and Moore, 1989). Redox and pH conditions predict Sb to be more stable in the Sb(V) oxidation state, which adsorbs strongly to goethite across a pH range from 3 to 8 (Pourbaix, 1974; Martínez-Lladó et al., 2008). No secondary controls were predicted for As nor Sb from SI simulations; however, Sb was occasionally measured up to 3 wt.% as a potential adsorption phase on Fe-oxyhydroxide alteration surfaces, which is less significant than Pb, Zn, and Cu, but may control dissolved Sb to some extent.

3.4.2 Implications

Porewater concentrations of Ca and SO_4^{2-} at Ore Chimney peaked at approximately 400 and 2,000 ppm, which were observed closer to the base of the waste-rock pile. Smith et al (2013b) measured Ca and SO_4^{2-} concentrations in drainage waters from a constructed waste-rock test pile at Diavik mine with low relative carbon (~0.02 wt.%) and sulfur (0.16 wt.%) content, which plateaued at approximately 350 and 2,000 ppm, respectively, after only four months of weathering. Gypsum saturation was interpreted to limit dissolved Ca and SO_4^{2-} at Diavik and Ore Chimney, which demonstrates that elevated sulfide and carbonate content and prolonged subaerial exposure (i.e. Ore Chimney) are not required to saturate Ca and SO_4^{2-} concentrations with respect to Gypsum. It also indicates that gypsum can serve as a major control for dissolved Ca and SO_4^{2-} concentrations over long timescales when there is ongoing sulfide oxidation and an abundance of Ca-bearing carbonate minerals in the waste rock. Elevated alkalinity measurements ($\mu = 60.2 \text{ mg/L CaCO}_3$) throughout the Ore Chimney waste-rock pile are derived from calcite and dolomite dissolution resulting in stable

near-neutral pH levels. Consistently low-ppb measurements of Fe, Al, and Cr are suggested to be controlled by the formation of secondary hydroxide phases with low relative solubilities, which signifies that the concentrations of dissolved in situ Fe, Al, and Cr are minimized over long time periods by near-neutral pH conditions maintained by an abundance of calcite and dolomite.

Atherton (2017) deconstructed a low-carbon (~0.02 wt.% C) and low-sulfur (~0.02 wt.% S) 10-metre-high waste-rock test pile at the Diavik mine that had weathered for approximately eight years and collected in situ porewater samples throughout the entire depth profile at ~3 m sampling intervals. The carbonate neutralization capacity was depleted in at least one location (~3 m depth) yielding a pH of 4 that corresponded with elevated dissolved porewater concentrations of SO_4^{2-} , Ca, Fe, Al, Ni, Co, Cu, and Zn. Likewise, Ca and SO_4^{2-} measurements of ~400 and ~2,500 ppm, respectively, were likely being controlled by the formation of gypsum, which was observed to be nearest saturation at that locality. The geochemical signatures in the waste-rock test pile at Diavik investigated by Atherton (2017) were observed to be heavily dependent on pH, which depended on the carbonate content, or lack thereof. Atherton (2017) also observed elevated SO_4^{2-} , Ca, and Mg at ~6 m depth, which did not correspond to low pH nor other abovementioned metals suggesting the accumulation of SO_4^{2-} , Ca, and Mg to a depth range of 3 m from eight years of weathering.

Porewater concentrations of SO_4^{2-} , Ca, and Mg at Ore Chimney accumulated from 0.0 to 5.0 m depth, which is greater than the ~3 m depth range observed by Atherton (2017), possibly due to a longer weathering period, but likely not a signature unique to ~100 years. Instead, it provides an indication that weathering processes drive Ca and SO_4^{2-} to near saturation within approximately a decade if weathering is accelerated due to a limited carbonate content and can reveal SO_4^{2-} , Ca, and Mg depth profiles similar to what was observed at Ore Chimney despite the significant difference in exposure times. An abundance of carbonate minerals that maintain near-neutral pH for nearly a century (i.e. Ore Chimney) subject sulfide minerals to slower weathering rates than younger waste-rock piles

that are weathering faster under acidic conditions and can create difficulties in making comparisons based on differences in age. Therefore, the mineralogy and mineral abundance plays a significant role in characterizing waste-rock weathering, and it is imperative to have a comprehensive understanding on the physical properties of mine-waste material and in situ solid-phase and aqueous-phase geochemical signatures to isolate and properly address the influence of time.

Jeong and Lee (2003) investigated the weathering of waste rock derived from quartz veins bearing galena, sphalerite and manganoan carbonates that weathered at the Dadeok mine for at least 50 years. Drainage waters underneath the Dadeok waste-rock pile measured Zn concentrations as high as 10.2 ppm derived from sphalerite weathering under near-neutral pH with a similar Fe content as Ore Chimney sphalerite (Ch.2). Porewater Zn concentrations at the base of trenches 1 and 2 at Ore Chimney measured 35.2 and 31.6 ppm, which are threefold higher than measurements by Jeong and Lee (2003). While the higher Zn concentrations at Ore Chimney may be a function of an additional 50 years of weathering, seepage waters may represent more dilute concentrations than in situ centrifuged porewaters. Moreover, Jeong and Lee (2003) did not quantify solid-phase Zn concentrations so the elevated Zn (and Cd) at Ore Chimney may also be from a higher proportion of sphalerite.

Jeong and Lee (2003) and Ore Chimney measured significantly higher dissolved Zn concentrations than Pb. The Zn:Pb ratio measured at Dadeok was approximately 50 whereas Zn:Pb ratios at the base of trenches 1 and 2 at Ore Chimney were 360 and 440, respectively. Jeong and Lee (2003) observed alteration rims of Galena to be replaced by anglesite whereas Pb concentrations at Ore Chimney were undersaturated with respect to anglesite and alteration rims were determined to be replaced by cerussite, which may be due to a higher carbonate content in the waste rock. The solubility product (i.e. K_{sp}) of cerussite (1.6×10^{-13}) is five orders of magnitude lower than anglesite (1.6×10^{-8}), which may help explain why the Zn:Pb ratios are significantly higher at Ore Chimney than

Dadeok mine (Marani et al., 1995). Therefore, carbonate-rich waste rock may exert a stronger control on Pb through the formation of cerussite even after ~100 years of weathering, as observed at Ore Chimney.

Waste-rock piles are inherently complex, and the geochemical signatures are evidently a function of variable weathering characteristics such as mineralogy, grain size, hydrologic flow regimes, and time (Blowes et al., 2013). Despite these inherent differences among various waste-rock studies, including Ore Chimney and others in the literature, the fundamental processes for sulfide weathering, pH buffering, and secondary chemical controls that are described for young waste rock, are also observed for much older systems (i.e. Ore Chimney). After ~100 years, the liberation of metals from sulfide oxidation and carbonate mineral dissolution remains an ongoing process. Likewise, dissolved metal concentrations as a function of long-term weathering are similarly controlled by secondary attenuation processes such as mineral precipitation and adsorption onto the surfaces of secondary mineral phases. The differences in geochemical signatures between waste rock exposed for a year compared to ~100 years has a greater dependency on internal factors such as alkalinity, mineralogy, and grain size than external factors such as exposure time. For Ore Chimney, the remaining presence of sphalerite in addition to galena, pyrite, and chalcopyrite strongly suggests that weathering processes will continue to occur. Likewise, the in situ signatures will continue to be regulated by secondary controls, and abundant alkalinity and carbonate minerals suggest that drainage pH will remain neutral as the waste-rock pile continues to age.

Chapter 4: Conclusions

4.1 General Summary of Implications

The Ore Chimney waste-rock pile revealed total S (2.02 wt.%) and C (1.38 wt.%) concentrations that are significantly higher than what is commonly reported in the literature for waste-rock piles at other mines (Smith et al., 2013a; Fan et al., 2014; Essilfie-Dughan et al., 2017). The sulfide mineral assemblage at Ore Chimney was mainly derived from calcite- and dolomite-bearing quartz veins and primarily composed of sphalerite and galena with a lower occurrence of pyrite and chalcopryrite. High concentrations of in situ porewater alkalinity ($\mu = 60.2$ mg/L CaCO_3) and consistent near-neutral pH (6.4 - 8.3) at Ore Chimney are a function of high concentrations of calcite and dolomite, but also due to a reduced tendency for sphalerite and galena to generate acidity from weathering processes under the availability of oxygen (Equation 1) (Plumlee, 1999). High Eh readings coupled with observations of sulfide alteration were consistent across depth and location indicating a fully aerobic system, which may be attributed to the accumulation of coarse material towards the base of the waste-rock pile from edge dumping and prolonged weathering (Lahmira et al., 2016).

Total S and C content of the waste rock were observed to be independent of grain size between ranges of < 0.5 mm and 0.5 to 2.0 mm. It is therefore suggested that sulfide and carbonate grains encapsulated by quartz have a decreased propensity for partitioning into finer grain sizes from blasting and long-term subaerial exposure and the source of sulfide minerals may play an important role in weathering. Studies of younger mine-waste systems [i.e. Gunsinger et al., 2006a (28 years), Jeong and Lee, 2003 (50 years), and Moncur et al., 2009 (70 years)] described a relative sulfide mineral resistance to alteration in the order chalcopryrite > pyrite > galena > sphalerite, which was consistently observed after ~100 years at Ore Chimney. Sphalerite showed the highest susceptibility to weathering but was still abundant throughout the entire waste-rock pile suggesting that sulfide weathering will actively continue. Observations of secondary Fe-oxyhydroxide phases on the

alteration rims of pyrite and chalcopyrite suggest higher adsorption affinities of Cu, Pb, and Zn, and slower weathering rates; however, it is likely that they will continue to serve as the primary acid-generating sources in the waste-rock pile. Nonetheless, the uncertain acid-generating capacity at Ore Chimney governed by inherent physical and chemical heterogeneities and the presence of pyrite and chalcopyrite is not expected to generate AMD in the near future due to the abundance of Ca-carbonates.

The high alkalinity in the waste-rock porewaters derived from the abundance of Ca-carbonates controlled dissolved Zn, Cd, Pb, and Cu by the formation of secondary metal-carbonates. The magnitude of concentration of dissolved Zn, Cd, Pb, and Cu is likely due to differences in solubility products of the respective secondary carbonate mineral controls, and insufficient alkalinity (i.e. 0.5 m in trench 1 and 2.5 m depth in trench 3) corresponded with elevated metals in the porewater. Results from this study indicate that principal waste-rock weathering mechanisms, such as the accumulation of heavy metals and sulfate from sulfide oxidation, pH buffering from Ca-carbonates, and secondary controls on porewater chemistry can appropriately describe mine-waste systems that have weathered across a wide range of timescales. As such, the differences in drainage chemistry and in situ geochemical signatures between mine-waste studies of different exposure times tends to be a result of lithological and mineralogical variations as opposed to prolonged weathering.

4.2 Recommendations for Areas of Future Research

It can be assumed that gypsum has been near saturation in the waste-rock porewaters at Ore Chimney for an extended period. As such, a more detailed investigation looking at gangue minerals under transmitted light and SEM-EDX may have led to direct observations of gypsum, which would corroborate interpretations of its presence and help understand the effect that the abundance of gypsum may have on AP and subsequent NPR calculations. Solid-phase sulfide and sulfate content can be distinguished by employing certain laboratory analytical methods described by Pillai et al, (2007) and Mussa et al, (2009) that may have

greater utility in the case for Ore Chimney. Likewise, samples of waste-rock material can be sieved to an even finer grain size fraction and analyzed by PXRD to potentially resolve and quantify the presence of gypsum among other secondary mineral phases (Piantone et al., 2004). Estimations of NPR values at Ore Chimney may also be adjusted to account for differences in chemical weathering between acid-generating and non-acid generating sulfide minerals.

The oxidation ranking scheme and subsequent SAI developed herein was performed only on the coarse-grained fraction of waste-rock material (0.5 to 2.0 mm) since SEM-EDX analysis on polished grain mounts representing the fine-grained fraction (< 0.5 mm) required a carbon coating, which rendered them ineffective for further investigation with optical microscopy. SAI assessments could have been conducted on the entire suite of both grain fractions prior to SEM-EDX analysis and weathering extents could have been compared in greater detail to gain a better understanding on long-term weathering with grain size. However, mineral obscurities from high degrees of weathering and difficulties with preparing the < 0.5 mm polished grain mounts necessitated the use of SEM-EDX to ensure that ore minerals were properly identified. In addition, electron microprobe analysis (EMPA) can be employed to perform higher chemical and spatial resolution analyses of alteration phases.

The high-resolution sampling technique facilitated by carefully deconstructing the waste-rock pile resulted in field work that could only be attempted once. Likewise, additional 5 to 6 kg samples of waste-rock material were collected in tandem with samples collected for solid-phase and aqueous-phase investigations in consideration for particle size distributions throughout the waste-rock pile and their effect on geochemical signatures in the waste rock. Samples under a wider range of grain sizes can be analyzed for total C/S to help investigate how sulfur derived from quartz veins partitions into different grain sizes and how this compares with sulfur derived from other lithologies, such as biotite schist at Diavik (Smith et al., 2013a).

5.0 References

- Abdus-Salam, N., & Adekola, F. A. (2005). The Influence of pH and Adsorbent Concentration on Adsorption of Lead and Zinc on a Natural Goethite. *African Journal of Science and Technology*, 6, 55-66.
- Aguilar, V., Ruvalcalba-Sil, J. L., Brucio, L., & Rivera-Muñoz, E. M. (2019). Characterization and setting protocol for a simultaneous X-ray Diffraction - X-ray Fluorescence system (XRD/XRF) for in situ analysis. *The European Physical Journal Plus*, 134: 286
- Aiken, G. R., Hsu-Kim, H., & Ryan, J. N. (2011). Influence of dissolved organic matter on the environmental fate of metals, nanoparticles, and colloids. *Environmental science and technology*, 45:3196-3201.
- Akcil, A., & Koldas, S. (2006). Acid Mine Drainage (AMD): causes, treatment and case studies. *Journal of Cleaner Production*, 14, 1139-1145.
<https://doi.org/10.1016/j.jclepro.2004.09.006>
- Amos, R. T., Blowes, D. W., Bailey, B. L., Sego, D. C., Smith, L., Ian, A., & Ritchie, M. (2015). Waste-rock hydrogeology and geochemistry. *Applied Geochemistry*, 57, 140-156.
<https://doi.org/10.1016/j.apgeochem.2014.06.020>
- Amrani, M., Taha, Y., Elghali, A., Benzaazoua, M., Kchikach, A., & Hakkou, R. (2021). An experimental investigation on collapsible behavior of dry compacted phosphate mine waste rock in road embankment. *Transportation Geotechnics*, 26, 100439. <https://doi.org/10.1016/j.trgeo.2020.100439>
- Archibald, J. C. (2012). Technical Report on the Diamond Drilling Program 2011-2012 Ore Chimney Mine Property NTS 31C/43 SW UTM Zone 18 329700E - 4960300 N Barrie Township, S.W. Ontario.
- ASTM C702/C702M-11 Standard Practice, (2011). Standard Practice for Reducing Samples of Aggregate to Testing Size. In: *Anonymous Annual Book of ASTM Standards, American Society for Testing and Materials*.
- Atherton, C. (2017). An Investigation of Heterogeneity and the Impact of Acidic Regions on Bulk Effluent from a Deconstructed Low Sulfide Waste-Rock Pile. *Masters Thesis, University of Waterloo*.
- Azam, S., Wilson, G. W., Herasymuik, G., Nichol, C., & Barbour, L. S. (2007). Hydrogeological behaviour of an unsaturated waste rock pile: a case study at the Golden Sunlight Mine, Montana, USA. *Bulletin of Engineering Geology and the Environment*, 66, 259-268.

- Azam, S., Wilson, G. W., Fredlund, D. G., & Van Zyl, D. (2011). Geotechnical characterization of mine waste rock. In *Proceedings of the 17th International Conference on Soil Mechanics and Geotechnical Engineering: 5-9 October 2009, Alexandria, Egypt*, 5, 3421-3425.
- Bailey, B. L., Smith, L. J. D., Blowes, D. W., Ptacek, C. J., Smith, L., & Segó, D. C. (2013). The Diavik Waste Rock Project: Persistence of contaminants from blasting agents in waste rock effluent. *Applied Geochemistry*, 36, 256-270. <https://doi.org/10.1016/j.apgeochem.2012.04.008>
- Bain, J. G., Mayer, K. U., Blowes, D. W., Frind, E. O., Molson, J. W. H., Kahnt, R., & Jenk, U. (2001). Modelling the closure-related geochemical evolution of groundwater at a former uranium mine. *Journal of Contaminant Hydrology*, 52, 109-135. [https://doi.org/10.1016/S0169-7722\(01\)00155-3](https://doi.org/10.1016/S0169-7722(01)00155-3)
- Balistrieri, L. S., Borrok, D. M., Wanty, R. B., & Ridley, W. I. (2008). Fractionation of Cu and Zn isotopes during adsorption onto amorphous Fe(III) oxyhydroxide: Experimental mixing of acid rock drainage and ambient river water. *Geochimica et Cosmochimica Acta*, 72, 311-328. <https://doi.org/10.1016/j.gca.2007.11.013>
- Bao, Z., Bain, J., Holland, S. P., Wilson, D., MacKenzie, P., Ptacek, C. J., & Blowes, D. W. (2020). Faro Waste Rock Project: Characterizing geochemical heterogeneity in sulfide- and carbonate-rich waste rock. *Applied Geochemistry*, 121, 104691. <https://doi.org/10.1016/j.apgeochem.2020.104691>
- Bao, Z., Al, T., Couillard, M., Poirier, G., Bain, J., Shrimpton, H. K., Finrock, Y. Z., Lanzirotti, A., Paktunc, D., Saurette, E., Hu, Y., Ptacek, C. J., & Blowes, D. W. (2021). A cross scale investigation of galena oxidation and controls on mobilization of lead in mine waste rock. *Journal of Hazardous Materials*, 412, 125130. <https://doi.org/10.1016/j.jhazmat.2021.125130>
- Barsi, D. (2017). Spatial variability of particles in waste rock piles. *Masters Thesis, University of Waterloo*.
- Berghorn, G. H., & Hunzeker, G. R. (2001). Passive Treatment Alternatives for Remediating Abandoned-Mine Drainage. *Remediation*, 11, 111-127. <https://doi.org/10.1002/rem.1007>
- Bhatti, T. M., Bigham, J. M., Vuorinen, A., & Tuovinen, O. H. (2011). Weathering of biotite in *Acidithiobacillus ferrooxidans* cultures. *Geomicrobiology Journal*, 28, 130-134. <https://doi.org/10.1080/01490451003720901>

- Bigham, J. M., & Nordstrom, D. K. (2019). Iron and aluminum hydroxysulfates from acid sulfate waters. *Sulfate Minerals: Crystallography, Geochemistry, and Environmental Significance*, 40, 351-403. <https://doi.org/10.2138/rmg.2000.40.7>
- Blowes, David W., & Jambor, J. L. (1990). The pore-water geochemistry and the mineralogy of the vadose zone of sulfide tailings, Waite Amulet, Quebec, Canada. *Applied Geochemistry*, 5, 327-346. [https://doi.org/10.1016/0883-2927\(90\)90008-S](https://doi.org/10.1016/0883-2927(90)90008-S)
- Blowes, D. W., Ptacek, C. J., Jambor, J. L., Weisener, C. G., Paktunc, D., Gould, W. D., & Johnson, D. B. (2013). The Geochemistry of Acid Mine Drainage. In *Treatise on Geochemistry: Second Edition (11th ed., Vol. 11)*. Elsevier Ltd. <https://doi.org/10.1016/B978-0-08-095975-7.00905-0>
- Borgne, V. Le, Cosentino, A., Brehe, J-M., & Thivierge, S-E. (2018). Deployment Of Large-area Radio-enabled Monitoring Systems In Northern Mines. In *International Symposium on Field Measurements in Geomechanics: 16-20 July 2018, Rio De Janeiro, Brazil*.
- Boulanger-Martel, V., Bussière, B., & Côté, J. (2021). Resistance of a soapstone waste rock to freeze-thaw and wet-dry cycles: implications for use in a reclamation cover in the Canadian Arctic. *Bulletin of Engineering Geology and the Environment*, 80, 41-54. <https://doi.org/10.1007/s10064-020-01930-8>
- Boulet, M. P., & Larocque, A. C. L. (1998). A comparative mineralogical and geochemical study of sulfide mine tailings at two sites in New Mexico, USA. *Environmental Geology*, 33, 130-142. <https://doi.org/10.1007/s002540050233>
- Boyle, F. W., & Lindsay, W. L. (1985). Diffraction Patterns and Solubility Products of Several Divalent Manganese Phosphate Compounds. *Soil Science Society of America Journal*, 49, 761-766. <https://doi.org/10.2136/sssaj1985.03615995004900030046x>
- Carranza, E. J. M., & Sadeghi, M. (2012). Primary geochemical characteristics of mineral deposits - Implications for exploration. *Ore Geology Reviews*, 45, 1-4. <https://doi.org/10.1016/j.oregeorev.2012.02.002>
- Carter, T., R. (1984). Metallogeny of the Grenville Province, Southeastern Ontario. Ontario Geological Survey. Available at: <http://www.geologyontario.mndmf.gov.on.ca/mndmfiles/pub/data/imaging/OFR5515//OFR5515.pDf>
- Cash, A. (2014). Structural and Hydrologic Characterization of Two Historical Waste Rock Piles. *Masters Thesis, University of Alberta*.

- Chidambaram, S., Anandhan, P., Prasanna, M. V., Ramanathan, A. L., Srinivasamoorthy, K., & Kumar, G. S. (2012). Hydrogeochemical Modelling for Groundwater in Neyveli Aquifer, Tamil Nadu, India, Using PHREEQC: A Case Study. *Natural Resources Research*, 21, 311-324. <https://doi.org/10.1007/s11053-012-9180-6>
- Combes, J. M., Manceau, A., Calas, G., & Bottero, J. Y. (1989). Formation of ferric oxides from aqueous solutions: A polyhedral approach by X-ray absorption spectroscopy: I. Hydrolysis and formation of ferric gels. *Geochimica et Cosmochimica Acta*, 53, 583-594. [https://doi.org/10.1016/0016-7037\(89\)90001-X](https://doi.org/10.1016/0016-7037(89)90001-X)
- Cook, N. J., Ciobanu, C. L., Pring, A., Skinner, W., Shimizu, M., Danyushevsky, L., Saini-Eidukat, B., & Melcher, F. (2009). Trace and minor elements in sphalerite: A LA-ICPMS study. *Geochimica et Cosmochimica Acta*, 73, 4761-4791. <https://doi.org/10.1016/j.gca.2009.05.045>
- Cox, E. (2005). Alternative Causes of Wide-Spread, Low Concentration Perchlorate Impacts to Groundwater. *Strategic Environmental Research and Development Program (SERDP) Arlington, Virginia; Geosyntec Consultants Guelph (Ontario)*. pp. 1-45.
- Cranstone, D. (2002). A history of mining and mineral exploration in Canada and outlook for the future. *Natural Resources Canada*. pp. 1-47.
- Dawson, J. B., & Smith, J. V. (1977). The MARID (mica-amphibole-rutile-ilmenite-diopside) suite of xenoliths in kimberlite. *Geochimica et Cosmochimica Acta*, 41, 309-323. [https://doi.org/10.1016/0016-7037\(77\)90239-3](https://doi.org/10.1016/0016-7037(77)90239-3)
- Demers, I., Molson, J., Bussière, B., & Laflamme, D. (2013). Numerical modeling of contaminated neutral drainage from a waste-rock field test cell. *Applied Geochemistry*, 33, 346-356. <https://doi.org/10.1016/j.apgeochem.2013.02.025>
- Dillon, E. P. (1985). Gold-quartz-arsenopyrite vein deposits localized near the base of the Finton Group, Kaladar and Barrie Townships, Southeastern Ontario. *Ontario Geological Survey, Open-file*, pp. 1-53.
- Eary, L. E. (1999). Geochemical and equilibrium trends in mine pit lakes. *Applied Geochemistry*, 14, 963-987. [https://doi.org/10.1016/S0883-2927\(99\)00049-9](https://doi.org/10.1016/S0883-2927(99)00049-9)
- Easton, R., M. (2006). Precambrian Geology of the Cloyne-Plevna-Ompah Area, Northern Mazinaw Domain, Grenville Province. *Ontario Geological Survey*. Available at: <http://www.geologyontario.mndmf.gov.on.ca/mndmfiles/pub/data/imaging/OF R5454/OF R5454.pdf>.

- Elghali, A., Benzaazoua, M., Bouzahzah, H., Bussière, B., & Villarraga-Gómez, H. (2018). Determination of the available acid-generating potential of waste rock, part I: Mineralogical approach. *Applied Geochemistry*, 99, 31-41. <https://doi.org/10.1016/j.apgeochem.2018.10.021>
- Elghali, A., Benzaazoua, M., Bouzahzah, H., Abdelmoula, M., Dynes, J. J., & Jamieson, H. E. (2021). Role of secondary minerals in the acid generating potential of weathered mine tailings: Crystal-chemistry characterization and closed mine site management involvement. *Science of the Total Environment*, 784, 147105. <https://doi.org/10.1016/j.scitotenv.2021.147105>
- Elwood Madden, M. E., Madden, A. S., Rimstidt, J. D., Zahrai, S., Kendall, M. R., & Miller, M. A. (2012). Jarosite dissolution rates and nanoscale mineralogy. *Geochimica et Cosmochimica Acta*, 91, 306-321. <https://doi.org/10.1016/j.gca.2012.05.001>
- Enviromin. (2017). Black Butte Copper Project Water Quality Monitoring Report. *Tintina Montana Inc. pp 1-55.*
- Environment Canada. (2010). Canadian Climate Normals 1981-2010 Station Data. Arnprior Grandon, Ontario. Available at: https://climate.weather.gc.ca/climate_normals/results_1981_2010_e.html?searchType=stnProvandlstProvince=ONandtxtCentralLatMin=0andtxtCentralLatSec=0andtxtCentralLongMin=0andtxtCentralLongSec=0andstnID=4225anddispBack=0.
- Essilfie-Dughan, J., Hendry, M. J., Dynes, J. J., Hu, Y., Biswas, A., Lee Barbour, S., & Day, S. (2017). Geochemical and mineralogical characterization of sulfur and iron in coal waste rock, Elk Valley, British Columbia, Canada. *Science of the Total Environment*, 586, 753-769. <https://doi.org/10.1016/j.scitotenv.2017.02.053>
- Ettler, V., Vrtišková, R., Mihaljevič, M., Šebek, O., Grygar, T., & Drahot, P. (2009). Cadmium, lead and zinc leaching from smelter fly ash in simple organic acids-Simulators of rhizospheric soil solutions. *Journal of Hazardous Materials*, 170, 1264-1268. <https://doi.org/10.1016/j.jhazmat.2009.05.068>
- Fan, G., Zhang, D., & Wang, X. (2014). Reduction and utilization of coal mine waste rock in China: A case study in Tiefsa coalfield. *Resources, Conservation and Recycling*, 83, 24-33. <https://doi.org/10.1016/j.resconrec.2013.12.001>
- Fanfani, L., Zuddas, P., & Chessa, A. (1996). Heavy metals speciation analysis as a tool for studying mine tailings weathering. *Journal of Geochemical Explorations*, 58, 241-248.

- Ford, K. L. (2003). Passive treatment systems for acid mine drainage. *U.S. Bureau of Land Management Papers*. pp. 1-13.
- Fordham, A. W. (1990). Weathering of biotite into dioctahedral clay minerals. *Clay Minerals*, 25, 51-63. <https://doi.org/10.1180/claymin.1990.025.1.06>
- Frogner, P., & Schweda, P. (1998). Hornblende dissolution kinetics at 25°C. *Chemical Geology*, 151, 169-179. [https://doi.org/10.1016/S0009-2541\(98\)00078-3](https://doi.org/10.1016/S0009-2541(98)00078-3)
- Fu, X., Wang, Y., & Wei, F. (2010). Phase transitions and reaction mechanism of ilmenite oxidation. *Metallurgical and Materials Transactions A: Physical Metallurgy and Materials Science*, 41, 1338-1348. <https://doi.org/10.1007/s11661-010-0173-y>
- Gawdzik, A., Garbat, K., Gawdzik, A., & Gawdzik, J. (2015). Chemical Composition of The Commerce Mineral Waters Versus Tap Water In The City Of Kielce. *Proceedings of ECOpole*, 9, 15-17. [https://doi.org/10.2429/proc.2015.9\(1\)005](https://doi.org/10.2429/proc.2015.9(1)005)
- George, L., Cook, N. J., Cristiana, C., & Wade, B. P. (2015). Trace and minor elements in galena: A reconnaissance LA-ICP-MS study. *American Mineralogist*, 100, 548-569. <https://doi.org/10.2138/am-2015-4862>
- Gleisner, M. (2005). Quantification of mineral weathering rates in sulfidic mine tailings under water-saturated conditions. *PhD Thesis, Stockholm University*.
- Gorakhki, M. H., & Bareither, C. A. (2017). Sustainable reuse of mine tailings and waste rock as water-balance covers. *Minerals*, 7, 128. <https://doi.org/10.3390/min7070128>
- Goumih, A., El Adnani, M., Hakkou, R., & Benzaazoua, M. (2013). Geochemical Behavior of Mine Tailings and Waste Rock at the Abandoned Cu–Mo–W Azegour Mine (Occidental High Atlas, Morocco). *Mine Water and the Environment*, 32, 121-132. <https://doi.org/10.1007/s10230-013-0221-0>
- Grey, I. E., & Reid, A. F. (1975). The Structure of Pseudorutile and Its Role in The Natural Alteration of Ilmenite. *The American Mineralogist*, 60, 898-906.
- Gunsinger, M. R., Ptacek, C. J., Blowes, D. W., & Jambor, J. L. (2006a). Evaluation of long-term sulfide oxidation processes within pyrrhotite-rich tailings, Lynn Lake, Manitoba. *Journal of Contaminant Hydrology*, 83, 149-170. <https://doi.org/10.1016/j.jconhyd.2005.10.013>
- Gunsinger, M. R., Ptacek, C. J., Blowes, D. W., Jambor, J. L., & Moncur, M. C. (2006b). Mechanisms controlling acid neutralization and metal mobility within a Ni-rich tailings impoundment. *Applied Geochemistry*, 21, 1301-1321. <https://doi.org/10.1016/j.apgeochem.2006.06.006>

- Hach. (2013). Sulfate, SulfaVer 4 Method 10248. *Hach Company Headquarters. Document no. 316.53.01316.*
- Hach. (2014a). Sulfide, Methylene Blue Method 10254. *Hach Company Headquarters. Document no. 316.53.01319.*
- Hach. (2014b). Alkalinity, Colorimetric Method 10239. *Hach Company Headquarters. Document no. 316.54.01257.*
- Hach. (2014c). Ferrous Iron, 1,10-Phenanthroline Method 8146. *Hach Company Headquarter. Document no. 316.53.01049.*
- Hamzeh, M., Bafti, S. B., & Omrani, H. (2020). Trace element geochemistry of galena in fluorite deposits from central Alborz, Mazandaran Province. *Journal of Economic Geology, 12, 227-247.*
- Harnois, L., & Moore, J. M. (1988). Geochemistry and origin of the Ore Chimney Formation, a transported paleoregolith in the Grenville Province of southeastern Ontario, Canada. *Chemical Geology, 69, 267-289.*
[https://doi.org/10.1016/0009-2541\(88\)90039-3](https://doi.org/10.1016/0009-2541(88)90039-3)
- Harnois, L., & Moore, J. M. (1989). Geochemistry and genesis of two unconformity-associated gold deposits at the base of the Flinton Group, Grenville Province, southeastern Ontario, Canada. *Economic Geology, 84, 676-693.* <https://doi.org/10.2113/gsecongeo.84.3.676>
- Harper, C., Walsh, C., Fong, C., & Amos, R. T. (2021). Long Term Zinc Contamination and Transport at the Abandoned Ore Chimney Gold Mine. (*In press; Canadian Geotechnical Journal*).
- Hayes, S. M., Root, R. A., Perdrial, N., Maier, R. M., & Chorover, J. (2014). Surficial weathering of iron sulfide mine tailings under semi-arid climate. *Geochimica et Cosmochimica Acta, 141, 240-257.*
<https://doi.org/10.1016/j.gca.2014.05.030>
- Hedin, R. S., Watzlaf, G. R., & Nairn, R. W. (1994). Passive treatment of acid mine drainage with limestone. *Journal of Environmental Quality, 23, 1338-1345.*
- Heidel, C., Tichomirowa, M., & Junghans, M. (2013). Oxygen and sulfur isotope investigations of the oxidation of sulfide mixtures containing pyrite, galena, and sphalerite. *Chemical Geology, 342, 29-43.*
<https://doi.org/10.1016/j.chemgeo.2013.01.016>
- Hsu, S. C., & Maynard, J. B. (1999). The use of sulfur isotopes to monitor the effectiveness of constructed wetlands in controlling acid mine drainage. *Environmental Engineering and Policy, 1, 223-233.*

- Hudson-Edwards, K. A., Jamieson, H. E., & Lottermoser, B. G. (2011). Mine Wastes: Past, Present, and Future. *Elements*, 7, 375-380. <https://doi.org/10.1016/b978-0-12-381475-3.10005-1>
- ICOLD (International Commission on Large Dams). (1996). A guide to tailings dams and impoundments. *Bulletin 106*. pp 1-239.
- INAC [Indian and Northern Affairs, Canada], 1993. Guidelines for Acid Rock Drainage Prediction in the North. Catalogue Number R71-50/1E.
- Jambor, J. L., Dutrizac, J. E., Groat, L. A., & Raudsepp, M. (2002). Static tests of neutralization potentials of silicate and aluminosilicate minerals. *Environmental Geology*, 43, 1-17. <https://doi.org/10.1007/s00254-002-0615-y>
- Jameson, E., Rowe, O. F., Hallberg, K. B., & Johnson, D. B. (2010). Sulfidogenesis and selective precipitation of metals at low pH mediated by *Acidithiobacillus* spp. and acidophilic sulfate-reducing bacteria. *Hydrometallurgy*, 104, 488-493.
- Jamieson, H. E., Shaw, S. C., & Clark, A. H. (1995). Mineralogical Factors Controlling Metal Release from Tailings at Geco, Manitouwage, Ontario. *Conference on Mining and the Environment, 1 June 1995, Sudbury, Ontario*.
- Jeong, G. Y., & Lee, B. Y. (2003). Secondary mineralogy and microtextures of weathered sulfides and manganoan carbonates in mine waste-rock dumps, with implications for heavy-metal fixation. *American Mineralogist*, 88, 1933-1942. <https://doi.org/10.2138/am-2003-11-1236>
- Johnson, R. H., Blowes, D. W., Robertson, W. D., & Jambor, J. L. (2000). The hydrogeochemistry of the Nickel Rim mine tailings impoundment, Sudbury, Ontario. *Journal of Contaminant Hydrology*, 41, 49-80. [https://doi.org/10.1016/S0169-7722\(99\)00068-6](https://doi.org/10.1016/S0169-7722(99)00068-6)
- Jurjovec, J., Ptacek, C. J., & Blowes, D. W. (2002). Acid neutralization mechanisms and metal release in mine tailings: A laboratory column experiment. *Geochimica et Cosmochimica Acta*, 66, 1511-1523. [https://doi.org/10.1016/S0016-7037\(01\)00874-2](https://doi.org/10.1016/S0016-7037(01)00874-2)
- Kammerman, L. M. (2006). History of the Ontario Mining and Lands Commissioner. Ministry of Northern Development and Mines. Available at: <https://www.ontario.ca/page/history-ontario-mining-and-lands-commissioner>
- Keim, M. F., & Markl, G. (2015). Weathering of galena: Mineralogical processes, hydrogeochemical fluid path modeling, and estimation of the growth rate of pyromorphite. *American Mineralogist*, 100, 1584-1594. <https://doi.org/10.2138/am-2015-5183>

- Kingston, P. W. (1980). Resident Geologist, Tweed, Ontario. Ministry of Northern Development and Mines. Extracted and modified from Archibald, J. C. (2012).
- Kingston, P.W., & Papertzian, V.C., (1982). Gold Development Potential in Eastern Ontario (Open File Report No. 5379), *Ontario Geological Survey*. Ministry of Natural Resources.
- Komárek, M., Antelo, J., Králová, M., Veselská, V., Číhalová, S., Chrastný, V., Ettler, V., Filip, J., Yu, Q., Fein, J. B., & Koretsky, C. M. (2018). Revisiting models of Cd, Cu, Pb and Zn adsorption onto Fe(III) oxides. *Chemical Geology*, 493, 189-198. <https://doi.org/10.1016/j.chemgeo.2018.05.036>
- Kooner, Z. S. (1993). Comparative study of adsorption behavior of copper, lead, and zinc onto goethite in aqueous systems. *Environmental Geology*, 21, 242-250. <https://doi.org/10.1007/BF00775914>
- Koski, R. A., Munk, L. A., Foster, A. L., Shanks, W. C., & Stillings, L. L. (2008). Sulfide oxidation and distribution of metals near abandoned copper mines in coastal environments, Prince William Sound, Alaska, USA. *Applied Geochemistry*, 23, 227-254. <https://doi.org/10.1016/j.apgeochem.2007.10.007>
- Kwong, Y. T. J., Roots, C. F., Roach, P., & Kettley, W. (1997). Post-mine metal transport and attenuation in the Keno Hill mining district, central Yukon, Canada. *Environmental Geology*, 30, 98-107. <https://doi.org/10.1007/s002540050137>
- La Brooy, S. R., Linge, H. G., & Walker, G. S. (1994). Review of gold extraction from ores. *Minerals Engineering*, 7, 1213-1241.
- Lahmira, B., Lefebvre, R., Aubertin, M., & Bussière, B. (2016). Effect of heterogeneity and anisotropy related to the construction method on transfer processes in waste rock piles. *Journal of Contaminant Hydrology*, 184, 35-49. <https://doi.org/10.1016/j.jconhyd.2015.12.002>
- Lane, S. J., & Dalton, J. A. (1994). Electron microprobe analysis of geological carbonates. *American Mineralogist*, 79, 745-749.
- Langman, J. B., Moore, M. L., Ptacek, C. J., Smith, L., Segó, D., & Blowes, D. W. (2014). Diavik waste rock project: Evolution of mineral weathering, element release, and acid generation and neutralization during a five-year humidity cell experiment. *Minerals*, 4, 257-278. <https://doi.org/10.3390/min4020257>

- Langman, J. B., Blowes, D. W., Veeramani, H., Wilson, D., Smith, L., Segó, D. C., & Paktunc, D. (2015). The mineral and aqueous phase evolution of sulfur and nickel with weathering of pyrrhotite in a low sulfide, granitic waste rock. *Chemical Geology*, 401, 169-179. <https://doi.org/10.1016/j.chemgeo.2015.02.024>
- Langman, J. B., & Moberly, J. G. (2018). Weathering of a mined quartz-carbonate, galena-sphalerite ore and release and transport of nanophase zinc carbonate in circumneutral drainage. *Journal of Geochemical Exploration*, 188, 185-193. <https://doi.org/10.1016/j.gexplo.2018.01.024>
- Langmuir, D. (1997). Activity Coefficients of Dissolved Species in: Aqueous Environmental Geochemistry. *Prentice-Hall, Inc.*
- Lapakko, K. (2002). Metal mine rock and waste characterization tools: An overview. *International Institute for Environment and Development*, 67, 1-30.
- Laurenzi, L., Mayer, K. U., & Beckie, R. (2015). A metal attenuation study on waste rock collected from the East Dump, Antamina Mine, Peru: A combined mineralogical and geochemical approach. *International Conference on Acid Rock Drainage, April 2015, Santiago Chile*, 1-11.
- Leahy, M. J., & Schwarz, M. P. (2009). Modelling jarosite precipitation in isothermal chalcopyrite bioleaching columns. *Hydrometallurgy*, 98, 181-191.
- Lee, G., Bigham, J. M., & Faure, G. (2002). Removal of trace metals by coprecipitation with Fe, Al and Mn from natural waters contaminated with acid mine drainage in the Ducktown Mining District, Tennessee. *Applied Geochemistry*, 17, 569-581. [https://doi.org/10.1016/S0883-2927\(01\)00125-1](https://doi.org/10.1016/S0883-2927(01)00125-1)
- Lefebvre, R., Hockley, D., Smolensky, J., & Geélinas, P. (2001). Multiphase transfer processes in waste rock piles producing acid mine drainage. 1: Conceptual model and system characterization. *Journal of Contaminant Hydrology*, 52, 137-164. [https://doi.org/10.1016/S0169-7722\(01\)00156-5](https://doi.org/10.1016/S0169-7722(01)00156-5)
- Lehner, S., Savage, K., Ciobanu, M., & Cliffel, D. E. (2007). The effect of As, Co, and Ni impurities on pyrite oxidation kinetics: An electrochemical study of synthetic pyrite. *Geochimica et Cosmochimica Acta*, 71, 2491-2509. <https://doi.org/10.1016/j.gca.2007.03.005>
- Lewkowicz, A. G., & Bonnaventure, P. P. (2011). Equivalent elevation: A new method to incorporate variable surface lapse rates into mountain permafrost modelling. *Permafrost and Periglacial Processes*, 22, 153-162. <https://doi.org/10.1002/ppp.720>

- Llera, A. R., Fuertes-Fuente, M., Cepedal, A., & Martin-Izard, A. (2019). Barren and Li–Sn–Ta mineralized pegmatites from NW Spain (Central Galicia): A comparative study of their mineralogy, geochemistry, and wallrock metasomatism. *Minerals*, 9, 739. <https://doi.org/10.3390/min9120739>
- Machemer, S. D., & Wildeman, T. R. (1992). Adsorption compared with sulfide precipitation as metal removal processes from acid mine drainage in a constructed wetland. *Journal of Contaminant Hydrology*, 9, 115-131.
- Mackasey, W. O. (2000). Abandoned Mines in Canada. *WOM Geological Associates Inc.*
- Malmstrom, M., & Banwart, S. (1997). Biotite dissolution at 25°C: The pH dependence of dissolution rate and stoichiometry. *Geochimica et Cosmochimica Acta*, 61, 2779-2799.
- Marani, D., Macchi, G., & Pagano, M. (1995). Lead precipitation in the presence of sulphate and carbonate: Testing of thermodynamic predictions. *Water Research*, 29, 1085-1092. [https://doi.org/10.1016/0043-1354\(94\)00232-V](https://doi.org/10.1016/0043-1354(94)00232-V)
- Marshall, B. (2017). Facts and Figures of the Canadian Mining Industry. The Mining Association of Canada. Ottawa, Ontario, Canada. Available at: <https://mining.ca/wp-content/uploads/2020/01/FF-English-Web-1.pdf>
- Martínez-Lladó, X., de Pablo, J., Giménez, J., Ayora, C., Martí, V., & Rovira, M. (2008). Sorption of antimony (V) onto synthetic goethite in carbonate medium. *Solvent Extraction and Ion Exchange*, 26, 289-300. <https://doi.org/10.1080/07366290802053637>
- Mayer, K. U., Frind, E. O., & Blowes, D. W. (2002). Multicomponent reactive transport modeling in variably saturated porous media using a generalized formulation for kinetically controlled reactions. *Water Resources Research*, 38, 1-21 <https://doi.org/10.1029/2001wr000862>
- Mayes, W. M., Batty, L. C., Younger, P. L., Jarvis, A. P., Kõiv, M., Vohla, C., & Mander, U. (2009). Wetland treatment at extremes of pH: a review. *Science of the Total Environment*, 407, 3944-3957.
- McCarron, T., J., A. (2013). Unravelling the P-T-t history of Grenvillian Metamorphism in the Mazinaw Domain, southeastern Ontario: Insights from phase equilibria modeling and geospeedometry. *PhD Thesis, Carleton University.*
- McCreadie, H., Blowes, D. W., Ptacek, C. J., & Jambor, J. L. (2000). Influence of reduction reactions and solid-phase composition on porewater concentrations of arsenic. *Environmental Science and Technology*, 34, 3159-3166. <https://doi.org/10.1021/es991194p>

- Mead, S. (2011). Faro Mine remediation project – an overview. In *Proceedings of the Sixth International Conference on Mine Closure, Australian Centre for Geomechanics*, pp. 433-440.
https://doi.org/10.36487/acg_rep/1152_111_mead
- MNDM. (1994). Geology of Bon Echo Provincial Park, Frontenac and Lennox and Addington Counties, Grenville Province. *Ontario Geological Survey*. Available at:
<http://www.geologyontario.mndmf.gov.on.ca/mndmfiles/pub/data/imaging/OF R5899//ofr5899.pdf>
- MNDM. (2008). Modernizing Ontario's Mining Act. *Ministry of Northern Development and Mines. Government of Ontario*.
- Mohapatra, M., Mohapatra, L., Singh, P., Anand, S., & Mishra, B. (2011). A comparative study on Pb(II), Cd(II), Cu(II), Co(II) adsorption from single and binary aqueous solutions on additive assisted nano-structured goethite. *International Journal of Engineering, Science and Technology*, 2, 89-103.
<https://doi.org/10.4314/ijest.v2i8.63784>
- Moncur, M. C., Ptacek, C. J., Blowes, D. W., & Jambor, J. L. (2005). Release, transport and attenuation of metals from an old tailings impoundment. *Applied Geochemistry*, 20, 639-659.
<https://doi.org/10.1016/j.apgeochem.2004.09.019>
- Moncur, M. C., Jambor, J. L., Ptacek, C. J., & Blowes, D. W. (2009). Mine drainage from the weathering of sulfide minerals and magnetite. *Applied Geochemistry*, 24, 2362-2373.
<https://doi.org/10.1016/j.apgeochem.2009.09.013>
- Moncur, Michael C., Ptacek, C. J., Lindsay, M. B. J., Blowes, D. W., & Jambor, J. L. (2015). Long-term mineralogical and geochemical evolution of sulfide mine tailings under a shallow water cover. *Applied Geochemistry*, 57, 178-193. <https://doi.org/10.1016/j.apgeochem.2015.01.012>
- Mondillo, N., Arfè, G., Herrington, R., Boni, M., Wilkinson, C., & Mormone, A. (2018). Germanium enrichment in supergene settings: evidence from the Cristal nonsulfide Zn prospect, Bongará district, northern Peru. *Mineralium Deposita*, 53, 155-169. <https://doi.org/10.1007/s00126-017-0781-1>
- Moore, J., M., & Morton, R., L. (1986). Geology of the Marble Lake Area. Counties of Frontenac and Lennox and Addington. *Ontario Geological Survey*. Available at:
<http://www.geologyontario.mndmf.gov.on.ca/mndmfiles/pub/data/imaging/R238//r238.pdf>

- Moore, J. M., & Thompson, P. H. (1980). The Flinton Group: a late Precambrian metasedimentary succession in the Grenville Province of eastern Ontario. *Canadian Journal of Earth Sciences*, *17*, 1685-1707.
<https://doi.org/10.1139/e80-178>
- Muhammed, M., & Zhang, Y. (1989). A hydrometallurgical process for the dephosphorization of iron ore. *Hydrometallurgy*, *21*, 277-292.
- Mussa, S. A. B., Elferjani, H. S., Haroun, F. A., & Abdelnabi, F. F. (2009). Determination of available nitrate, phosphate and sulfate in soil samples. *International Journal of PharmTech Research*, *1*: 598-604.
- Natural Resources Canada. (2016). National Air Photo Library. Accessed in 2016. Ottawa, ON.
- Natural Resources Canada. (2017). Canadian Mineral Production. Available at: <https://www.nrcan.gc.ca/maps-tools-and-publications/publications/minerals-and-mining-publications/canadian-mineral-production/17722>.
- Nesbitt, H. W., Fedo, C. M., & Young, G. M. (1997). Quartz and feldspar stability, steady and non-steady-state weathering, and petrogenesis of siliciclastic sands and muds. *Journal of Geology*, *105*, 173-191.
<https://doi.org/10.1086/515908>
- Neuner, M., Smith, L., Blowes, D. W., Segó, D. C., Smith, L. J. D., Fretz, N., & Gupton, M. (2013). The Diavik waste rock project: Water flow through mine waste rock in a permafrost terrain. *Applied Geochemistry*, *36*, 222-233.
<https://doi.org/10.1016/j.apgeochem.2012.03.011>
- Nordstrom, D. K., & Alpers, C. N. (1999). Geochemistry of Acid Mine Waters. *The Environmental Geochemistry of Mineral Deposits*, *6*, 133-160.
<https://doi.org/10.5382/rev.06.06>
- Nordstrom, D. K., Blowes, D. W., & Ptacek, C. J. (2015). Hydrogeochemistry and microbiology of mine drainage: An update. *Applied Geochemistry*, *57*, 3-16.
<https://doi.org/10.1016/j.apgeochem.2015.02.008>
- Nordstrom, D. K. (1982). Aqueous pyrite oxidation and the consequent formation of secondary iron minerals. *Acid Sulfate Weathering*, *10*, 37-56.
<https://doi.org/10.2136/sssaspecpub10.c3>
- Ontario's Ministry of Northern Development, Mines, Natural Resources, and Forestry (2018). Abandoned Mines database. Retrieved from: <https://www.mndm.gov.on.ca/en/mines-and-minerals/applications/ogsearth/abandoned-mines>
- O'Reilly, K. (2012). Giant Mine, giant legacy. *Northern Public Affairs*, 50-53.

- Parbhakar-Fox, A., & Lottermoser, B. (2017). *Environmental Indicators in Metal Mining*. Springer. https://doi.org/10.1007/978-3-319-42731-7_2
- Parkhurst, D.L., & Appelo, C.A.J., (1999). User's Guide to PHREEQC (Version 2) – A Computer Program for Speciation, Batch-Reaction, One-Dimensional Transport, and Inverse Geochemical Calculations. *U.S. Geological Survey Water-Resources Investigations Report 99-4259*, pp. 1-312.
- Pearce, S., Dobchuk, B., Shurniak, R., Song, J., & Christensen, D. (2016). Linking waste rock dump construction and design with seepage geochemistry: an integrated approach using quantitative tools. In *IMWA Annual Conference: Frieberg, Germany*. pp 512-519.
- Pedretti, D., Mayer, K. U., & Beckie, R. D. (2017). Stochastic multicomponent reactive transport analysis of low quality drainage release from waste rock piles: Controls of the spatial distribution of acid generating and neutralizing minerals. *Journal of Contaminant Hydrology*, 201, 30-38. <https://doi.org/10.1016/j.jconhyd.2017.04.004>
- Petrescu, M. I. (1999). Self consistency between the Mohs hardness and the vickers microhardness for some sulphides and sulphosalts. *UPB Scientific Bulletin, Series B: Chemistry and Materials Science*, 61, 145-151.
- Pham, N. H., Segó, D. C., Arenson, L. U., Blowes, D. W., Amos, R. T., & Smith, L. (2013). The diavik waste rock project: Measurement of the thermal regime of a waste-rock test pile in a permafrost environment. *Applied Geochemistry*, 36, 234-245. <https://doi.org/10.1016/j.apgeochem.2013.05.007>
- Pham, N., Amos, R., Blowes, D., Smith, L., & Segó, D. (2015). The Diavik Waste Rock Project: Heat Transfer in a Large Scale Waste Rock Pile Constructed in a Permafrost Region. *International Conference on Acid Rock Drainage, April 2015, Santiago Chile*, 1-11.
- Piantone, P., Bodéan, F., & Chatelet-Snidaro, L. (2004). Mineralogical study of secondary mineral phases from weathered MSWI bottom ash: Implications for the modelling and trapping of heavy metals. *Applied Geochemistry*, 19, 1891-1904. <https://doi.org/10.1016/j.apgeochem.2004.05.006>
- Pillai, A., Abraham, B., & Sridharan, A. (2007). Determination of sulphate content in marine clays. *Res Appl (IJERA)*, 1: 1012-1016.
- Plumlee, G. S. (1999). The Environmental Geology of Mineral Deposits. *United States Geological Survey*. pp 71-116.
- Pourbaix, M. (1974). *Atlas of Electrochemical Equilibria in Aqueous Solutions*. Pergamon Press Ltd. <https://doi.org/10.4028/www.scientific.net/msf.251-254.143>

- Qiu, Y., & Segó, D. C. (2001). Laboratory properties of mine tailings. *Canadian Geotechnical Journal*, 38, 183-190. <https://doi.org/10.1139/cgj-38-1-183>
- Ramos, C. G., Querol, X., Dalmora, A. C., de Jesus Pires, K. C., Schneider, I. A. H., Silva, L. F. O., & Kautzmann, R. M. (2017). Evaluation of the potential of volcanic rock waste from southern Brazil as a natural soil fertilizer. *Journal of Cleaner Production*, 142, 2700-2706. <https://doi.org/10.1016/j.jclepro.2016.11.006>
- Ripley, E. M., Li, C., Moore, C. H., Elswick, E. R., Maynard, J. B., Paul, R. L., Sylvester, P., Seo, J. H., & Shimizu, N. (2011). Analytical methods for sulfur determination in glasses, rocks, minerals and fluid inclusions. *Reviews in Mineralogy and Geochemistry*, 73, 9-39.
- Rivett, M. O., Chapman, S. W., Allen-King, R. M., Feenstra, S., & Cherry, J. A. (2006). Pump-and-treat remediation of chlorinated solvent contamination at a controlled field-experiment site. *Environmental science and technology*, 40, 6770-6781.
- Rodda, D. P., Johnson, B. B., & Wells, J. D. (1993). The effect of temperature and pH on the adsorption of Copper(II), Lead(II), and Zinc(II) onto goethite. *Journal of Colloid And Interface Science*, 161, 57-62. <https://doi.org/10.1006/jcis.1993.1440>
- Rose, A. W., & Bianchi-Mosquera, G. C. (1993). Adsorption of Cu, Pb, Zn, Co, Ni, and Ag on goethite and hematite: a control on metal mobilization from red beds into stratiform copper deposits. *Economic Geology*, 88, 1226-1236. <https://doi.org/10.2113/gsecongeo.88.5.1226>
- Sangster, P. J., LeBaron, P. S., Charbonneau, S. J., Laidlaw, D. A., Wilson, A. C., Carter, T. R., & Fortner, L. (2012). Report of Activities, 2011 Resident Geologist Program. Available at: <http://www.geologyontario.mndm.gov.on.ca/mndmfiles/pub/data/imaging/OF R6277/OFR6277.pdf>
- Schroeder, P. A., Le Golvan, J. J., & Roden, M. F. (2002). Weathering of ilmenite from granite and chlorite schist in the Georgia Piedmont. *American Mineralogist*, 87, 1616-1625. <https://doi.org/10.2138/am-2002-11-1211>
- Seal, R. R., & Foley, N. K. (2002). Progress on Geoenvironmental Models for Selected Mineral Deposit Types. (Vol. 2, No. 195). *US Department of the Interior, US Geological Survey*.
- Sharp, T. G., & Buseck, P. R. (1993). The distribution of Ag and Sb in galena: inclusions versus solid solution. *American Mineralogist*, 78, 85-95.

- Sheoran, A. S., & Sheoran, V. (2006). Heavy metal removal mechanism of acid mine drainage in wetlands: a critical review. *Minerals engineering*, 19, 105-116.
- Shum, M., & Lavkulich, L. (1999). Speciation and solubility relationships of Al, Cu and Fe in solutions associated with sulfuric acid leached mine waste rock. *Environmental Geology*, 38, 59-68. <https://doi.org/10.1007/s002540050401>
- Sinclair, S., A. (2014). Influence of Freeze-Thaw Dynamics and Spatial Contributions on Geochemical Loading from a Low Sulfide Waste-Rock Pile. *Masters Thesis, University of Waterloo*.
- Skierszkan, E. K., Mayer, K. U., Weis, D., & Beckie, R. D. (2016). Molybdenum and zinc stable isotope variation in mining waste rock drainage and waste rock at the Antamina mine, Peru. *Science of the Total Environment*, 550, 103-113. <https://doi.org/10.1016/j.scitotenv.2016.01.053>
- Skousen, J. G., Sexstone, A., & Ziemkiewicz, P. F. (2000). Acid mine drainage control and treatment. *Reclamation of drastically disturbed lands*, 41, 131-168.
- Skrabal, S. A., & Terry, C. M. (2002). Distributions of dissolved titanium in porewaters of estuarine and coastal marine sediments. *Marine Chemistry*, 77, 109-122. [https://doi.org/10.1016/S0304-4203\(01\)00077-9](https://doi.org/10.1016/S0304-4203(01)00077-9)
- Smith, L. J. D., Blowes, D. W., Jambor, J. L., Smith, L., Segó, D. C., & Neuner, M. (2013a). The diavik waste rock project: Particle size distribution and sulfur characteristics of low-sulfide waste rock. *Applied Geochemistry*, 36, 200-209. <https://doi.org/10.1016/j.apgeochem.2013.05.006>
- Smith, L. J. D., Bailey, B. L., Blowes, D. W., Jambor, J. L., Smith, L., & Segó, D. C. (2013b). The Diavik waste rock project: Initial geochemical response from a low sulfide waste rock pile. *Applied Geochemistry*, 36, 210-221. <https://doi.org/10.1016/j.apgeochem.2012.06.008>
- Smith, L. J. D., Paktunc, D., & Blowes, D. W. (2021). Trace elements in sulfides and release to porewater from sulfide oxidation in a historical waste-rock pile, Ontario, Canada. *Applied Geochemistry*, 126, 104899. <https://doi.org/10.1016/j.apgeochem.2021.104899>
- Smitheringale, W. G. B. (2011). Great mining camps of Canada 5. Britannia mines, British Columbia. *Geoscience Canada*, 38, 97-134.
- Sobek, A. A., Schuller, W. A., Freeman, J. R., & Smith, R. M. (1978). Field and Laboratory Methods Applicable to Overburdens and Mine Soils (p. EPA-600/2-78-054).

- Sracek, O., Choquette, M., Gélinas, P., Lefebvre, R., & Nicholson, R. V. (2004). Geochemical characterization of acid mine drainage from a waste rock pile, Mine Doyon, Québec, Canada. *Journal of Contaminant Hydrology*, 69, 45-71. [https://doi.org/10.1016/S0169-7722\(03\)00150-5](https://doi.org/10.1016/S0169-7722(03)00150-5)
- Statistics Canada. (2012). Human Activity and the Environment. *Statistics Canada: Environment Accounts and Statistics Division*, 16, 1-46.
- Stedman, A., & Green, K. P. (2019). Fraser Institute Annual Survey of Mining Companies 2018. *Fraser Institute*.
- Stillings, L. L., Drever, J. I., Brantley, S. L., Sun, Y., & Oxburgh, R. (1996). Rates of feldspar dissolution at pH 3-7 with 0-8 mM oxalic acid. *Chemical Geology*, 132, 79-89. [https://doi.org/10.1016/s0009-2541\(96\)00043-5](https://doi.org/10.1016/s0009-2541(96)00043-5)
- Stipp, S. L. S., Hansen, M., Kristensen, R., Hochella, M. F., Bennedsen, L., Dideriksen, K., Balic-Zunic, T., Léonard, D., & Mathieu, H. J. (2002). Behaviour of Fe-oxides relevant to contaminant uptake in the environment. *Chemical Geology*, 190, 321-337. [https://doi.org/10.1016/S0009-2541\(02\)00123-7](https://doi.org/10.1016/S0009-2541(02)00123-7)
- Strömberg, B., & Banwart, S. A. (1999). Experimental study of acidity-consuming processes in mining waste rock: Some influences of mineralogy and particle size. *Applied Geochemistry*, 14, 1-16. [https://doi.org/10.1016/S0883-2927\(98\)00028-6](https://doi.org/10.1016/S0883-2927(98)00028-6)
- Sudom, M. D., & St. Arnaud, R. J. (1971). Use of Quartz, Zirconium and Titanium As Indices in Pedological Studies. *Canadian Journal of Soil Science*, 51, 385-396. <https://doi.org/10.4141/cjss71-052>
- Swedlund, P. J., Webster, J. G., & Miskelly, G. M. (2009). Goethite adsorption of Cu(II), Pb(II), Cd(II), and Zn(II) in the presence of sulfate: Properties of the ternary complex. *Geochimica et Cosmochimica Acta*, 73, 1548-1562. <https://doi.org/10.1016/j.gca.2008.12.007>
- Takahashi, T. (1960). Supergene alteration of zinc and lead deposits in limestone. *Economic Geology*, 55, 1083-1115. <https://doi.org/10.2113/qsecongeo.55.6.1083>
- Tischendorf, G., Förster, H.-J., & Gottesmann, B. (2001). Minor- and trace-element composition of trioctahedral micas: a review. *Mineralogical Magazine*, 65, 249-276. <https://doi.org/10.1180/002646101550244>
- Vriens, B., Peterson, H., Laurenzi, L., Smith, L., Aranda, C., Mayer, K. U., & Beckie, R. D. (2019). Long-term monitoring of waste-rock weathering at the Antamina mine, Peru. *Chemosphere*, 215, 858-869. <https://doi.org/10.1016/j.chemosphere.2018.10.105>

- Watzlaf, G. R., Schroeder, K. T., Kleinmann, R. L., Kairies, C. L., & Nairn, R. W. (2004). The passive treatment of coal mine drainage. *United States Department of Energy National Energy Technology Laboratory Internal Publication*, 1-72.
- Weatherington, B. L., Cunningham, C. J. L., & Pittenger, D. J. (2012). Understanding Business Research, First Edition; Appendix B: Statistical Tables. *John Wiley & Sons, Inc.*
- Wheeler, S. (2017). An assessment of sulfide mineral oxidation within a WRP from the decommissioned Ore Chimney gold mine in Northbrook, Ontario. *Undergraduate Thesis, Carleton University*.
- White, A. F., Schulz, M. S., Lowenstern, J. B., Vivit, D. V., & Bullen, T. D. (2005). The ubiquitous nature of accessory calcite in granitoid rocks: Implications for weathering, solute evolution, and petrogenesis. *Geochimica et Cosmochimica Acta*, 69, 1455-1471.
<https://doi.org/10.1016/j.gca.2004.09.012>
- Wickland, B. E., Wilson, G. W., Wijewickreme, D., & Klein, B. (2006). Design and evaluation of mixtures of mine waste rock and tailings. *Canadian Geotechnical Journal*, 43, 928-945. <https://doi.org/10.1139/T06-058>
- Wilson, M. J. (1970). A study of weathering in a soil derived from a biotite-hornblende rock: I. The Weathering of biotite. *Clay Minerals*, 8, 291-303.
- Wilson, M. J., & Farmer, V. C. (1970). A study of weathering in a soil derived from a biotite-hornblende rock: II. The Weathering of Hornblende. *Clay Minerals*, 8, 435-444.
- Winter, J. G. (1916). The prodromus of Nicolaus Steno's dissertation concerning a solid body enclosed by process of nature within a solid. *University of Michigan Humanistic Study*, 11, 229-230.
- Ye, L., Cook, N. J., Ciobanu, C. L., Yuping, L., Qian, Z., Tiegeng, L., Wei, G., Yulong, Y., & Danyushevskiy, L. (2011). Trace and minor elements in sphalerite from base metal deposits in South China: A LA-ICPMS study. *Ore Geology Reviews*, 39, 188-217.
<https://doi.org/10.1016/j.oregeorev.2011.03.001>
- Zak, J. (2013). Hydrologic Investigations of Waste Rock Test Piles in a Permafrost Environment. *Masters thesis, University of Waterloo*.
- Zaitsev, A., & Polezhaeva, L. (1994). Dolomite-calcite textures in early carbonatites of the Kovdor ore deposit, Kola peninsula, Russia: their genesis and application for calcite-dolomite geothermometry. *Contributions to Mineralogy and Petrology*, 115, 339-344.
<https://doi.org/10.1007/BF00310772>

- Zhixun, L. (1996). Leachate Chemistry and Precipitates Mineralogy of Rudolfsgruvan Mine Waste Rock Dump in Central Sweden. *Water Science and Technology*, 33, 163-171.
- Ziemkiewicz, P. F., Skousen, J. G., & Simmons, J. (2003). Long-term performance of passive acid mine drainage treatment systems. *Mine water and the Environment*, 22, 118-129.